A CENTER OF COMPETENCE IN SOLID STATE MATERIALS AND DEVICES

by

Fred A. Lindholm, Arthur J. Brodersen, Eugene R. Chenette,
Robert W. Gould, Larry L. Hench, John J. Hren, Sheng S. Li,
Jack Salz, James K. Watson

College of Engineering
University of Florida
Gainesville, Florida 32601

Scientific Report No. 2

10 October 1968

D D C
RECEIVED
NOV 2 5 1968
B

Prepared

for

**AIR FORCE CAMBRIDGE RESEARCH LABORATORIES
OFFICE OF AEROSPACE RESEARCH
UNITED STATES AIR FORCE
BEDFORD, MASSACHUSETTS 01730**

AFCRL-68-0493

A CENTER OF COMPETENCE IN SOLID STATE MATERIALS AND DEVICES

by

Fred A. Lindholm, Arthur J. Brodersen, Eugene R. Chenette,
Robert W. Gould, Larry L. Hench, John J. Hren, Sheng S. Li,
Jack Salz, James K. Watson

College of Engineering
University of Florida
Gainesville, Florida 32601

Contract No. F 19628-68-C-0058

Project No. 8687

Electrical Engineering Department

Scientific Report No. 2

10 October 1968

Contract Monitor
Richard F. Cornelissen
Solid State Sciences Laboratory

Prepared

for

**AIR FORCE CAMBRIDGE RESEARCH LABORATORIES
OFFICE OF AEROSPACE RESEARCH
UNITED STATES AIR FORCE
BEDFORD, MASSACHUSETTS 01730**

BLANK PAGE

ABSTRACT

The content of this report, for the second semi-annual period of contract support, comprises three main topics. The first treats of the relationships borne in glasses between microstructure and electrical properties. One study examines a theoretical model that relates the aperiodicity in glass lattices to electron transport. Another explores the structural mechanisms involved in the nucleation of crystal phases in glasses.

The second main topic deals with the measurement of parameters of material structure, demonstrating the measurement techniques by applying them to various materials: glass ceramics, nickel alloys, magnetic films, and degenerate semiconductors. Discussion centers on analysis by small-angle x-ray scattering, by electron microprobe, and by transmission electron microscopy. The errors inherent in the measurements and the theoretical basis for the analysis of data receive special attention.

The third main topic concerns semiconductors and semiconductor devices. One study reports, for degenerate n-type germanium and silicon, the theoretical variation of the density of quantum states as a function of impurity concentration. In another, the conventional theory of pn junctions is extended by removing the assumption of non-degeneracy. Finally, for both devices and bulk material, the sources of noise are subjected to theoretical and experimental study.

SUMMARY

The content of this report, for the second semi-annual period of contract support, comprises three main topics. The first treats of the relationships borne in glasses between microstructure and electrical properties. The second deals with the measurement of parameters of material structure, demonstrating the utility of the measurement techniques by applying them to various materials: glass ceramics, nickel alloys, magnetic films, and degenerate semiconductors. The third main topic concerns semiconductors and semiconductor devices, with emphasis on degenerate germanium and silicon and on the sources of noise in both devices and bulk material.

GLASSES: To explain electron transport phenomena in glasses containing transition metal oxides, a theoretical model is developed that takes into account the lack of periodicity of the glassy lattice and the strong electron-lattice interaction expected in the transition metal oxides. This model is termed the Nearly Crystalline Ionic Model. As a test of the adequacy of this model, comparisons are made between measured and predicted data for AC and DC conductivity. The comparison shows that two special cases of the model -- one postulating cells of small disorder surrounded by a small region of large disorder, the other postulating cells of disordered materials of a high transition-metal-oxide content surrounded by a small disordered phase of low transition-metal-oxide content -- give results in qualitative agreement with experiment. The effects of heat treatments on glass properties are attributed to either phase separation or ordering of the lattice.

A second study explores the structural mechanisms involved in the nucleation of crystal phases in a glass. It presents information concerning the rates of bulk crystallization of glasses and concerning the relationship

between the mechanisms of nucleation and growth. Binary Li_2O-SiO_2 and Na_2O-SiO_2 glasses serve as the experimental vehicles.

MEASUREMENT TECHNIQUES AND APPLICATIONS: Of the measurement techniques discussed, analysis by small-angle x-ray scattering, by electron microprobe, and by transmission electron microscopy receive the primary attention. Special consideration is given to the theoretical basis for the analysis of data and to the errors inherent in the measurements. This work -- coupled with collateral efforts concerning the measurement of electronic parameters of materials -- undergirds a major objective of our research program: the correlation of material structure and electronic properties.

During this second semi-annual period, x-ray research has centered on the determination of particle-size distribution by small-angle x-ray scattering. The theory underlying this method is first discussed. Then the method is applied to dispersion-hardened nickel alloys containing small spherical particles of thoria. The x-ray analysis yields results for the particle size distribution in good agreement with published results determined by transmission electron microscopy.

Moreover, the application of this x-ray technique to the determination of impurity clustering in degenerate semiconductors is considered, as is the structural analysis of permalloy thin films by the electron microprobe.

In transmission electron microscopy, the analysis must take account of sample thickness to avoid introducing considerable error in the evaluation of structure. When the ratio of sample thickness to particle diameter (t/b) exceeds 2, error may result. A reporting is made concerning the magnitude of this error. Partially devitrified $Li_2O-2SiO_2$ glass was examined by both transmission and reflection measurements, and the results thus yielded were compared with results of published x-ray studies. This research demonstrates

that quantitative stereological parameters can be overestimated by as much as 300% when measured in transmission if corrections for thickness effects are not made. On the other hand, the proper corrections give parameter values that differ by less than 10% from the values obtained from reflection measurements and x-ray analysis.

SEMICONDUCTORS AND SEMICONDUCTOR DEVICES: Accounts are given of two studies concerning degenerate semiconductors. The first presents, for degenerate n-type silicon and germanium, the theoretical variation of the density of quantum states as a function of impurity concentration. The second study extends the conventional theory of pn junctions by removing the assumption of non-degeneracy. In the analysis, an approximation is utilized for the Fermi-Dirac statistics and the dependence of the quantum density of states on impurity concentration is neglected. Calculations using the parameters of silicon illustrate the predicted behavior.

Research concerning noise is reported dealing with two subjects. One concerns 1/f noise present in planar bipolar transistors. The other relates to a novel theoretical formulation of recombination-generation noise in semiconductors.

TABLE OF CONTENTS

BLANK PAGE

I. Introduction

The general objective of this research program is to establish at the University of Florida a center of competence in solid-state materials and devices, with primary emphasis to be placed on materials and devices not used in the conventional silicon integrated-circuit technology.

From the efforts expended in establishing and maintaining this center of competence have evolved technical findings: technical findings concerning such materials as glass ceramics, semiconducting glasses, magnetic films, and degenerate semiconductors; concerning devices made from these materials; concerning measurement techniques; and concerning methods of fabrication. The first of the findings in these various areas appeared in Scientific Report No. 1[1]. To that report the reader is also referred for a more detailed statement of research objectives than given here and for a discussion of the means to be used in achieving these objectives.

The present report sets forth the major findings of the second semi-annual period of contract support. In the presentation to follow, Section II describes the results of research concerning glasses, Section III reports the progress relating to measurement techniques, and Section IV treats of the findings concerned with semiconductors and semiconductor devices.

REFERENCES

1. F. A. Lindholm et al, Scientific Report No. 1, Contract No. F 19628-68-C-0058, College of Engineering, University of Florida, 10 April 1968 (prepared for AFCRL, United States Air Force, Bedford, Mass.)

II.   Glasses (L. L. Hench)

This section deals first with a theoretical model relating the aperio-
dicity in glass lattices to electron transport, and, then, with a study of
the nucleation of the crystal phases of glass.

A. ELECTRON TRANSPORT PHENOMENA IN TRANSITION METAL OXIDE GLASSES (H. F.
    Schaake and L. L. Hench)

1. INTRODUCTION

The phenomenon of electronic conduction in glasses containing the
transition metal oxides has received considerable experimental attention
in recent years.[*] Although a variety of explanations have been advanced
to describe the electron transport process, essentially all the theoretical
models have been crystalline. It is the purpose of this paper to develop
a noncrystalline model which will result in a qualitative understanding of
the transport process itself, and hopefully, shed some light on the struc-
ture of the glass.

A brief review of the electron transport process in the crystalline
transition metal oxides will serve as a basis for the remainder of this
paper.[3-5] In the crystalline state, each transition metal ion is surrounded
by six oxygen ions in octahedral coordination (Figure 1). The presence of
the oxygen ions causes the d-electron energy levels of the metal ions to split.
The wave function of an electron in any one of these levels is highly localized
inside the octahedron formed by the oxygen ions. There will be a small amount
of overlap of the wave function on one metal ion with the wave function
on a neighboring metal ion, causing the formation of a very narrow
band. Depending on the particular oxide, these bands will be either

---

[*] For reviews, see Mott[1] and Mackenzie[2]
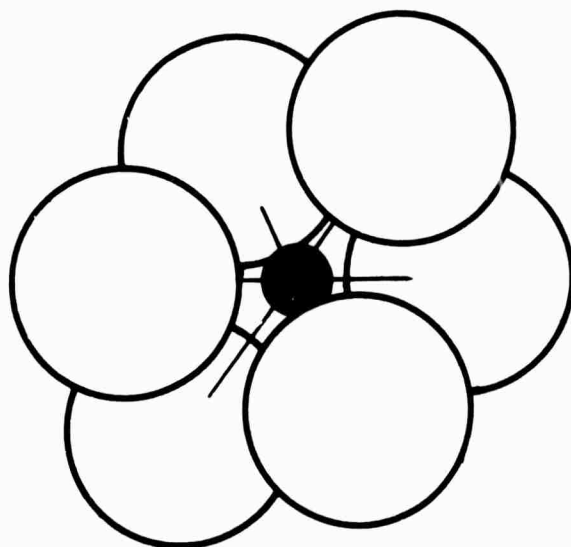
Figure 1. Transition metal oxide complex.

completely filled, partially filled, or completely empty. We shall confine our attention from hereon to the latter case. The insertion of donor states, either by the addition of impurities, or as a result of nonstoichiometry caused by the evolution of oxygen during forming, can result in the presence of electrons in the normally empty band. Consequently the oxide will be a semiconductor.

These excess electrons are usually thought of as being associated with a certain ion; the electron concentration being specified by the $Me^{(n)+}/Me^{(n+1)+}$ ratio. Although the motion of the electron through the lattice is via band diffusion, because the wave function of the electron in the lattice remains highly localized about the metal ions, the electron transport process is frequently described as a hopping of the electron from ion to ion.

The narrowness of the conduction band implies that the velocity with which the electron moves through the lattice will be extremely small. As a result of the low velocity and the highly polar nature of the lattice, the lattice will distort due to the field of the electron. The combination of lattice distortion and electron is treated theoretically as a quasi-particle known as a polaron, and behaves similarly to the "undressed" electron, but with a higher effective mass, and with a polaron bandwidth narrower than the pure electron bandwidth. Due to the strong coupling with the lattice, the polaron will be greatly affected by lattice vibrations (or phonons), and as the temperature increases, an increasing portion of the total conduction will be due to a thermally activated hopping process.

If the velocity of the electron is slow enough, and the electron-lattice coupling large enough, the lattice in the immediate

vicinity of the electron will be able to react to the field of the electron, effectively trapping it. The resultant combination of the electron and lattice distortion is known as a small polaron. At low temperatures the small polaron will move by band diffusion, although with a very high effective mass, and an extremely small polaron bandwidth (of the order of 10^{-2} to 10^{-4} that of the pure electron bandwidth). As the temperature increases, the effective mass of the polaron increases, and the bandwidth decreases. At sufficiently high temperature (of the order of the Debye temperature), however, transport is predominantly by a thermally activated hopping process, in which phonons are emitted and absorbed as the small polaron moves from site to site.

There is no agreement at this time as to which mechanism is present in each of the crytalline transition metal oxides, although recent experimental evidence for NiO favors the polaron, rather than the small polaron.[1]

Turning now to the situation in the glassy state, the theoretical picture is much less clear. Mott[1] has recently reviewed the current theory of electrons in a disordered lattice. There appears to be general agreement that, if the lattice is sufficiently disordered, and if the binding of the electrons to the lattice ions is sufficiently great, then all electron states in the solid will be localized. Localization means that each wave function will have a maximum about some site in the lattice, and that the envelope of the wave function on the average will decay exponentially with distance from that site. Conduction by band diffusion is impossible; thermally activated hopping with the emission and/or absorption of phonons is then required for

the electron to diffuse through the lattice. We note that the transition metal oxide containing glasses, as a result of the inherent tight binding of the d-electrons may be expected to exhibit localized states.

A rigorous treatment of the electron transport process in a three-dimensional glass is completely impossible at the present time. This is a result of the following:

(1) The lack of a detailed model for the glassy state. There are two conflicting models of the glassy state at the present time:[5] the microcrystalline model of the Russian School, and the random model of Zachariesen, which is generally held in the West. One point of agreement by both schools of thought is that the anion-cation complex present in the crystalline state (the metal ion with oxygen ions in octahedral coordination for the transition metal oxides) is maintained in at most a slightly distorted state. This point can be inferred from x-ray diffraction data,[6] and is supported by infrared studies.[7,8]

(2) The construction of electronic wave functions for a three-dimensional disordered lattice is a difficult problem, particularly in the absence of a specific model for a glass. Only recently have some papers appeared in an attempt to construct such wave functions.[9]

(3) There has been little success in constructing phonon wave functions in a disordered three-dimensional lattice.[10] Classical calculations do indicate that high frequency modes are localized in specific regions in the glass.[7,8]

We shall therefore limit our attention to a one-dimensional one-electron model. Here the tight binding model, which assumes that wave functions in the solid may be approximated by a linear combination

-6-

of the wave functions in the isolated atoms (or metal-oxygen complexes in our case). We shall furthermore use as a framework for our calculations, Holstein's small polaron approach.[5] The justification for this step is twofold:

(1) Even though the small polaron picture may not be applicable to the crystalline state, if there is sufficient disorder, it may be applicable to the glassy state. In the glassy state, the wave functions will be localized if there is sufficient disorder. Localization implies that the lattice outside the region where the electron is localized will be highly polarized, since that portion of the lattice will always see the field of the electron. Furthermore, the lattice inside the region of the localized electron will be somewhat polarized as a result of the exponential decay of the electron wave function. If the situation in the crystalline state is marginal; that is, near to assuming the small polaron configuration, then with sufficient disorder it may in fact assume the small polaron configuration. This possibility is further enhanced by the greater average separation of the metal ions in the glass in comparison to the crystalline state, and the presence of other species, resulting in decreased overlap of adjacent wave functions.

(2) Holstein's theory can be qualitatively extended to the normal polaron problem.

In Chapter II we shall therefore cast Holstein's model into a form suitable for an ionic lattice, and take into consideration the lack of periodicity. In Chapter III we shall apply the results of our calculations to the observed AC and DC conductivity data recently obtained on potassium vanadium phosphate glasses. Some additional implications of the model shall also be discussed.

2. THEORETICAL

Nearly Crystalline Ionic Model

In accordance with our previous discussion we shall develop the following model, which we shall refer to as the Nearly-Crystalline Ionic Model. Consider a one-dimensional non-periodic lattice consisting of alternating metal and oxygen ions (Figure 2). We shall assume that the forces acting on the ions are harmonic. In place of the unit cell which would concern us if we were discussing a crystalline model, we shall use the concept of a metal-oxide complex, consisting of a metal ion and the two adjacent oxygen ions. We shall consider our chain to have N complexes or 2N atoms. The analogy with a three-dimensional complex consisting of a metal ion and 6 oxygen ions in approximately octahedral coordination should be obvious.

In the following discussion we shall use the following notation: x will denote the electron coordinate, u_{ni} the displacement of the ith ion from its equilibrium position in the nth complex. We shall use the notation u_n to denote the triplet of displacements (u_{n-1}, u_{n0}, u_{n1}) and the notation u to denote the entire set of displacements of the 2N atoms. Our other notation will follow closely that used by Holstein.[5]

The Schrödinger equation for one electron in the lattice will be:

$$\hat{H}\psi = -\frac{\hbar}{i}\frac{\partial\psi}{\partial t} \qquad (1)$$
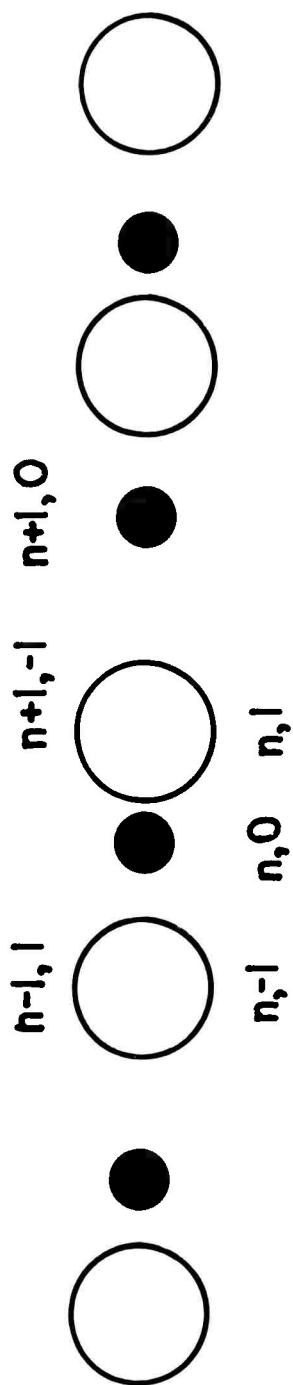
Figure 2. Nearly Crystalline Ionic Lattice.

where the Hamiltonian will be given by:

$$\hat{H} = \hat{H}_{electron} + \hat{H}_{lattice} + \hat{H}_{int} \qquad (2)$$

The electronic portion of the Hamiltonian is

$$\hat{H}_{electron} = -\frac{\hbar^2}{2m}\frac{\partial^2}{\partial x^2} + \sum_{n,i} U_i\,(x-R_{ni},\,u_{ni})$$

where $U_i\,(x-R_{ni},\,U_{ni})$ denotes the potential of the ith atom of the nth complex which is located at R_{ni} from the origin.

The lattice vibrational portion of the Hamiltonian will be given by:

$$\hat{H}_{lattice} = \sum_{\substack{n,i \\ \ell,j}}{}' \; -\frac{\hbar^2}{2M_i}\frac{\partial^2}{\partial u_{ni}^2} + g\begin{pmatrix} ni \\ \ell j \end{pmatrix} u_{ni}\,u_{\ell j}$$

In this expression, $g\begin{pmatrix} ni \\ \ell j \end{pmatrix}$ is the force constant acting between the ith atom of the nth complex and the jth atom of the ℓth complex. The primed sum indicates that the summation goes over each atom once; it is required due to the equivalence of $u_{n,-1}$ and $u_{n-1,1}$.

The interaction portion of the Hamiltonian $\hat{H}_{int}$ describes the interaction of the electron with the lattice vibrations and is contained in $\hat{H}_{electron}$ due to the explicit dependence of the U_i on the displacements.

We now wish to solve equation (1). To do so, we shall use the tight binding approximation which is appropriate for the narrow bands of the crystalline transition metal oxides. We consider first the nth isolated complex. The electronic wave functions will satisfy the following Schrödinger equation:

$$\left[-\frac{\hbar^2}{2m}\frac{\partial^2}{\partial x^2} + \sum_i U_i\,(x-R_{ni},\,u_{ni}) \right]\phi_n = E_n(u_n)\phi_n \qquad (3)$$

Both ϕ_n and $E_n(u_n)$ will depend on the displacements. We have chosen to explicitly display this for the $E_n(u_n)$. The wave function for the entire solid will be given by:

$$\psi = \sum_m a_m(u)\phi_m \tag{4}$$

Inserting equation (4) into equation (1) and making use of equation (3), we find:

$$-\frac{\hbar}{i}\sum_m \frac{\partial a_m(u)}{\partial t}\phi_m = \sum_n E_n(u_n)a_n(u)\phi_n + \sum_{\substack{n,i \\ t,j}}' \left[-\frac{\hbar^2}{2M_i}\frac{\partial^2}{\partial u_{ni}^2}\right.$$

$$\times a_m(u) + g\binom{n,i}{t,j}u_{ni}u_{tj}a_m(u)\Big]\phi_m + \sum_{\substack{n,i \\ m}}'\left[-\frac{\hbar^2}{2M_i}\right.$$

$$\times \left(2\frac{\partial a_m(u)}{\partial u_{ni}}\frac{\partial \phi_m}{\partial u_{ni}} + a_m(u)\frac{\partial^2 \phi_m}{\partial u_{ni}^2}\right)\Big] + \sum_{\substack{n,i \\ m\neq n}}' U_i(x-R_{ni},\ U_{ni})$$

$$\times \phi_m\, a_m(u) \tag{5}$$

We now multiply both sides of equation (5) by ϕ_p^* and integrate over all space with respect to the electronic coordinate x. In doing so, we shall come across integrals of the form:

$$T_{mp} = \int \phi_p^* \phi_m\, dx \tag{6}$$

Due to the localized nature of the ϕ wave functions which allows us to use the tight binding theory, we shall follow Holstein[5] and approx-image equation (6) by:

$$T_{mp} = \delta_{mp} \tag{7}$$

-11-

Equation (5) becomes:

$$-\frac{\hbar}{i}\frac{\partial a_p(u)}{\partial t} = E_p(u_p)a_p(u) + \sum_{\substack{n,i \\ p,j}}' \left[\frac{\hbar^2}{2M_i} \cdot \frac{\partial^2 a_p(u)}{\partial u_{ni}^2} + g\binom{ni}{pj} \right.$$

$$\left. \times u_{ni}u_{pj}a_p(u) \right] + \sum_{\substack{n,i \\ m}}' \left[-\frac{\hbar^2}{2M_i} \left(2\int \phi_p^* \frac{\partial a_m(u)}{\partial u_{ni}} dx \right. \right.$$

$$\left. \left. - \int \phi_p^* a_m(u) \frac{\partial^2 \phi_m}{\partial u_{ni}^2} dx \right) \right] + \sum_{\substack{n,i \\ m\neq n}}' \int \phi_p^* U_i (x-R_{ni}, u_{ni})$$

$$\times \phi_m dx \, a_m(u) \tag{8}$$

Consider the last sum in equation (8). Because of the localized nature of the three functions under the integral sign, we can approximate the integral as zero unless two functions refer to the same site, and the third refers to a neighboring site. Therefore, this sum becomes:

$$\sum_{\varepsilon\pm 1} \delta_{m,p+\varepsilon} \int \phi_p^* \sum_i U_i (x-R_{mi}, u_{mi}) \phi_p \, dx \, a_p(u)$$

$$+ \sum_{\varepsilon\pm 1} \delta_{p,m+\varepsilon} \int \phi_p^* \sum_i U_i (x-R_{pi}, u_{pi}) \phi_m \, dx \, a_m(u) \tag{9}$$

Next, consider the second sum of the right hand side of equation (8), which contains derivatives of the wave functions with respect to the nuclear displacements. These terms should be small (i.e., the displacements affect the wave functions only slightly), and we shall therefore follow Holstein[5] and set this entire term to zero. With these approximations, equation (8) becomes:

$$\left[-\frac{\hbar}{i}\frac{\partial}{\partial t} - \sum_{\substack{p,i \\ \ell,j}}' \left(-\frac{\hbar^2}{2M_i}\frac{\partial^2}{\partial u_{ni}^2} + g\binom{pi}{\ell j} \right) u_{pi}\, u_{\ell j} - E_n(u_n) \right.$$

$$\left. - W_n(u) \right] a_n(u) = \sum_{\varepsilon=\pm 1} \delta_{n,m+\varepsilon}\, J_{mn}(u)\, a_m(u) \qquad (10)$$

where:

$$W_n(u) = \sum_{\varepsilon=\pm 1}' \int \phi_n^* \sum_i U_i\,(x-R_{mi},\ U_{mi}) \phi_n \, dx \qquad (11)$$

$$J_{mn}(u) = \int \phi_n^* \sum_i U_i\,(x-R_{ni},\ U_{ni}) \phi_m \, dx \qquad (12)$$

Inspection of equations (11) and (12) shows that $W_n(u)$ represents the perturbation on the energy of the isolated complex $E_n(u_n)$ due to the neighboring complexes while $J_{mn}(u)$ is an overlap integral which will allow for transitions between the two adjacent sites.

Equation (10) is similar to that derived by Holstein. There are two important differences, however. First we see that the terms $E_n(u_n) + W_n(u)$ and $J_{mn}(u)$ are in general different for each site, due to the effects of disorder. Secondly the lattice vibration inter- action is written in a more general form.

A general solution to equation (10) is still impossible without further approximations. We shall therefore make the following simplifications:

$$M_1 = M_2 = M \qquad (13a)$$

$$g\binom{pi}{\ell j} = g \text{ (constant, between nearest} \qquad (13b)$$
$$\text{neighbors only)}$$

$$E_n(u_n) + W_n(u) = A_n - B_n u_{n,0} - C_n^1 (u_{n,1} - u_{n-1,1})$$

$$- C_n^2 (u_{n+1,0} - u_{n-1,0}) - C_n^3 (u_{n+1,1} - u_{n-2,1})$$

$$= A_n - B_n u_{n,0} - \sum_\ell C_n^\ell (u_\ell - u_{\delta(\ell)}) \tag{13c}$$

$$J_{nm}(u) = J_{nm} \quad (\text{constant}) \tag{13d}$$

Approximations (13a) and (13b) allow us to establish analytic normal coordinates for lattice vibrations. The problem reduces to 2N equal masses interconnected by springs of force constant g. In an actual glass the nearest neighbor force constants should be slightly different due to anharmonic terms in the lattice potential. This would reduce the problem to a nonanalytic problem in which the short wavelength modes become somewhat localized. By assuming the force constants are all equal, we shall therefore be assuming a strictly harmonic approximation. Assuming the masses equal restricts our phonon spectrum (Figure 3); however, in consideration of the large differences between one- and three-dimensional spectra, and in light of the success of the Debye approximation, which is similar in its effects as our approximation, we expect qualitative agreement between our model and reality.

The approximation of the energies as being linearly related to the displacements of the ions appears to be standard in polaron theory. It allows the problem to be recast into displaced normal coordinates, as we shall see. Inclusion of higher order terms would recouple the phonon modes which the normal coordinates decouple, and hence shift the phonon frequencies. The approximation (13c) therefore corresponds to a series expansion of the energy about zero displacement and the
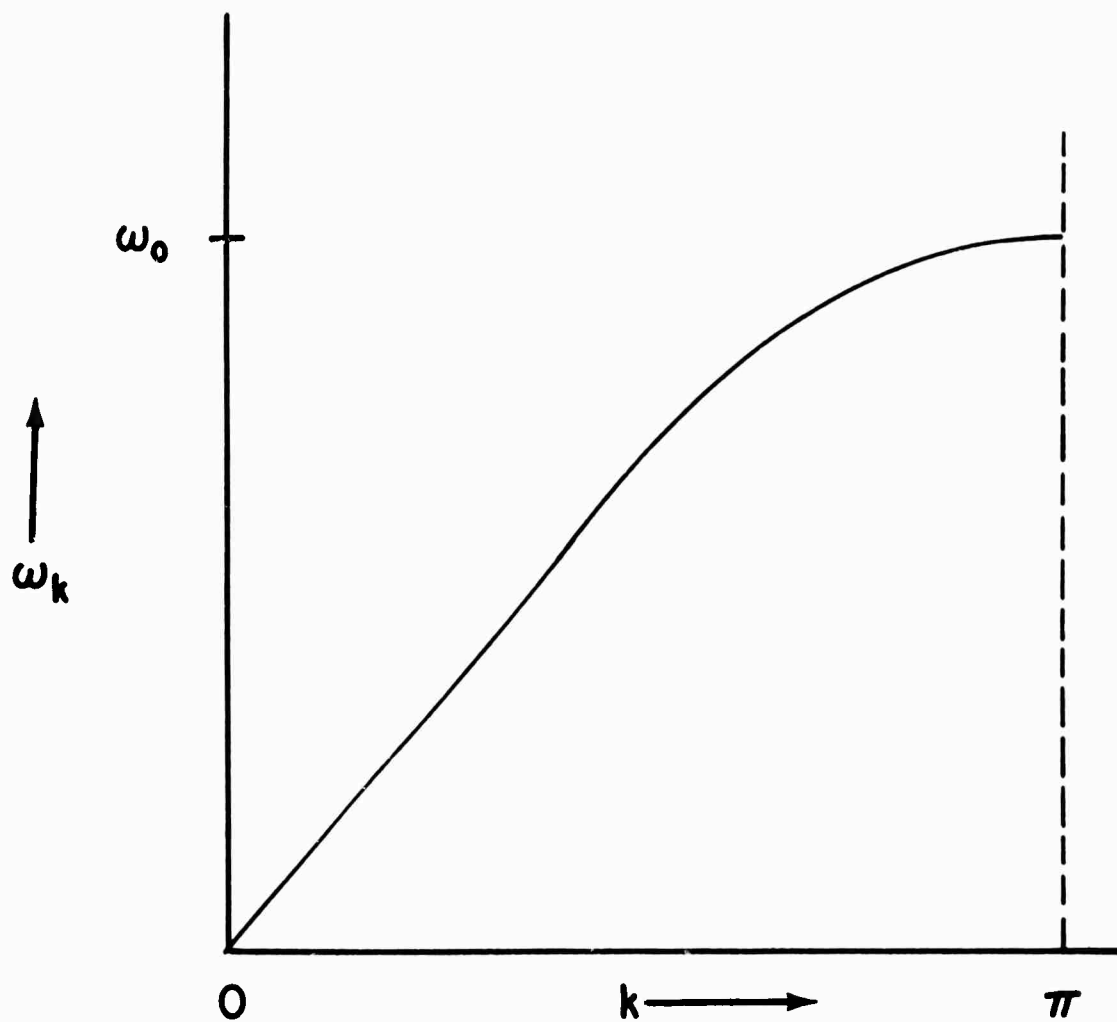
Figure 3. Plot of ω_k versus k.

ignoring of nonlinear terms. The term A_n reflects that different sites have different energy. The B_n term yields the shift of energy due to the displacement of the metal ion of the site on which the electron is located. The C_n^1 yields the effect of displacement of nearest neighbor oxygen ions, C_n^2 of nearest neighbor metal ions, and so on. We shall see that the B_n term yields essentially meaningless results, but we include it as it is similar to Holstein's approximation.[5]

Finally, the approximation (13d) states that we shall ignore the effect of displacements on the overlap integral, and is justified in view of the smallness of J_{mn}.

With the approximations of equation (13), equation (10) may be rewritten.

$$\left[-\frac{\hbar}{i} \frac{\partial}{\partial t} - \sum_{p,i}' \left(-\frac{\hbar^2}{2M} \frac{\partial^2}{\partial u_{pi}^2} + \frac{1}{2} g \, (u_{p,i} - u_{p,i-1})^2 \right) - A_n \right.$$

$$\left. - B_n \, u_{n,0} - \sum_{\ell} C_n^{\ell} \, (u_{\ell} - u_{\delta(\ell)}) \right] a_n(u) = \sum_{\epsilon = \pm 1} \delta_{n,m+\epsilon}$$

$$\times J_{nm} \, a_m(u) \tag{14}$$

We transform to normal coordinates by setting:

$$u_{ni} = \sum_k \left(\frac{1}{N} \right)^{1/2} q_k \sin \left((2n+1)k + \frac{\pi}{4} \right) \tag{15}$$

In doing so, we find the frequencies given by:

$$\omega_k^2 = \omega_o^2 \, (\sin^2 \tfrac{1}{2} \, k); \quad \omega_o = 2\sqrt{\tfrac{g}{M}} \tag{16a}$$

with:

$$k = \frac{\pi \ell}{2N}; \quad \text{where } \ell \text{ is an integer in the interval} \tag{16b}$$
$$-2N \leq \ell \leq 2N$$

Substitution of equation (15) into equation (14) yields

$$\left[-\frac{\hbar}{i}\frac{\partial}{\partial t} - \sum_k \left(-\frac{\hbar^2}{2M} + \frac{1}{2}M\,\omega_k^2\,q_k^2 \right) - A_n + B_n \sum_k \left(\frac{1}{N}\right)^{1/2}\!\!\left(q_k \sin(2nk + \tfrac{\pi}{4}) \right) \right.$$

$$+ C_n^1 \sum_k \left(\frac{1}{N}\right)^{1/2} q_k \left(\sin[(2n+1)k + \tfrac{\pi}{4}] - \sin[(2n-1)k + \tfrac{\pi}{4}] \right)$$

$$+ C_n^2 \sum_k \left(\frac{1}{N}\right)^{1/2} q_k \left(\sin[(2n+2)k + \tfrac{\pi}{4}] - \sin[(2n-2)k + \tfrac{\pi}{4}] \right)$$

$$\left. + \ldots \right] a_n(q) = \sum_{\epsilon=\pm 1} \delta_{n,m+\epsilon}\, J_{nm}\, a_m(q) \qquad (17)$$

Collecting terms involving q_k, and completing the square to obtain a term of the form $(q_k - q_k^{(n)})$ we find:

$$\left[-\frac{\hbar}{i}\frac{\partial}{\partial t} - \sum_k \left(-\frac{\hbar^2}{2M}\frac{\partial^2}{\partial q_k^2} + \frac{1}{2}M\,\omega_k^2\,(q_k - q_k^{(n)})^2 \right) - E_b^{(n)} \right] a_n(q)$$

$$= \sum_{\epsilon=\pm 1} J_{mn}\, \delta_{n,m+\epsilon}\, a_m(q) \qquad (18)$$

where:

$$q_k^{(n)} = \left(\frac{1}{N}\right)^{1/2} \omega \frac{1}{M\omega_k^2} \left[B_n \sin(2nk + \tfrac{\pi}{4}) + \sum_\ell C_n^\ell \sin 2\ell k \right.$$

$$\left. \times \cos(2nk + \tfrac{\pi}{4}) \right] \qquad (19)$$

and:

$$E_b^{(n)} = A_n + \sum_k \frac{1}{2NM\omega_k^2} \left[B_n \sin(2nk + \tfrac{\pi}{4}) + \sum_\ell C_n^\ell \sin 2\ell k \right.$$

$$\left. \times \cos(2nk + \tfrac{\pi}{4}) \right]^2 \qquad (20)$$

Equation (20) represents the polaron binding energy. We now treat J_{mn} as a small perturbation. To obtain our first order results, we set $J_{mn} = 0$. We obtain the equation:

$$-\frac{\hbar}{i} \frac{\partial \chi^P(q)}{\partial t} = \sum_k \left[-\frac{\hbar^2}{2M} \frac{\partial^2}{\partial q_k^2} + \frac{1}{2} M \omega_k^2 (q_k - q_k^{(p)})^2 \right] \chi^P(q) \tag{21}$$

Equation (21) is the equation for a set of decoupled displaced harmonic oscillators. The solution is:

$$\chi^P(q) = \pi_k \left[\phi_{N_k} \left(\left[\frac{M\omega_k}{\hbar} \right]^{1/2} (q_k - q_k^{(p)}) \right) \right] \exp \left(-\frac{itE_N^P}{\hbar} \right) \tag{22}$$

where:

$$E_N^P = \sum_k h \omega_k (N_k + \frac{1}{2}) + E_b^{(p)} \tag{23a}$$

$$\phi_N(z) = (2^N N! \pi^{1/2})^{-1/2} e^{-z^2/2} H_N(z) \tag{23b}$$

In equations (23), N_k is the occupation number of the kth mode with frequency ω_k, and the $H_N(z)$ are the Hermite polynomials.

We now "turn on" the perturbation J_{mn}. We look for solutions of the form:

$$a_n(q) = \sum_{p,N} C(p,N) a_{p,N}(n,q) \tag{24}$$

with

$$a_{p,N}(n,q) = \delta_{np} \chi^P(q) \exp \left(-\frac{itE_N^P}{\hbar} \right) \tag{24a}$$

Inserting equation (24) into equation (18) we find:

$$-\frac{\hbar}{i} \sum \frac{\partial C(p,N)}{\partial t} a_{p,N}(n,q) \exp \left(-\frac{itE_N^P}{\hbar} \right) = \sum_{\varepsilon = \pm 1} \delta_{n,m+\varepsilon} J_{mn}$$

$$\times C(p',N') a_{p',N'}(m,q) \exp \left(-\frac{itE_{N'}^{P'}}{\hbar} \right) \tag{25}$$

Multiplying both sides of equation (25) by the complex conjugate of equation (24a), and integrating with respect to all q_k:

$$-\frac{\hbar}{i}\frac{\partial C(p,N)}{\partial t} = \sum_{p',N'} (pN|V|p'N')\, C(p',N')\, \exp\left(\frac{it}{\hbar}\right.$$

$$\left. \times\, (E_N^p - E_{N'}^{p'}) \right) \tag{26}$$

with:

$$(p,N|V|p'N') = \sum_{\varepsilon=\pm 1} J_{pp'}\, \delta_{p,p'+\varepsilon}\, \pi_k \int \phi_{N_k}\left[\left(\frac{M\omega_k}{\hbar}\right)^{1/2}\right.$$

$$\left. \times\, (q_k - q_k^{(p)})\right] \phi_{N_k'}\left[\left(\frac{M\omega_k}{\hbar}\right)^{1/2}(q_k - q_k^{(p')})\right]\left(\frac{M\omega_k}{\hbar}\right) dq_k \tag{27}$$

To evaluate equation (27), we expand $\phi_{N_k}\left[\left(\frac{M\omega_k}{\hbar}\right)^{1/2}(q_k - q_k^{(p')})\right]$ in a power series about $q_k^{(p)} - q_k^{(p')} = 0$. We find:

$$\phi_{N_k}\left[\left(\frac{M\omega_k}{\hbar}\right)^{1/2}(q_k - q_k^{(p')})\right] = \phi_{N_k}\left[\left(\frac{M\omega_k}{\hbar}\right)^{1/2}(q_k - q_k^{(p)})\right]$$

$$+ \left.\frac{\partial \phi_{N_k}(z)}{\partial z}\right|_{z=\left(\frac{M\omega_k}{\hbar}\right)^{1/2}(q_k - q_k^{(p)})} \left(\frac{M\omega_k}{\hbar}\right)^{1/2}(q_k^{(p')} - q_k^{(p)})$$

$$+ \frac{1}{2}\left.\frac{\partial^2 \phi_{N_k}(z)}{\partial z^2}\right|_{z=\left(\frac{M\omega_k}{\hbar}\right)^{1/2}(q_k - q_k^{(p)})} \left(\frac{M\omega_k}{\hbar}\right)(q_k^{(p')}$$

$$- q_k^{(p)})^2 + \dots \tag{28}$$

and making use of the relation:

$$\frac{\partial \phi_{N_k}(z)}{\partial z} = \left(\frac{N_k}{2}\right)^{1/2}\phi_{N_{k-1}}(z) - \left(\frac{N_k+1}{2}\right)^{1/2}\phi_{N_{k+1}}(z) \tag{28a}$$

Equation (28) becomes:

$$\Phi_{N_k'}\left[\left(\frac{M\omega_k}{\hbar}\right)^{1/2}(q_k - q_k^{(p')})\right] = \Phi_{N_k'}\left[\left(\frac{M\omega_k}{\hbar}\right)^{1/2}(q_k - q_k^{(p)})\right]$$

$$+ \left(\frac{N_k'}{2}\right)^{1/2}\Phi_{N_k'-1}\left[\left(\frac{M\omega_k}{\hbar}\right)^{1/2}(q_k - q_k^{(p)})\right] - \left(\frac{N_k'+1}{2}\right)^{1/2}$$

$$\times \Phi_{N_k'+1}\left[\left(\frac{M\omega_k}{\hbar}\right)^{1/2}(q_k - q_k^{(p)})\right]\left(\frac{M\omega_k}{\hbar}\right)^{1/2}(q_k^{(p')} - q_k^{p})$$

$$- \frac{1}{2}(N_k' + \frac{1}{2})\Phi_{N_k'}\left[\left(\frac{M\omega_k}{\hbar}\right)^{1/2}(q_k - q_k^{(p)})\left(\frac{M\omega_k}{\hbar}\right)(q_k^{(p')} - \right.$$

$$- q_k^{(p)})^2 + \text{higher order terms} \qquad (28b)$$

Evaluating the integral appearing on the right hand side of equation
(27), and using the orthonormality relation:

$$\int_{-\infty}^{\infty} \Phi_{N_k}(z)\,\Phi_{N_k'}(z)\,dz = \delta_{N_k,N_k'} \qquad (28c)$$

We find:

$$\int_{-\infty}^{\infty} \Phi_{N_k}\left[\left(\frac{M\omega_k}{\hbar}\right)^{1/2}(q_k - q_k^{(p)})\right]\Phi_{N_k'}\left[\left(\frac{M\omega_k}{\hbar}\right)^{1/2}(q_k - q_k^{(p')})\right]$$

$$\times \left(\frac{M\omega_k}{\hbar}\right)dq_k = \left[1 - \frac{1}{2}(N_k + \frac{1}{2})\left(\frac{M\omega_k}{\hbar}\right)(q_k^{(p')} - q_k^{(p)})^2\right]$$

$$\times \delta_{N_k,N_k'} + \left[\left(\frac{N_k'}{2}\right)^{1/2}\left(\frac{M\omega_k}{\hbar}\right)^{1/2}(q_k^{(p')} - q_k^{(p)})\right]\delta_{N_k,N_{k-1}'}$$

$$- \left[\left(\frac{N_k'+1}{2}\right)^{1/2}\left(\frac{M\omega_k}{\hbar}\right)(q_k^{(p')} - q_k^{(p)})\right]\delta_{N_k,N_{k+1}'} + \cdots$$

$$(29)$$

-20-

We can evaluate $(q_k^{(p')} - q_k^{(p)})$ from equation (19):

$$(q_k^{(p')} - q_k^{(p)}) = \left(\frac{1}{N}\right)^{1/2} \frac{1}{M\omega_k^2} \left[B_{p'} \sin(2p'k + \frac{\pi}{4}) \right.$$

$$\left. + \sum_\ell c_{p'}^\ell \sin 2\ell k \cos (2p'k + \frac{\pi}{4}) \right]$$

$$- \left(\frac{1}{N}\right)^{1/2} \frac{1}{M\omega_k^2} \left[B_p \sin(2pk + \frac{\pi}{4}) \right.$$

$$\left. + \sum_\ell c_p^\ell \sin 2\ell k \cos(2pk + \frac{\pi}{4}) \right] \qquad (30)$$

To proceed further, we need to place

$$B_{p'} = B_p - B$$

$$c_{p'}^\ell = c_p^\ell = c^\ell \qquad (31)$$

This assumption is equivalent to saying that the lattice-electron coupling is the same in all complexes. While not exactly true, we expect the coupling to be nearly the same in all complexes. Using equations (31), we can rewrite equation (30):

$$(q_k^{(p')} - q_k^{(p)}) = \left(\frac{1}{N}\right)^{1/2} \frac{2 \sin k\varepsilon}{M\omega_k^2} \left[B \cos [(k(p+\varepsilon) + \frac{\pi}{4}) \right.$$

$$\left. - \sum_\ell c^\ell \sin 2\ell k \sin [k(p+\varepsilon) + \frac{\pi}{4}] \right] \qquad (32)$$

where $p' = p + \varepsilon$

In the following discussion we shall deal with two cases:

Case I $\quad B = 0$

$$\gamma_k = \frac{\sin^2 k}{M\omega_k^2 \hbar\omega_k} \left[\sum_\ell c^\ell \sin 2\ell k \right]^2 \qquad (33a)$$

-21-

<u>Case II</u> $(\sum_{\ell} C_\ell \sin 2\ell k) = 0$

$$\gamma_k = \frac{B^2 \sin^2 k}{M\omega_k^2 \hbar \omega_k} \tag{33b}$$

We make use of equations (33), (32) and (29) and rewrite equation (27) as:

$$
(pN|V|p'N') = \sum_{\varepsilon=\pm 1} J_{pp'} \, \delta_{p,p+} \, \pi_k \Bigg\{ \left[1 - \left(\frac{2}{N}\right)\left(N_k + \frac{1}{2}\right)\gamma_k \right.
$$

$$
\left. \times \sin^2[k(p+\varepsilon) + \frac{\pi}{4}] \right] \delta_{N_k,N_k'} + \left(\frac{2N_k'}{N}\right)^{1/2} \gamma_k^{1/2}
$$

$$
\times \sin[k(p+\varepsilon) + \frac{\pi}{4}] \, \delta_{N_k,N_{k+1}'} - \left(\frac{2(N_k+1)}{N}\right)^{1/2}
$$

$$
\times \gamma_k^{1/2} \sin[k(p+\varepsilon) + \frac{\pi}{4}] \, \delta_{N_k,N_{k-1}'} \Bigg\} \tag{34}
$$

for Case I. For Case II the sine terms are replaced by cosines of the same argument.

Solution for Crystalline Lattice

In anticipation of difficulties which we shall encounter when we treat the disordered case, we shall first treat the crystalline lattice first. In doing so we find that approximations (13b) and (31) become exact, and that all of the A_n's of equation (13c) become equation, making all the $E_b^{(p)}$'s of equations (20) and (23a) equal. We restrict our attention to the case when all N_k's remain unchanged. Using equation (34), equation (26) becomes

$$-\frac{\hbar}{i}\frac{\partial C(p,N)}{\partial t} = \sum_{\varepsilon=\pm 1} J_{pp'} \, \delta_{p,p'+\varepsilon} \, \pi_k \left[1 - \left(\frac{2}{N}\right)\left(N_k + \frac{1}{2}\right)\gamma_k \right.$$

$$\left. \times \sin^2[k(p+\varepsilon) + \frac{\pi}{4}] \right] C(p',N) \tag{35}$$

We note that each of the terms inside the product bracket will be nearly unity, since the N term is much greater than N_k. Hence we can approximate

$$1 - a \approx e^{-a} \tag{36a}$$

and

$$\pi_k \, (1 - a_k) \approx e^{-\sum_k a_k} \tag{36b}$$

Equation (35) therefore becomes

$$-\frac{\hbar}{i}\frac{\partial C(p,N)}{\partial t} = \sum_{\varepsilon=\pm 1} J_{pp'} \, \delta_{p,p'+\varepsilon} \, e^{-S(T)} \, C(p',N) \tag{37}$$

where

$$S(T) = \sum_k \frac{2\gamma_k}{N} \sin^2[k(p+\varepsilon) + \frac{\pi}{4}] \, (N_k + \frac{1}{2}) \tag{38}$$

Since for every k there is a -k

$$S(T) = \sum_k \frac{\gamma_k}{N} \, (N_k + \frac{1}{2}) \tag{38a}$$

We can now replace N_k by $(\exp \beta\hbar\omega_k - 1)^{-1}$, where $\beta = 1/kT$. Equation (38) becomes

$$S(T) = \sum_k \frac{\gamma_k}{2N} \coth \frac{\beta\hbar\omega_k}{2} \tag{38b}$$

-23-

Assuming a time dependence of exp $\left(\frac{itE}{\hbar}\right)$ of the $C(p,N)$, equation (37) becomes

$$E \ C(p,N) \ = \ J e^{-S(T)} \ C(p'+1,N) + C(p-1,N) \qquad (39)$$

where we have made use of the fact that $J_{p,p+1} = J_{p,p-1} = J$ for the crystalline case. The solution to equation (39) will be

$$C(p,N) \ = \ e^{i\sigma p} \qquad (40)$$

because of the periodicity. The energy will be given by:

$$E \ = \ 2J \cos \sigma \exp [-S(T)] \qquad (40a)$$

The $C(p,N)$ assures that our solutions are of the required Bloch form.

Solution for Disordered Lattices

We are now against one of the most formidable problems in contempory theoretical physics, and one for which there is not a complete methematical solution as of now. We are therefore forced to anticipate the results of a theoretical solution.

We can prove that in our problem localized states may be formed. This can be seen by writing equation (26) for the case when $N = N'$:

$$-\frac{\hbar}{i} \frac{\partial}{\partial t} \left[C(p,N) \exp\left(-\frac{itE_N^p}{\hbar} \right) \right] = E_N^p \ C(p,N) \exp\left(-\frac{itE_N^p}{\hbar} \right)$$

$$+ \sum_{p'} \ (pN|V|p'N) \ C(p'N) \exp\left(-\frac{itE_N^{p'}}{\hbar} \right) \qquad (26a)$$

By taking $N = N'$, $\sum_k (N_k + \frac{1}{2})\hbar\omega_k = \sum_k (N_k' + \frac{1}{2})\hbar\omega_k$. Therefore, by equation (23a) and equation (20), equation (26a) becomes

$$- \frac{\hbar}{i} \frac{\partial}{\partial t}\left[C(p,N)\ \exp\left(- \frac{itA_p}{\hbar}\right)\right] = A_p\ C(p,N)\ \exp\left(- \frac{itA_p}{\hbar}\right)$$

$$+ \sum_{p'} (pN|V|p'N)\ C(p'N)\ \exp\left(- \frac{itA_p}{\hbar}\right) \qquad (26b)$$

Equation (26b) is identical to that of Anderson,[11] and we may use the results of his theorem, that if $\frac{\langle A \rangle}{J} e^{S(T)}$ is sufficiently large, all states will be localized (in the sense that nonthermally activated diffusion is absent). Here $\langle A \rangle$ represents the deviation of the A_n.

The problem of solving for these localized states is considerably more complicated, however. To circumvent this problem, we note that in the development up to equation (35), no use was made of the energy differences on different sites, other than to carry it in the time development exponential. Furthermore, we note that until this point, the local site variable p appears only through the electron-phonon coupling term, in the displaced normal coordinate $q_k^{(p)}$.

We therefore propose to handle the disorder in the following manner:

1. We begin by taking the crystalline lattice as our first approximation, that is, the J's are all taken equal, and the A_n's all equal.

2. At this point we introduce disorder into the problem. The energy difference in the A_n's will now appear in the solution for our $C(p,N)$'s. We can also allow our J's to be different; the differences will affect our solution for $C(p,N)$

3. At this point we can follow Mott,[1] and take as the solution for $C(p,N)$ to be:

$$C^r(p,N) = F(r,p) \, e^{-\gamma_r \left| S_p - S_r \right|} \qquad (41)$$

that is, a state localized on site r located at S_r. The justification for this assumption has been summarized by Mott:

a. The solutions to the random Kronig-Penney model and the random δ-well model are of this type provided there is sufficient disorder.[12,13]

b. The wave functions of impurity atoms in semiconductors are of this type. The theory of impurity semiconductors shows that the wave functions of the impurity atoms are localized due to random fields.[14] Furthermore, the impurity conduction is found to fit Anderson's criteria. We should point out that our current problem is akin to impurity conduction experimentally.

We shall anticipate testing the validity of this assumption by comparison of our theory with experimental results.

Inspection of the results of the disordered Kronig-Penney and disordered δ-well models shows that $F(r,p)$ will be highly sensitive to local structure; the important point is that the envelope of $C^r(p,N)$ will fall off exponentially on either side of the localized center.

The physical meaning of equation (41) is that in the disordered lattice the small polaron will not be confined to one site. Even though adjacent sites have different energy, the polaron will tunnel to adjacent sites, or equivalently, will "resonate," in the sense used by Pauling,[15] with them.

-26-

As in the crystalline case, the $C^r(p,N)$ will be defined only on a site. Also, since equation (41) will represent the steady state solution of the problem, the $C^r(p,N)$ must be orthonormal; i.e.,

$$\sum_p F^*(r'p) \exp\left(-\gamma_{r'}\left|S_p - S_{r'}\right|\right) F(r,p) \exp\left(-\gamma_r\left|S_p - S_r\right|\right)$$

$$= \delta_{rr'} \qquad (42)$$

To each localized state there will be an energy V_r which is the counterpart of E in equation (40a) for the crystalline case. V_r will now contain the energy shifts due to disorder.

Now we wish to calculate the transition rate for a polaron in a localized state at r to jump to a localized state at site r'. This problem is not equivalent to a calcuation for a jump from a polaron on site r to a polaron on site r', because the eigensolutions to our problem are spread out due to tunneling.

The total wave function for a polaron in a localized state on site r will be given by

$$a_n^r(N) = \sum_p F(r,p) \exp\left(-\gamma_r\left|S_p - S_r\right|\right) \delta_{np} \, \phi_{N_k}\left[\left(\frac{M\omega_k}{\hbar}\right)^{1/2}\right.$$

$$\left. \times \, (q_k - q_k^{(p)})\right] \exp\left[\left(-\frac{it}{\hbar}\right)\left(A + \sum_k (N_k + \frac{1}{2}) \, \hbar\omega_k\right.\right.$$

$$\left.\left. + E_b + V_r\right)\right] \qquad (43)$$

Also of interest is the fact that

$$
\int \sum_n a_n^{*r}(N)\, a_n^{r'}(N')\,dq = \sum_p F^*(r,p)\, F(r',p)\, \exp\left(-\gamma_{r'}\right.
$$

$$
\times \left|S_p - S_{r'}\right|\right) \exp\left(-\gamma_r\left|S_p - S_r\right|\right) \pi_k \left\{\int \phi_{N_k}^* \left[\left(\frac{M\omega_k}{\hbar}\right)^{1/2}\right.\right.
$$

$$
\times \left.(q_k - q_k^{(p)})\right] \phi_{N_{k'}}\left[\left(\frac{M\omega_k}{\hbar}\right)^{1/2}(q_k - q_k^{(p)})\right]dq_k \, \exp\left[\left(\frac{it}{\hbar}\right)\right.
$$

$$
\times \left.\left(V_r - V_{r'} - \sum_k \Delta N_k \hbar\omega_k\right)\right]\right\} = \delta_{rr'}\,\delta_{NN'} \tag{44}
$$

by virtue of equations (42) and (28c). In other words, a polaron cannot hop from one localized state to another without hopping from one site to another at the same time.

To return to the problem, we wish to computer the transition rate from a state localized at r to one localized at r'. We take as our wave functions:

$$
a_n(q) = \sum_{r',N'} Q_n(r',N')\, a_n^{r'}(N') \tag{45}
$$

Substituting equation (45) into equation (17), with a reminder that all A_n's are equal, multiplying both sides by $a_n^{*r}(N)$, integrating over all q_k, we find:

$$
-\frac{\hbar}{i}\frac{\partial Q_n(rN)}{\partial t} = \sum_{n',N',r'} (nN|V|n'N')\, Q_{n'}(r'N')\, F^*(r,n)
$$

$$
\times F(r'n')\, \exp\left(-\gamma_r\left|S_n - S_r\right|\right) \exp\left(-\gamma_{r'}\left|S_{n'} - S_{r'}\right|\right)
$$

$$
\times \exp\left[\left(\frac{it}{\hbar}\right)\left(V_r - V_{r'} + \sum_k \Delta N_k \hbar\omega_k\right)\right] \tag{46}
$$

where $(nN|V|n'N')$ is given by equation (34). The transition rate from state r to r' via a jump from $n \rightarrow n \pm 1$ is given by time dependent perturbation theory:

$$W^{r \rightarrow r'}(nN \rightarrow n'N') = \frac{2}{\hbar^2} H(r,r',n,n') \left| (nN|V|n'N') \right|^2$$

$$\times \frac{\partial}{\partial t} \Omega \left(\sum_k \hbar\omega_k(N_k' - N_k) + \Delta E \right) \qquad (47)$$

where:

$$\Delta E = V_r - V_{r'} \qquad (47a)$$

$$\Omega(x) = \frac{1 - \cos\left(\frac{xt}{\hbar}\right)}{\left(\frac{xt}{\hbar}\right)^2} \qquad (47b)$$

$$\frac{\partial}{\partial t} \Omega(x) = \frac{1}{2} \int_{-t}^{t} e^{ixt/\hbar} \, dt \qquad (47c)$$

$$H(r,r',n,n') = \left| F^*(r,n) \, F(r'n') \, e^{-\gamma_r |S_n - S_r| - \gamma_{r'} |S_{n'} - S_{r'}|} \right|^2 \qquad (47d)$$

Substituting equation (34) into (47), we find

$$W^{r \rightarrow r'}(nN \rightarrow n'N) = \frac{1}{\hbar^2} \sum_{\epsilon = \pm 1} J^2 \, \delta_{n,n'+\epsilon} \, H(r,r',n,n')$$

$$\times \int_{-t}^{t} \pi_k \left\{ \left[1 - \left(\frac{2}{N}\right)\gamma_k \, (N_k + \tfrac{1}{2}) \sin^2[k(n+\epsilon) + \tfrac{\pi}{4}] \right]^2 \right.$$

$$\left. + 2\gamma_k \left[\frac{N_k}{N} e^{-i\omega_k t} - \frac{N_k+1}{N} e^{i\omega_k t} \right] \sin^2[k(n+\epsilon) + \tfrac{\pi}{4}] \right\}$$

$$\times e^{i\Delta E t/\hbar} \, dt \qquad (48)$$

Completing the square in equation (48) and ignoring the term in $\sin^4(\ )$ since it is of order $1/N^2$, and making use of equations (36a), (36b) and replacing N_k by $(\exp \beta\hbar\omega_k - 1)^{-1}$;

$$W^{r \to r'}(n \to n') = \frac{1}{\hbar^2} \sum_{\varepsilon \pm 1} J^2 \, \delta_{n,n'\pm\varepsilon} \, H(r,r',n,n')$$

$$\times \exp[-2S(T)] \int_{-t}^{t} \exp\left(\frac{i\Delta Et}{\hbar}\right) \exp\left[+\sum_{k} \frac{\gamma_k}{N}\left(\coth\frac{\beta\hbar\omega_k}{2}\right.\right.$$

$$\left.\left.\times \cos \omega_k t + i \sin \omega_k t\right)\right]dt \tag{49}$$

The term $S(T)$ is given by equation (38a).

Low Temperature Approximation

An expression valid at low temperatures will be of interest in discussing the AC conductivity. Inspection of the second exponential in equation (49) shows that at low temperatures it will remain finite, and hence we expand it in a power series and obtain:

$$W^{r \to r'}(n \to n\pm1) = \frac{J^2}{\hbar^2} \exp[-2S(T)]\, H(r,r',n,n\pm1) \left\{ \frac{\sin \frac{\Delta E t}{\hbar}}{\frac{\Delta E}{\hbar}} \right.$$

$$+ \sum_k \left[\frac{\gamma_k}{N}\, e^{\beta\hbar\omega_k}\, \frac{\sin\left(\frac{\Delta E}{\hbar} + \omega_k\right)t}{\frac{\Delta E}{\hbar} + \omega_k} + \frac{\sin\left(\frac{\Delta E}{\hbar} - \omega_k\right)t}{\frac{\Delta E}{\hbar} - \omega_k} \right]$$

$$\times \frac{1}{e^{\beta\hbar\omega_k} - 1} + \sum_{k,k'} \frac{\gamma_k \gamma_{k'}}{N^2} \left[e^{\beta\hbar(\omega_k+\omega_{k'})} \right.$$

$$\times \frac{\sin\left(\omega_k + \omega_{k'} + \frac{\Delta E}{\hbar}\right)t}{\omega_k + \omega_{k'} + \frac{\Delta E}{\hbar}} + e^{\beta\hbar\omega_{k'}}\, \frac{\sin\left(\omega_{k'} + \frac{\Delta E}{\hbar} - \omega_k\right)t}{\omega_{k'} - \omega_k + \frac{\Delta E}{\hbar}}$$

$$+ \frac{e^{\beta\hbar\omega_k} \sin\left(\omega_k - \omega_{k'} + \frac{\Delta E}{\hbar}\right)t}{\omega_k - \omega_{k'} + \frac{\Delta E}{\hbar}} + \frac{\sin\left(\frac{\Delta E}{\hbar} - \omega_k - \omega_{k'}\right)t}{\frac{\Delta E}{\hbar} - \omega_k \omega_{k'}} \right]$$

$$\left. \frac{1}{\left(e^{\beta\hbar\omega_k} - 1\right)\left(e^{\beta\hbar\omega_{k'}} - 1\right)} + \ldots \right\} \tag{50}$$

Now letting t approach ∞, which is valid if we are considering only low frequency applied fields; the terms (sin xt/x) will be replaced by $2\pi\delta(x)$. The first term in the brackets of equation (50) vanishes. This term represents transitions which do not involve phonon emission or absorption and has been considered previously. The second term (single sum) represents one-phonon processes; the third term (double sum), two-phonon processes, and higher order terms will represent multi-phonon processes. At low temperatures, only those modes where $\hbar\omega_k \ll kT$ will be activated, and from equation (33a) we see that the γ_k for these modes is small. Hence we can confine our attention to single phonon processes, as two phonon processes are of order γ_k^2. We can therefore write:

One Phonon Emission:

$$W^{r \to r'}(n \to n\underline{+}1) \;=\; \frac{2\pi J^2}{\hbar^2} \exp\,[-2S(T)]\; H(r,r',n,n\underline{+}1)$$

$$\times \; \sum_k \frac{\gamma_k}{N} \frac{e^{\beta\hbar\omega_k}}{e^{\beta\hbar\omega_k} - 1}\; \delta\left(\frac{\Delta E}{\hbar} + \omega_k\right) \tag{51a}$$

One Phonon Absorption:

$$W^{r \to r'}(n \to n\underline{+}1) \;=\; \frac{2\pi J^2}{\hbar^2} \exp\,[-2S(T)]\; H(r,r',n,n\underline{+}1)$$

$$\times \; \sum_k \frac{\gamma_k}{N} \left(e^{\beta\hbar\omega_k} - 1\right)^{-1} \delta\left(\frac{\Delta E}{\hbar} - \omega_k\right) \tag{51b}$$

In considering transport through a random lattice we should have at equilibrium an equal number of emissions as absorptions. With this criteria we can combine equations (51a) and (51b) to obtain:

$$W^{r \to r'}(n \to n\underline{+}1) \;=\; \frac{2\pi J^2}{\hbar^2} \exp\left[-2S(T)\right] H(r,r',n,n\underline{+}1)$$

$$\times \; \sum \frac{\gamma_k}{N} \coth\frac{\beta\hbar\omega_k}{2}\; \delta\left(\frac{\Delta E}{\hbar} \pm \omega_k\right) \tag{52}$$

To determine the total transition rate from r to r', we must sum over all n, as equation (52) gives only the transition rate from r to r' via a jump from site n to site n $\pm$ 1. As can be seen from equation (52) the only n dependent term is $H(r,r',n,n\underline{+}1)$. Let the sites r and r' be separated by a distance R; i.e.,

$$\left| S_r - S_i \right| \;=\; R \tag{53}$$

Therefore we can compute:

$$\sum_n H(r,r',n,n\pm1) = \sum_n \left| F*(r,n)\, F(r',n\pm1)\, e^{-\gamma_r\left|S_n - S_r\right|} \right.$$

$$\times \left. e^{-\gamma_{r'}\left|S_{n\pm1} - S_{r'}\right|} \right|^2 \tag{54}$$

If we now assume that most of the contribution to the sum comes from the region between the two centers, which is reasonable if R is great enough, since on either side of the centers we will have the product of two exponentially decreasing functions, equation (54) can be rewritten as

$$\sum_n H(r,r',n,n\pm1) = \sum_n \left| F*(r,n)\, F(r',n\pm1) \right|^2 e^{-2(\gamma_r - \gamma_{r'})S_n}$$

$$\times e^{-2(\gamma_r + \gamma_{r'})R}\, e^{\pm2(\gamma_r - \gamma_{r'})a} \tag{54}$$

where $\pm a$ is the distance between site n and site n + 1. If we are looking at an average process, we can write $\gamma_r = \gamma_{r'} = \gamma$.

$$\sum_n H(r,r',n,n\pm1) = \sum_n \left| F*(r,n)\, F(r',n\pm1) \right|^2 e^{-4\gamma R} \tag{55}$$

There is no way of evaluating the sum on the right hand side at this time. We note that it contains as its terms the relative probabilities that the jump will occur via site n, rather than another site n'. If R is large enough, we should be able to approximate it by a constant Z, of order unity. With this approximation, equation (52) can be rewritten as:

$$W(r \rightarrow r') = \frac{2\pi J^2}{\hbar^2}\, Z\, e^{-2S(T)}\, e^{-4\gamma R} \sum_k \frac{\gamma_k}{N} \coth \frac{\beta\hbar\omega_k}{2}\, \delta\left(\frac{\Delta E}{\hbar} \pm \omega_k\right)$$

$$\tag{56}$$

When a field is applied, we must substitute Δ for ΔE in equation (56):

$$\Delta = V_r - V_{r'} - eF \qquad (57)$$

Equation (56) can be evaluated for Case I. Then from equations (33a) and (16a) we can write, considering coupling from only the nearest neighbor oxygen ions:

$$\gamma_k = \frac{C^2 \sin^2 k \sin^2 2k}{M\omega_o^2 \, \hbar\omega_o \sin^3 \frac{1}{2} k} \approx \frac{32 \, C^2 \, k}{M\omega_o^2 \, \hbar\omega_o} \approx \frac{64 \, C^2}{M\omega_o^2 \, \hbar\omega_o} \frac{\omega_k}{\omega_o} \qquad (58)$$

where use has been made that $\omega_k/\omega_o \ll 1$. Inserting equation (58) into equation (56), replacing the sum by an integral, and using relation (57);

$$W(r \to r') = \frac{2\pi J^2}{\hbar^2} Z \, e^{-2S(T)} \, e^{-4\gamma R} \, \frac{1}{\pi} \int_0^\pi \frac{2 \times 64 C^2}{M\omega_o^2 \, \hbar\omega_o}$$

$$\times \frac{\omega_k}{\omega_o} \coth \frac{\beta\hbar\omega_k}{2} \, \delta\!\left(\frac{\Delta}{\hbar} \pm \omega_k\right) \frac{d\omega_k}{\omega_o} \qquad (59)$$

and integrating leads to:

$$W(r \to r') = \frac{2J^2}{\hbar^2} Z \, e^{-2S(T)} \, e^{-4\gamma R} \, \frac{128 \, C^2 \, \Delta}{M\omega_o^3 (\hbar\omega_o)^2} \coth \frac{\beta\Delta}{2} \qquad (59a)$$

Equation (59a) is in the same form as that developed by Miller and Abrahams[14] for the case of impurity conduction at low concentration, with the addition of the term $e^{-2S(T)}$, and the absence of a term proportional to $R^{3/2}$. Our Z term could in fact have R dependence; however, it should vary slowly; the main variation will be via the exponential. Making use of typical values[5] $J = 10^{-3}$ eV, $e^{-2S(T)} = 10^{-2}$, $C^2/M\omega_o^2 \, \hbar\omega_o = 5$, $\omega_o = 10^{13}$, equation (59) reads:

$$W(r \rightarrow r') \approx 2 \times 10^{12} \Delta Z \, e^{-4\gamma R} \coth \frac{\beta \Delta}{2}$$

which is the same order of magnitude as that given by Pollack and Geballe[16] for Miller and Abraham's expression.[14]

We note that the Case II γ_k becomes infinite as $\omega_k \rightarrow 0$; in fact as can be seen by inspection of equations (13c) and (33b) a uniform translation of the solid will give rise to a large energy shift. We discard this case as meaningless.

High Temperature Approximation

We will require an expression for the transition rate at high temperatures in our discussion of the DC conductivity. The integral in equation (49) has been evaluated by Holstein[5] for $\Delta E = 0$. We shall follow his method here. First we introduce the transformation:

$$t = \frac{i\beta\hbar}{2} + \tau \tag{60}$$

which transforms the integrand of equation (49) to:

$$\exp\left(-\frac{\beta\Delta E}{2}\right) \exp\left[-\sum_k \frac{\gamma_k}{N}\left(\coth\frac{\beta\hbar\omega_k}{2} - \operatorname{csch}\frac{\beta\hbar\omega_k}{2}\cos\omega_k\tau\right)\right.$$

$$\left. + \frac{i\Delta E\tau}{\hbar}\right] \tag{61}$$

The τ-integration extends from $-t$ to $+t$ on the real axis, and two components perpendicular to this axis from $-t - \frac{i\beta\hbar}{2}$ to $-t$ and from t to $t - \frac{i\beta\hbar}{2}$. Combining the latter two under one integral we obtain:

$$W(r \rightarrow r') = \frac{J^2}{\hbar^2} Z \exp(-4\gamma R) \exp\left(-\frac{\beta\Delta E}{2}\right)(I_1 + I_2) \tag{62}$$

where:

$$I_1 = \int_{-t}^{t} \exp\left[- \sum_k \frac{\gamma_k}{N} \left(\coth \frac{\beta\hbar\omega_k}{2} - \operatorname{csch} \frac{\beta\hbar\omega_k}{2} \cos \omega_k\tau \right) \right.$$

$$\left. + \frac{i\Delta E\tau}{\hbar} \right] d\tau \tag{63}$$

$$I_2 = \sum_{\pm} \mp \int_0^{\beta h/2} \exp\left[- \sum_k \frac{\gamma_k}{N} \left(\coth \frac{\beta\hbar\omega_k}{2} - \operatorname{csch} \frac{\beta\hbar\omega_k}{2} \right.\right.$$

$$\left.\left. \times \cos \left[\omega_k(t \pm i\sigma)\right] \right) + \frac{i\Delta E}{\hbar}(t \pm i\sigma) \right] d\sigma \tag{64}$$

The second integral, equation (64), contributes little, following Holsteins's analysis (that is, the term inside the brackets still determines the convergence of the integral). Equation (63) diverges when $\Delta E = 0$, and needs to be corrected by removing those transitions for which $N = N'$. Equation (63) therefore becomes:

$$I_1^{(c)} = \exp[-2S(T)] \int_{-t}^{t} \left(\exp\left[\sum_k \frac{\gamma_k}{N} \operatorname{csch} \frac{\beta\hbar\omega_k}{2} \cos \omega_k\tau \right.\right.$$

$$\left.\left. + \frac{i\Delta E\tau}{\hbar} \right] - \exp\left[\frac{i\Delta E\tau}{\hbar}\right] \right) d\tau \tag{65}$$

We now wish to let $t \to \infty$. The first exponential of equation (65) will rapidly converge, while the second will cause the integrand to oscillate. Because of the rapid convergence, we can replace $\cos \omega_k\tau$ by $(1 - \omega_k^2\tau^2/2)$:

$$I_1^{(c)} = \exp[-2S(T)] \int_{-t}^{t} \left\{ \exp\left[\sum_k \frac{\gamma_k}{N} \operatorname{csch} \frac{\beta\hbar\omega_k}{2} \left(1 - \frac{\omega_k^2\tau^2}{2}\right) \right.\right.$$

$$\left.\left. + \frac{i\Delta E\tau}{\hbar} \right] - \exp\left(\frac{i\Delta E\tau}{\hbar}\right) \right\} d\tau \tag{66}$$

Rearranging terms, we find:

$$I_1^{(c)} = \exp\left[-2S(T)\right] \exp\left[\sum_k \frac{\gamma_k}{N} \operatorname{csch} \frac{\beta\hbar\omega_k}{2} - \frac{\Delta E^2}{4\hbar^2 W}\right]$$

$$\times \int_{-t}^{t} \left[\exp\left(-\sqrt{W}\tau - \frac{i\Delta E}{2\hbar\sqrt{W}}\right)^2 - \exp\left(\frac{i\Delta E\tau}{\hbar}\right)\right] d\tau \qquad (67)$$

where:

$$W = \sum_k \frac{\gamma_k}{2N} \omega_k^2 \operatorname{csch} \frac{\beta\hbar\omega_k}{2} \qquad (67a)$$

Evaluating the integral and letting $t \to \infty$:

$$I_1^{(c)} = \exp\left[-2S(T)\right] \exp\left[\sum_k \frac{\gamma_k}{N} \operatorname{csch} \frac{\beta\hbar\omega_k}{2} - \frac{\Delta E^2}{4\hbar^2 W}\right] \left(\frac{\pi}{W}\right)^{1/2} \qquad (68)$$

By use of equation (67a), and on changing the sums to integrals:

$$I_1^{(c)} = \exp\left[-2s(T)\right] \exp\left[\frac{1}{\pi} \int_0^\pi 2\gamma_k \operatorname{csch} \frac{\beta\hbar\omega_k}{2} \, dk\right]$$

$$\times \left\{\frac{\pi}{\frac{1}{\pi} \int \gamma_k \omega_k^2 \operatorname{csch} \frac{\beta\hbar\omega_k}{2} \, dk}\right\}^{1/2}$$

$$\times \exp\left[\frac{-\Delta E^2}{4\hbar^2 \frac{1}{\pi} \int \gamma_k \omega_k^2 \operatorname{csch} \frac{\beta\hbar\omega_k}{2} \, dk}\right] \qquad (69)$$

Combining the three exponentials, and noting that:

$$-\coth \frac{\beta\hbar\omega_k}{2} + \operatorname{csch} \frac{\beta\hbar\omega_k}{2} = -\tanh \frac{\beta\hbar\omega_k}{4} \qquad (70a)$$

and that if $\hbar\omega_k \ll kT$;

$$\tanh \frac{\beta\hbar\omega_k}{4} \approx \frac{\beta\hbar\omega_k}{4} \qquad (70b)$$

-37-

$$\operatorname{csch} \frac{\beta \hbar \omega_k}{2} \approx \frac{2}{\beta \hbar \omega_k} \tag{70c}$$

Equation (69) may be rewritten as:

$$I_1^{(c)} = \left(\frac{\pi \hbar^2}{4 E_a kT}\right)^{1/2} \exp\left[-\frac{E_a + \frac{\Delta E^2}{16 E_a}}{kT}\right] \tag{71a}$$

where:

$$E_a = \frac{1}{\pi} \int_0^\pi \frac{\gamma_k \hbar \omega_k}{2} dk \tag{71b}$$

Combining equation (71) with equation (62):

$$W(r \rightarrow r') = \frac{J^2}{\hbar} Z \exp(-4\gamma R) \exp\left[-\frac{E_a + \frac{\Delta E}{2} + \frac{\Delta E^2}{16 E_a}}{kT}\right]$$

$$\times \left[\frac{\pi}{4 E_a kT}\right]^{1/2} \tag{72}$$

In the crystalline case, $Z = 1$, $\gamma = 0$, $\Delta E = 0$, and equation (72) becomes identical to that given by Holstein[5] (his equation contains an error; the $\hbar$ is to the first and not the second power). Furthermore, if ΔE is small in comparison to E_a, the ΔE^2 term in equation (72) may be neglected.

3. DISCUSSION

Review of Theoretical Model

Before proceeding to apply the results of Chapter II to exper-
mental conductivity data, it is worthwhile to review the calculations
of that chapter, with specific emphasis on the assumptions which have
been made, and their implications.

Our starting equation (10) is very similar to that for the
crystalline lattice.[5] The essential difference arises from the energy
of the electron in each of the complexes being different due to the
disorder of the lattice. We then approximated the ionic masses to
be equal, and that all nearest neighbor force constants were equal.
Due to the anharmonic nature of the interatomic bonds, this approxi-
mation is not strictly true. Inclusion of these effects will result
in some localization of the vibrational wavefunctions, and hence to
a nonanalytic problem. Mathematically, localization is equivalent
to the normal vibration coordinates [equation (15)] no longer being
normal. If the anharmoniticity is not too great, the strictly
harmonic approximation that we have used should give reasonable
agreement with reality. In addition, because we have taken the ionic
masses to be equal, the phonon modes in the range $0 \le k \le \frac{\pi}{2}$ will be
accoustical modes, while those in the range $\frac{\pi}{2} \le k \le \pi$ will be
optical modes.

An analytic solution to the strictly harmonic one-dimensional

problem is possible since the solution of the vibrational modes will

be a plane wave expansion. In three-dimensions, the eigenstates of

the lattice vibrations are no longer plane waves due to the disorder.

It is for this reason that the three-dimensional problem has not been

solved analytically.[10]

We next assumed that the energy of the electron was linearly

related to the lattice displacements. It is at this point that we

can distinguish between a polaron and a small polaron treatment. In

the polaron problem, the main electron-lattice interaction would come

from more distant neighbors - that is, the electron would be moving

sufficiently fast so that the lattice in the vicinity of the electron

would not have time to react to the electron's field. In the small

polaron case, the electron velocity will be such that the lattice

in the vicinity of the electron will react, and hence the nearest

neighbor interaction will be important. The inclusion of distant

interactions enables us to treat the polaron case in our problem.

We shall come back to this point later on in this section.

The assumption that the overlap integrals J_{mn} are independent

of the lattice displacements [equation (13d)] removes the effect of

thermally assisted tunneling. Thermally assisted tunneling results

from the increased overlap of the electronic wave functions due to

lattice vibrations which cause adjacent metal ions to move closer

to each other. Provided that the wave functions do not vary appreciably

across nearest neighbor complexes, this approximation should be good.

Next, to solve the wave equation (we are treating the coef-

ficients, a_n, as wave functions), we took as a first approximation

$J_{mn} = 0$. In completing the square in equation (18) (which is the same thing as using a variational principale o determine the ground state) and transforming to displaced normal coordinates, we allowed the electron to interact with the lattice and distort it. The effect of the non-zero value for the J_{mn} was treated as perturbation. The J_{mn}'s gave rise to the matrix elements $(pN|V|p'N')$ which allow the polaron to move from site to site.

It is at this point that we have narrowed our attention to the small polaron case. In our solution, we have assumed that C^1 is important, as it will be for the small polaron. However, by setting the $C^\ell = 0$ for a certain number of inner neighbors, we can deal with the polaron case. Unfortunately, we have no criteria to indicate how far out to set the $C^\ell = 0$; this will vary depending on the material considered, and, as noted in Chapter I, on the amount of disorder present. In order to establish such a criteria, we would need to solve the wave equation [equation (18)] in the zeroeth order for both J and the electron-lattice interaction. Such a solution appears to be possible using Anderson's Green's function method;[11] however, since the solution would require numerical methods, it shall not be considered here.

In order to solve the problem, we assumed that the interaction parameters B_n, C_n^ℓ were equal for all values of n. In doing so, we have assumed that the lattice deformation on different sites, and consequently the deformation or binding erergy is the same for all sites for a given set of phonon occupation numbers. The result of nonequal binding energies will be to further increase the energy differences between sites.

The solution to the crystalline problem reaveals a polaron bandwidth of 2J exp [-2S(T)], that is, one which decreases exponentially with temperature. In the disordered lattice, we apply Anderson's theorem and find that the criterion for localized states is that the parameter ($<A>/J$) exp [S(t)] must be sufficiently large. Here we notice that the criterion is temperature dependent, and that the probability of localized states increases with increasing temperature. Furthermore, the presence of the exponential term, which is always greater than unity for both the polaron and small polaron cases, means that localized states are more probable in the polaron problem than in the pure electron problem, and that the probability for localized states, for a given amount of disorder, increases exponentially as the electron-lattice interaction increases. In addition, there is a possibility that when disorder is small, there will be band states at low temperature, but that these states will become localized as the temperature increases.

To solve the problem for the disordered lattice, we invoked Mott's conjecture[1] that the wave functions decay exponentially as exp ($- \gamma_r |S_n - S_r|$). In other words, the polaron in a state localized at r is not confined to a single metal ion; there is a probability of finding it on nearby ions also. With our eigenstates thus established, we determined the transition rate from a state localized on site r to one localized at r'. Such a transition cannot be vertical; that is, the polaron cannot emit or absorb a phonon on one site. Instead the transition is diagonal; that is, the polaron simultaneously jumps from one site to another with the absorption or emission of phonons.

Because of the overlap of the eigenfunctions, it is possible for the polaron to travel a large distance in a single hop. The transition will therefore take place via a tunnel-hop-tunnel mechanism. The importance of these transitions follows from the fact that nearest neighbor energy states may be too different for the transition to occur easily; but a transition between more distance neighbors, where the energy difference may be more favorable, can occur.

We should emphasize one fact about multiphonon processes. These transitions must take place in a single hop, or via multiple hops in which each intermediate state is an allowed state. The probability of a multiple hop will be equal to the product of the probabilities for each single hop.

We shall conclude this section by noting that the γ appearing in the exponent of the expression for the transition rate [equations (59a) and (72)] is not a constant, but is different for each pair of states. This statement follows from Anderson's Green's function method,[11] which will be treated in the next section. This "disorder" parameter, γ, will tend to zero as the lattice becomes ordered; hence, for localized states in regions of small disorder, it will be small; while in regions of extensive disorder, it will be large.

AC Conductivity

The AC conductivity of a disordered solid will be a bulk effect. The applied AC field will cause the energy levels of the complexes to fluctuate, and the polaron may therefore hop from one site to another. Since the field is varying, an electron does not have to travel through the lattice as is the case for DC conduction, but need merely change

-43-

sites in order to contribute to an AC current. The result is that localized states which do not contribute to the DC conduction are brought into play, causing an increase in the observed conductivity. As the frequency increases, more hops occur in a given period of time (provided that the transition time is short enough), and the net current increases.

Pollack and Geballe[16] have derived an expression for the difference between the AC and DC conductivity (σ_{AC}), which is assumed to take place via hopping between pairs of sites with an energy difference ΔE. Their expression is applicable in the present situation, by taking the total number of pairs to be $N(1-c)$, where N is the total number of metal ions, and c is the concentration of electrons ($= Me^{(n)+}/Me^{(n+1)+}$), and inserting a term $f'(\gamma) \, d\gamma$ and integrating with respect to γ to account for the variation in the disorder parameter γ:

$$\text{Re} \, [d\sigma_{AC}(r,\Delta E,\omega)] = \frac{1}{12} \, dp(r,\Delta E) \, N(1-c) \, \frac{e^2}{kT} \, r^2$$

$$\times \int \tau^{-1} \, \frac{\omega^2 \tau^2}{1 + \omega^2 \tau^2} \, \frac{f'(\gamma) \, d\gamma}{\cosh^2 \left(\frac{\Delta E}{2kT} \right)} \tag{73}$$

The term $dp(r,\Delta E)$ is the number of sites of energy difference ΔE at a distance r, which we shall define as:

$$dp(r,\Delta E) = 4\pi r^2 \, (Nc)P(r) \, f(\Delta E) \, dr \, d(\Delta E) \tag{74}$$

where $P(r)$ is the pair distribution function of metal ions, and $f(\Delta E)$ is the probability of a localized state with energy difference ΔE. This latter function intuitively should be a function close to a Gaussian

distribution function. Inserting equation (74) into equation (73) and integrating over r and ΔE, we find:

$$Re(\sigma_{AC}) = \frac{1}{12} N^2 c(1-c) \frac{e^2}{kT} \iiint 4\pi r^4 \tau^{-1} \frac{\omega^2 \tau^2}{1 + \omega^2 \tau^2}$$

$$\times \frac{P(r) \; f(\Delta E) \; f'(\gamma)}{\cosh^2 \left(\frac{\Delta E}{2kT}\right)} \; dr \; d(\Delta E) \; d\gamma \qquad (75)$$

where τ is obtained from equation (59a):

$$\tau = \frac{1}{W(r \rightarrow r')} = \frac{\hbar^2 \; M\omega_o^3 \; (\hbar\omega_o)^2}{256 \; J^2 \; Z \; c^2} \exp \, [2s(T)] \; \exp \, 4\gamma R$$

$$\times \tanh\left(\frac{\Delta}{2kT}\right) \qquad (76)$$

[The term Δ is taken into account in deriving equation (73).]

Equation (75) is nonanalytic and has not been evaluated even for the case when $P(r)$, and the terms in γ and ΔE can be omitted. We can discuss the qualitative results, however.

The first thing we note is that if

$$\tau \ll \frac{1}{\omega}$$

in all cases, then the AC conductivity is proportional to ω^2. However, τ is a function of r, ΔE, and γ. Pollack and Geballe considered the case when we can ignore the effect of γ (i.e., take it equal to a constant) and $P(r)$ [i.e., we are in the range where $P(r)$ is equal to 1]. They find that the AC conductivity is approximately proportional to ω^n where n is some constant less than 2. This behavior arises from the circumstance that as ω increases, more hops are made causing an increase in conductivity, but the longer transition times cease

-45-

to contribute to a conductivity increase (i.e., $\frac{\omega^2 \tau^2}{1 + \omega^2 \tau^2} \approx 1$ for these long transition times).

The case when all factors must be taken into consideration is much more complex, and therefore is best discussed by considering experimental data. We consider the data obtained by Hench and Clark,[17] and Hench and Kinser[18] for a potassium vanadium phosphate glass. They observed that at low temperatures, the AC conductivity increased proportional to $\omega^{0.8}$ at low frequencies, but that the exponent n gradually increased to a value of 2 at a frequency of 10^7 Hz. The variation in the exponent of ω^n with a change in the frequency can be attributed to either the pair distribution function $P(r)$, or to the γ distribution function $f'(\gamma)$. The pair distribution function can be calculated from x-ray diffraction data, and is generally found to differ from unity only for the first, second and third nearest neighbor metal ions. The distance between these pairs of ions is a maximum of approximately 10 $\overset{o}{A}$, and therefore the induced energy shift caused by the field is of the order of 10^{-5} electron volts. This value is much less than kT, and hence these transitions between second and third nearest neighbors can be accomplished by the phonons themselves, and should contribute little to the AC conductivity.

We are led to the conclusion that the variation in the exponent of ω must be due to the disorder parameter, γ. To understand how this can be, we must consider a qualitative solution to the wave equation [equation (26)]. According to Anderson[11]

$$a_{jk}(E) = \lim_{\sigma \to 0} i \, \sigma(j|W|k) \qquad (77)$$

where

$$(j|W|k) = \frac{\delta_{jk}}{i\sigma + E - E_j} + \sum_{\ell} \frac{1}{i\sigma + E - E_j} V_{j\ell} (\ell|W|k). \tag{78}$$

The $V_{j\ell}$ in our case is just the matrix element $(jN|V|eN)$. The energy E is the energy of the eigenstate V_j, and the energy E_j is the energy of the polaron on the complex j (including the perturbation energy). The coefficient $a_{jk}(E)$ is the wave function at site k for a polaron localized on site j. Equation (77) is solved by an iteration technique. From inspection it is seen that the solution for k distant from j will involve the product of matrix elements in the numerator, and a product of energy differences in the denominator. If now there are highly ordered regions in the lattice where the energy levels are nearly the same, then the wave function will not decrease rapidly. It will decrease rapidly in those areas where disorder is high. Thus if we may postulate the structure of the glass as being composed of partially ordered regions separated by regions of large disorder, the transition times will not vary continuously with r, but will come in "clumps," changing sizeably as the disordered regions are crossed. A similar behavior occurs if instead of ordered and disordered regions we postulate disordered regions of one phase (metal oxide rich) surrounded by disordered regions of a second phase (metal oxide deficient).* Then in the metal oxide deficient region, due to the decreased overlap, and the presence of other species presenting a wrong energy level

---

*An alternative model would consist of two interconnected phases, each having a slightly different metal oxide content, such that the easiest path takes the polaron across the different phases, rather than restricting it to one phase.

to the electron, the wave function will decrease sharply; while in the cells of the disordered metal oxide rich region, the wave function will decrease only gradually. The exponent variation would thus arise essentially from the distribution of metal oxide rich or ordered region cell sizes.

In order to be compatable with x-ray data, the size of the ordered regions can be no larger than ~15 $\overset{o}{A}$; otherwise crystalline diffraction lines will appear. There are no restrictions on the size of the phase separated regions however, for if the metal deficient phase assumes a very small total volume of the glass (being only one or two oxide complexes thick about the metal oxide deficient phase), then low angle x-ray scattering will not detect the phase separation.

The phase separation explanation appears to be more desirable since it allows the polaron to travel large distances, over which the effect of the applied field will be appreciable. It should be noted that Pollack and Geballe[16] found that in impurity conduction in silicon at low concentrations the distance traveled in a single hop was the order of 100-300 $\overset{o}{A}$. However, in the absence of specific calculations which our present model does not allow, it is questionable as to which effect is the cause of the change in the exponential of ω.

In any event, the electron transport mechanism at low frequency would be similar to that considered by Pollack and Geballe, but as the frequency increases, we approach a range where all τ are either $>> \frac{1}{\omega}$ or $<< \frac{1}{\omega}$. The former contribute as ω^2 as previously shown, the latter do not contribute to the frequency dependent conductivity.

The temperature dependence of the AC conductivity is an extremely complex situation. In the first place, we note that the

transition time is strongly dependent on temperature through the term $e^{2S(T)} \tanh\left(\frac{\Delta E}{2kT}\right)$. The conductivity expression also contains a term $\frac{1}{T} \frac{1}{\cosh^2\left(\frac{\Delta E}{2kT}\right)}$. Furthermore there are multiple phonon process which

enter in as T increases; these terms become increasingly important as the electron-lattice coupling increases. Finally, the γ in the exponential will be temperature dependent, increasing as temperature increases. This last point can be seen by considering Anderson's Green's function method. The amplitude on site j for a wave function localized on site k will be given by equation (77). Each of the matrix elements $(pN|V|p'N)$ contains the term exp $[-S(T)]$. Therefore, the sum over ℓ, which gives the wave function at site j contains the term exp $[-s(T)]$. Furthermore, because of $(\ell|W|h)$, the wave function must decrease approximately as $e^{-n\,S(T)}$ for the nth site from the site j. Hence, the wave function will become more localized as the temperature increases. This is the localized state analogue of the decrease in mean free path with increasing temperature for the crystal-line problem, and is the reason for the appearance of the term exp $[S(T)]$ in the criterion for localized states.

Before proceeding, it will be of interest to examine the term exp $[-s(T)]$. At absolute zero, this term will assume a value $e^{-S(0)}$. As the temperature increases, this term will decrease slowly, since the coth $\frac{\beta\hbar\omega_k}{2}$ will be large only for a few modes. At some temperature (of the order of $\frac{1}{2}\theta_{Debye}$), a large number of modes will be activated, and the exponent will decrease more rapidly. The larger the electron-lattice coupling, the more rapid will be decrease. The qualitative behavior of exp $[-S(T)]$ is plotted in Figure 4.
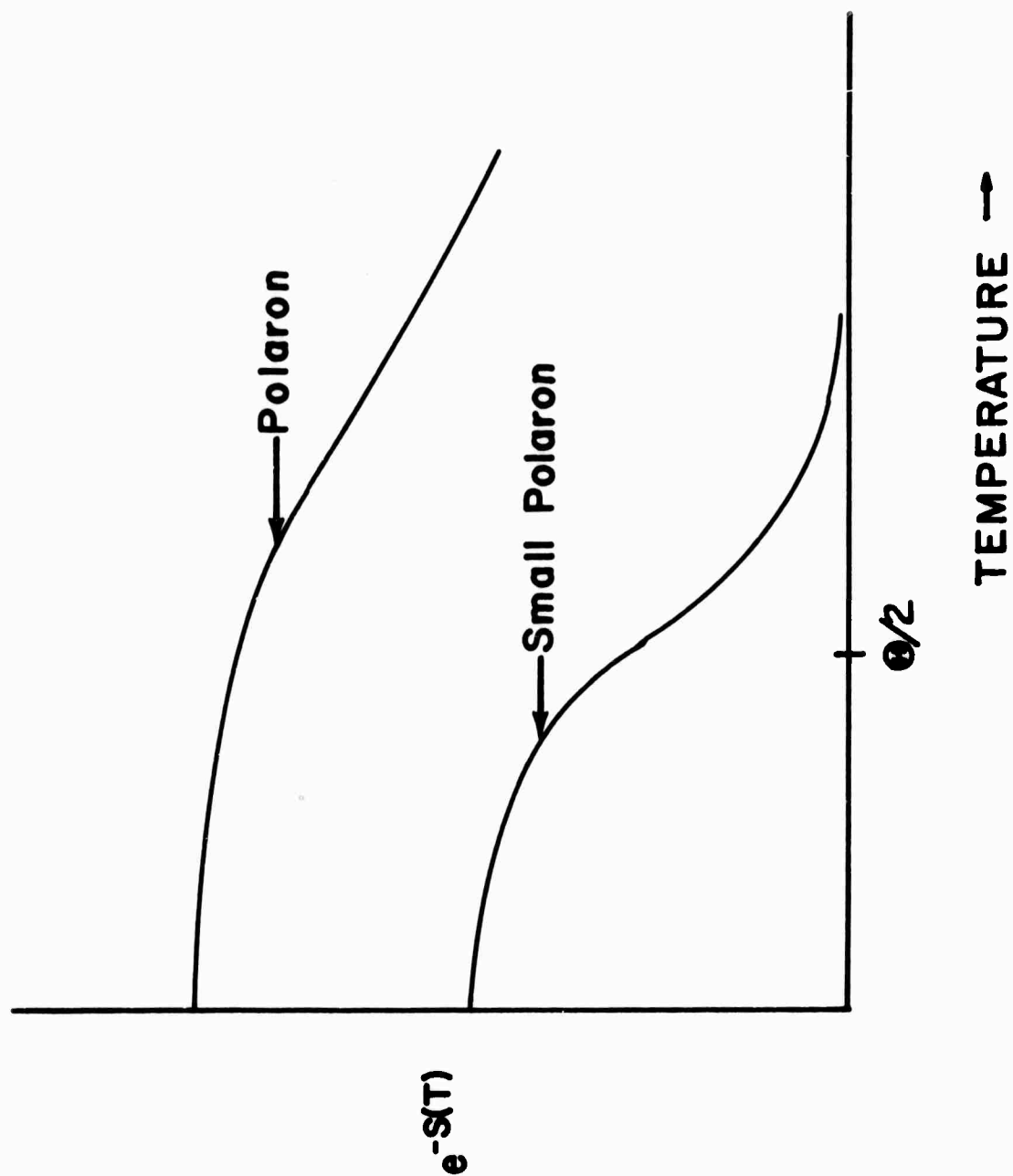
Figure 4. Qualitative plot of exp [-S(T)].

The AC conductivity is given by equation (75)

$$Re(\sigma_{AC}) = \frac{1}{12} N^2 c(1-c) \frac{e^2}{kT} \iiint 4\pi r^4 \tau^{-1} \frac{\omega^2 \tau^2}{1 + \omega^2 \tau^2}$$

$$\times \frac{P(r) \; f(\Delta E) \; f'(\gamma)}{\cosh^2 \left(\frac{\Delta E}{2kT}\right)} \; dr \; d(\Delta E) \; d\gamma$$

where:

$$\tau = \frac{\hbar^2 \; M\omega_o^3 \; (\hbar\omega_o)^2}{256 \; J^2 \; Z \; c^2} \; \exp \; [2S(T)] \; \exp \; 4\gamma R \; \tanh\left(\frac{\Delta}{2kT}\right)$$

We shall consider the effect first on the transition time τ. At sufficiently low temperatures, $kT \ll$ all ΔE. Under these circumstances $\tanh\left(\frac{\Delta E}{2kT}\right) \approx 1$. $\exp [2S(T)] \approx$ constant, and γ is not highly dependent on temperature (provided that the electron lattice interaction is not too strong). We conclude then, that at low temperatures, the transition time, τ, is practically independent of temperature.

As the temperature increases, for those transitions for which $kT \gg \Delta E$, $\tanh\left(\frac{\Delta E}{2kT}\right) \to 0$. At the same time $\exp [2S(T)]$ will increase. Thus some transition times become longer, while others become shorter (ΔE and R small). At sufficiently high temperatures, $\tanh\left(\frac{\Delta E}{2kT}\right) \exp [2S(T)] \to \infty$ for all transitions; thus all transition times increase. The increase is even more pronounced due to the temperature caused increase of γ. Also, as the temperature is increased multiphonon transitions will come into play, providing short transition times again.

As previously stated, the low temperature AC conductivity supports the view that the density of transition times come in clumps (Figure 5). As the temperature increases therefore, the frequency at which the exponent of ω becomes equal to 2 should decrease.
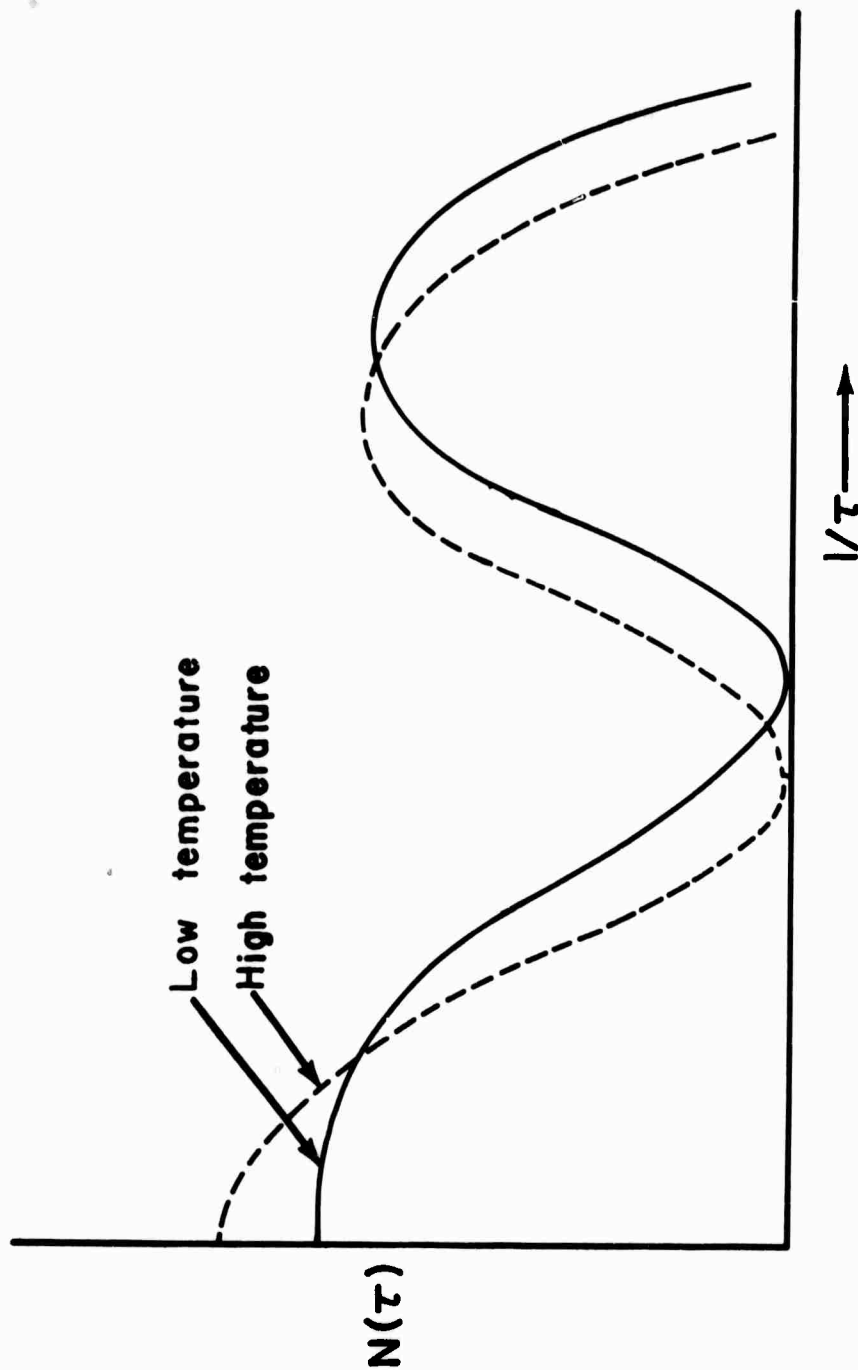
Figure 5. Plot of density of transition times.

Furthermore, at frequencies above 10^7 Hz, the exponent should also
decrease; the frequency at which the decrease in the exponent is observed
should also decrease with temperature.

Looking now at the term $\dfrac{1}{kT \cosh^2\left(\frac{\Delta E}{2kT}\right)}$, at low temperatures,
$kT \ll$ all ΔE, $\cosh^2\left(\frac{\Delta E}{2kT}\right) \to \infty$, such that $kT \cosh^2\left(\frac{\Delta E}{2kT}\right) \to \infty$. That is,
the AC conductivity should decrease with decreasing temperature at
very low temperatures. For $kT > \Delta E$, $kt \cosh^2\left(\frac{\Delta E}{2kT}\right) \to kT$. That is,
at sufficiently high temperatures, the AC conductivity should decrease
as $1/T$. At temperatures in between these two extremes, only those
transitions for which $\Delta E < kT$ will contribute appreciably to the
conductivity. As the temperature increases, more such states will
be brought into play, but offsetting this increase in total conductivity
will be the factor $1/T$. This paragraph is depicted graphically in
Figure 6.

It should be noted that in this discussion we have assumed
that none of these transitions will contribute to the DC conductivity.
As the temperature increases, many of the transition with small ΔE
will contribute to the DC conductivity; these must be subtracted from
consideration in our AC conductivity.

DC Conductivity

The low temperature conductivity will be determined essentially
by the most difficult step of the easiest path through the glass.[14]
Thus, most of the steps through the glass are between localized levels
of nearly the same energy. It is probable, however, that the most
difficult step will be of sufficiently high energy that the transition
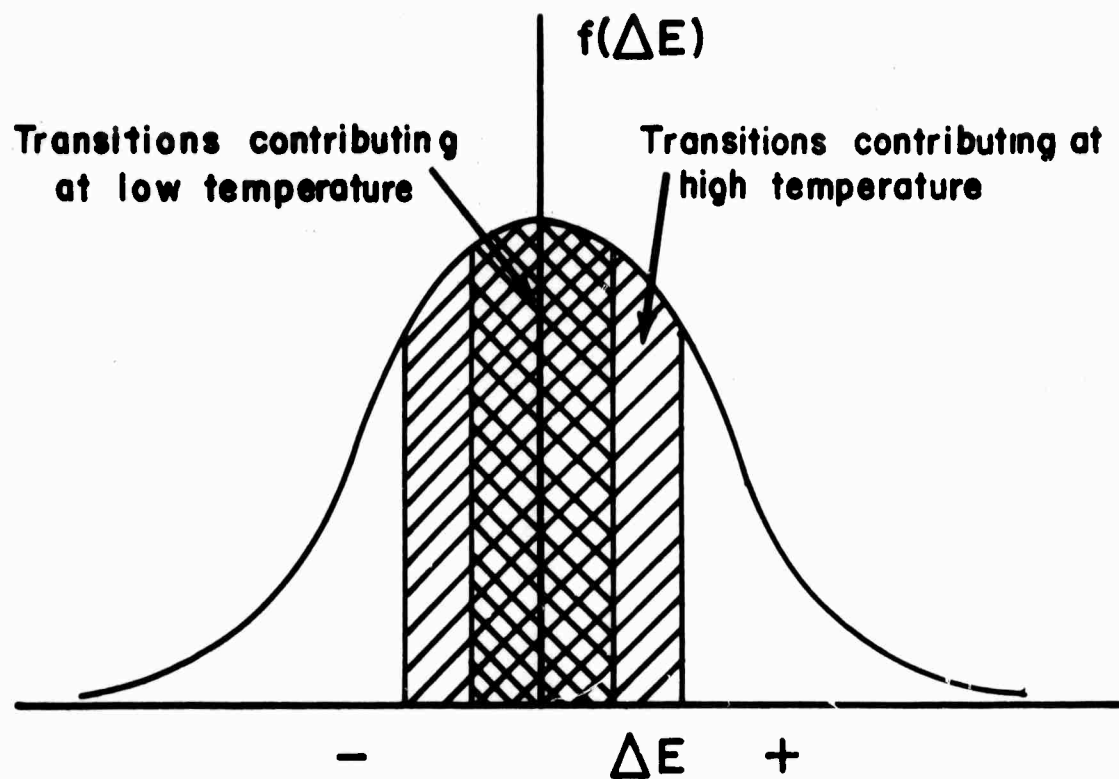
Figure 6. Transition contribution as a function of temperature.

will be via a multiphonon hop. Therefore we shall resort to using the high temperature approximation which takes into consideration these multiphonon hops. A detailed calculation of the conductivity must be based on averaging procedures similar to those of Miller and Abrahams.[14] In lieu of the uncertainty of the exact nature of the localized states at the present time, as was discussed in the preceeding section, we shall not go into such a derivation here. Instead, we shall consider only the most difficult step, which should largely determine the conductivity. The conductivity contribution of this step will be from equation (72):

$$\sigma = n e \mu = \frac{ne^2R^2}{kT} W(r \rightarrow r')$$

$$\sigma = \frac{ne^2R^2J^2Z\pi^{1/2}}{2E_a^{1/2}(kT)^{3/2}\hbar} \exp(-4\gamma R) \exp\left[-\frac{E_a + \frac{\Delta E}{2} + \frac{\Delta E^2}{16E_a}}{kT}\right] \quad (79)$$

Over a narrow temperature range, at sufficiently low temperatures where we can ignore the temperature effect on γ, the activation energy will be given by:

$$Q = E_a + \frac{\Delta E}{2} + \frac{\Delta E^2}{16E_a} \quad (80)$$

where ΔE represents the energy difference of the most difficult step.

As the temperature increases, ΔE will decrease, as has been noted by Miller and Abrahams,[14] and Mott.[1] The decrease is a result of the activation of paths other than the easiest. However, partially offsetting the decrease will be an increase caused by the temperature dependence of γ. This effect will be more pronounced the larger the electron-lattice interaction.

Effect of Heat Treatment

Experimentally, the effect of heat treatment on a glass has been shown to be (1) the nucleation and growth of crystallites in the glassy matrix, and/or (2) the separation of the glass into two or more phases of differing composition.[19]

We shall consider the effect of nucleation and growth first, which is an ordering of the glassy matrix. This ordering must lead to a reduction in the deviation of the distribution of the energy levels, $f(\Delta E)$. The decrease in disorder must lead to an increase in the magnitude of the low temperature DC conduction due to the increased overlap between more distant localized states, and a decreased transition time. The activation energy may also change to reflect the dielectric properties of the ordered or partially ordered lattice, and the decreased ΔE term. As the disorder continues to decrease, the criteria for localized states will not longer be met at low temperatures and the polaron motion will take place largely by band diffusion through large regions of the glass. Further reduction in the disorder will result in the introduction of more paths through which band diffusion is possible and an increase in the bandwidth. At the same time the number of localized states would be reduced.

The effect of nucleation on the AC conductivity will be highly dependent on the starting glassy model and on the exact way in which nucleation takes place. Concrete experimental evidence is lacking on either of these factors. Furthermore, there will be a marked dependency on the exact nature of the localized wave functions, a factor which our model in its present development has not determined. These three factors determine the overlap of the wave functions as

a function of heat treatment. As the localized levels disappear, however, the AC effect will disappear.

Some comment is in order on the two models postulated in the AC conductivity section; that is, the order-disorder cell model, and the two-phase cell model. In the order-disorder model, the partial ordering of the regions which are highly disordered will lead to a decrease in the reduction of the wave function amplitude as it traverses the disordered region (Figure 7). On the average, the effect on the wave function is equivalent to a decrease in the disorder parameter γ. Alternatively, in the two-phase cellular model (or in a model where the phase interconnect as discussed in the AC conductivity section), order in the metal oxide deficient phase will have the same effect as in the order-disorder model.

A phase separation from a homogeneous phase into a metal oxide rich and a metal oxide deficient region will also lead to an increase in the DC conductivity due to an increased overlap of the electronic wave functions. A continuous phase will be formed provided that* (1) the separation occurs by spinodal decomposition or (2) separation occurs by nucleation and growth, and that the metal oxide rich phase assumes approximately 40 percent or more of the total volume of glass. In the latter case, the continuous phase (as well as the second phase) is nucleated as spherical particles in the glassy matrix. These spherical particles grow, eventually intersecting to form a continuous phase. In spinodal decomposition, compositional fluctuations arise. As the heat treatment progresses, the compositional gradient across the phase boundary sharpens, until complete separation has occurred.

---

*A review of phase separation in a glass is given by Hench.[19]
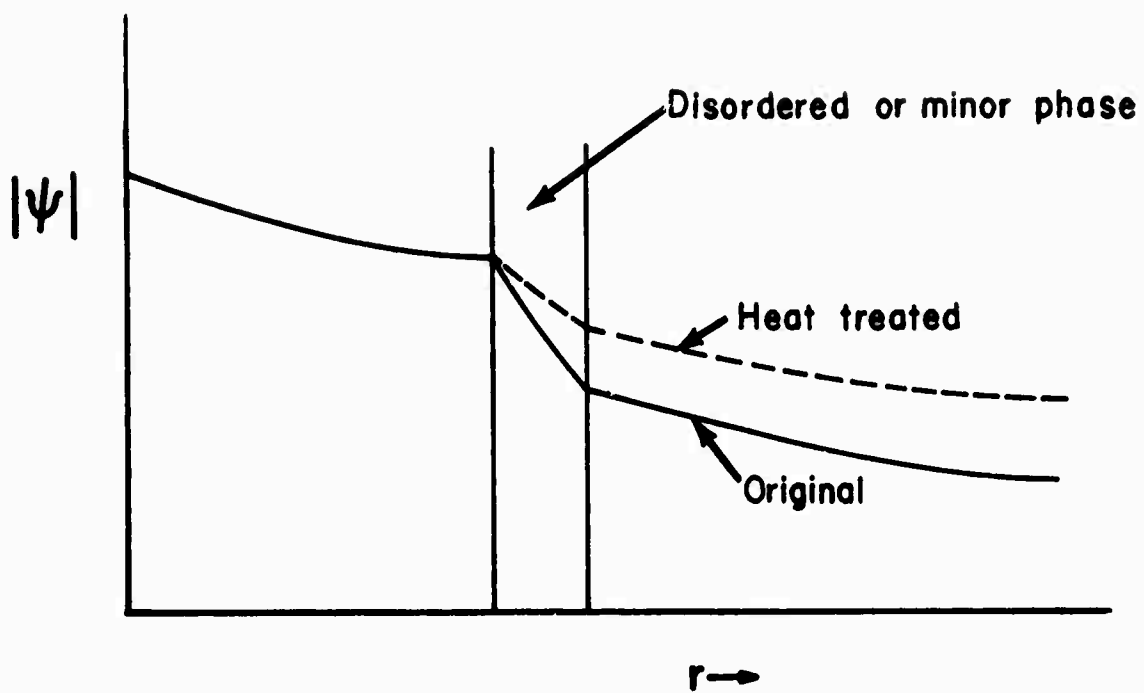
Figure 7. Envelope of wave function as a function of heat treatment.

It is probable that the new phases will be more ordered than the parent phase. The reasons for this are: (1) The parent phase reflects the temperature from which the glass is cast and the quenching rate (as well as composition), while the disorder of the separated phases will strongly reflect the annealing temperature (as well as the composition of the phases), which is lower than the casting temperature. (2) The "driving force" for the phase separation is a reduction in the free energy caused by satisfying the preferred coordination numbers of the species participating.

The result of such a phase separation will be an increase in DC conductivity. The region of rapidly increasing conductivity will be the region where nulceation and growth is taking place, or where the spinodal structure is coarsening. The activation energy will change (either increase or decrease) to reflect the dielectric properties of the high metal oxide phases, and the new disorder parameter and energy differences.

The effect of phase separation on the AC conductivity again will be dependent on the model treated. If the compositional gradient across the phase boundary is sharp enough, then conduction in the high metal oxide phase may be via band diffusion, which the metal oxide deficient phase will act as an insulator. Thus after sufficient heat treatment, all conduction would be essentially confined to the metal oxide rich phase, via band diffusion, and the AC conductivity would disappear.

The above discussion was based on the assumption that the initial composition was homogeneous, and is therefore applicable only to the order-disorder cell model. Turning our attention now to the

two-phase cellular model and the alternative interconnected phase model, we must take into consideration the fact that phase separation has already begun. Thus the two-phase cellular model would have to stem from a rather complicated peretectoid or eutectic reaction. We shall therefore not consider it further. If, however, decomposition has already begun spinodally, then the coarsening of the phase composition can lead to the formation of band states in the metal oxide rich phase and a loss in the AC conductivity.

Turning now to the experimental data (Figure 8), we see that the DC conductivity rapidly increases with heat treatment. The leveling off of the DC conductivity after a short time indicates that (1) a path of continuous high metal oxide content has been formed or (2) that a path(s) has been established which permits conduction essentially by band diffusion.

The AC conductivity during the early stages of heat treatment supports either of these views. The increase in the magnitude of the AC conductivity indicates that more localized states can contribute to the conduction. This can be a result of either an expansion in the spatial extent of the localized wave functions, allowing hops to be made between more distant localized states for which the field will cause a greater variation in energy, and/or a decrease in the energy levels. The loss of the AC effect with sufficiently long heat treatment indicates that the localized levels have spread out to such an extent that they may be considered as band states. Any of the models discussed so far supports these observations.

Additional insight into the distribution of transition times is gained in considering the effect of temperature on the AC conductivity

-60-
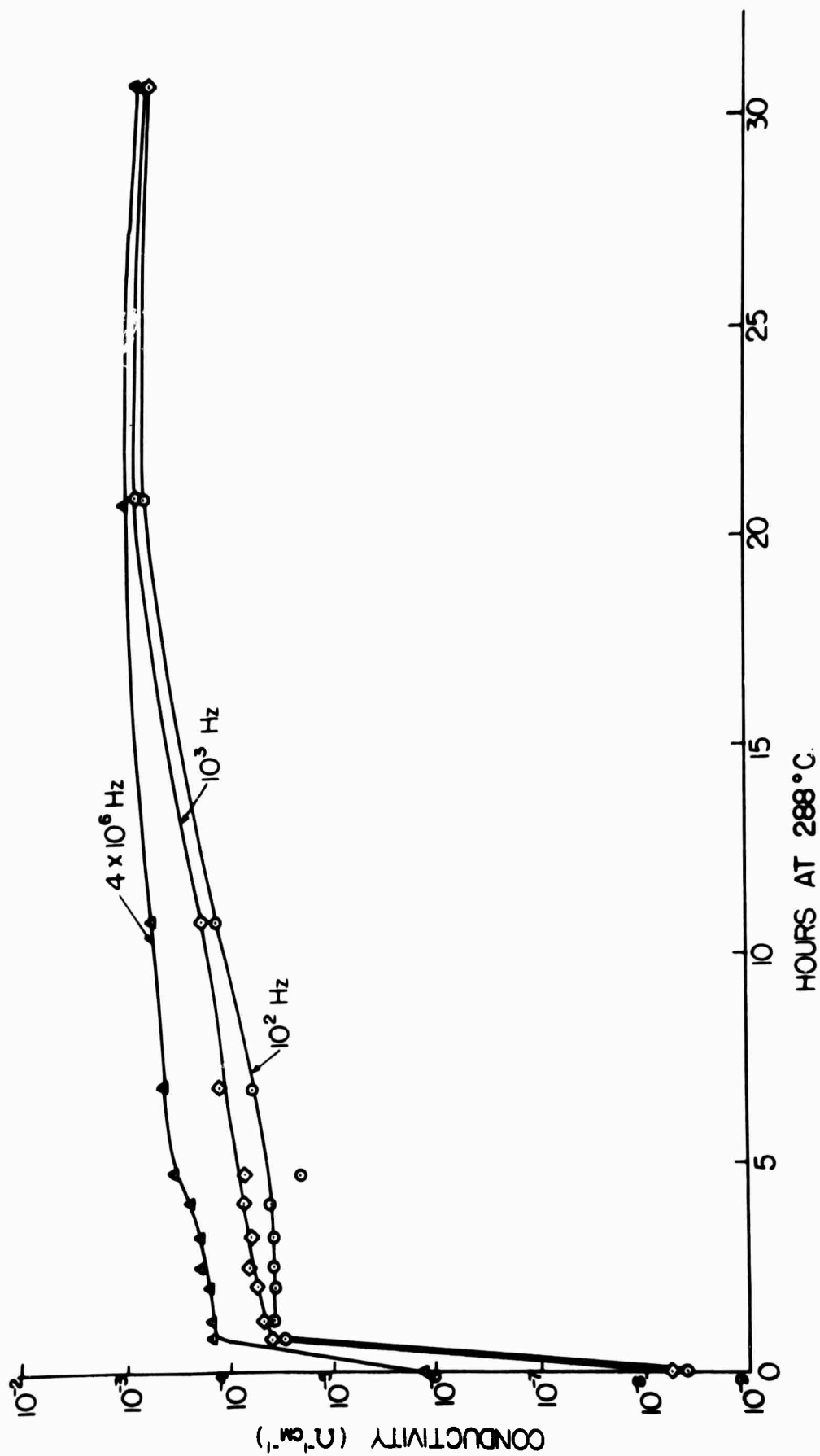
Figure 8. Conductivity behavior with thermal treatment.

of a glass heat treated for a short time. The AC effect is found
to be present at low temperatures, but decreases in magnitude as the
temperature increases (Figure 9). At a temperature of 56°C, the AC
conductivity becomes less than the DC conductivity. Since AC conduction
is via the bulk of the glass, the only way in which the AC conductivity
can be less than the DC conductvitiy is if the DC conductivity at
temperatures above the inversion temperature is also a bulk effect,
and not confined to a limited number of paths.

The depression in conductivity will arise from the presence
in the DC conduction expression of transition times $\tau < \frac{1}{\omega}$. That is,
both in AC and DC conduction, hops are made mainly by thermal acti-
vation, but as the frequency of the applied field increases, the long
transition times will not contribute to the conductivity. This is
a different phenomenon from the low temperature AC enhancement effect;
in that case, the localized states which caused an increase in the
conductivity with frequency did not contribute appreciably to the
DC conductivity. Instead, they were activated by a variation in the
energy levels caused by the applied AC field. Both effects may be
present; we require only that the suppression effect outweigh the
enhancement effect at high temperatures.

Referring to equation (76), we see that long transition times
will arise from (1) the effect of the exponential term exp [2S(T)]
which increases with temperature; (2) the exponential term exp (+4γR),
since γ increases with temperature; and (3) the term (tanh $\frac{\Delta E}{2kT}$) which
increases with increasing ΔE.

When a DC field is applied, the metal oxide complexes assume
a fixed set of energies. Assuming bulk conduction, hops between all
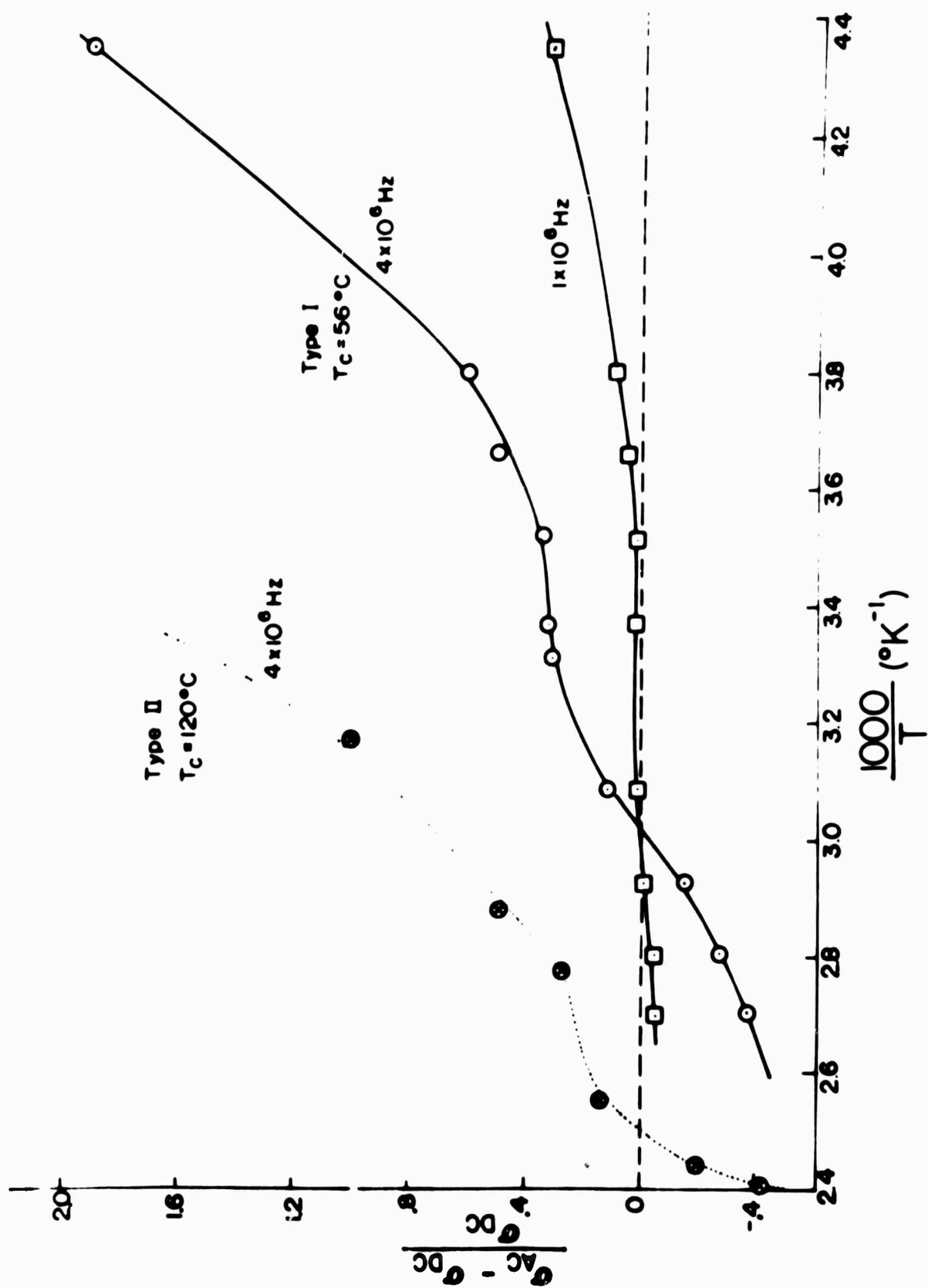
Figure 9. AC conductivity behavior of a partially annealed glass.

states will contribute to the total conductivity. We will also assume
that band diffusion contributes little at the high temperatures. When
an AC field is applied, the transitions for which $\tau < \frac{1}{\omega}$ will contribute
little (i.e., proportional to $\frac{1}{1 + \omega^2 \tau^2}$). The AC enhancement effect
may still be present; we require only that the suppression effect
outweighs the enhancement effect. The long transition times arise
primarily from distant states with large energy difference.

As the heat treatment continues, the localized states become
less and less localized until band diffusion appears. This will mean
that the temperature at which the inversion in the AC conductivity
takes place will increase, primarily since γ decreases. Similarly
at early stages during the heat treatment, the enhancement effect
outweighs the depression effect at all but the highest temperatures,
when all states participate in the hopping. Once again we see that
either the order-disorder cellular or the two-phase models are qual-
itatively correct in dealing with the depression phenonemon.

Conclusions

1. The localized polaron in the Nearly Crystalline Ionic Lattice
    model is found to qualitatively describe the observed conduction
    properties of a potassium vanadium phosphate glass.

2. The conduction phenomenon of a glass is found to be highly
    structure dependent, and with further numerical development
    should yield useful quantitative information on the disorder
    and phase separation in the glass.

3. Mott's proposal[1] that the localized wave functions vary as $\exp(-\gamma|x_n-x|)$ is found to be true only on the average. In actuality, the wave functions appear to be highly sensitive to the exact disorder.

4. The AC conductivity of a potassium vanadium phosphate glass can be explained in terms of an inhomogeneous structure; the inhomogeneities being a result of either a phase separation or varying degress of order and disorder.

5. Future experimental work should be centered around proving or disproving the existence of a phase separation. This work should include small angle x-ray scattering, transmission electron microscopy, and electrical measurements of splat-cooled V_2O_5 (where a phase separation is impossible). Future theoretical work should center on numerical solutions to the wave functions, based on the proposed models. The theory should also be extended to glasses containing other transition metal oxides.

REFERENCES

[1] N. F. Mott, Adv. Phys. 16, 49 (1967).

[2] J. D. Mackenzie, Semiconducting oxide glasses, Modern Aspects of of the Vitreous State, Vol. 3, p. 126, edited by J. D. Mackenzie. Butterworths (1964).

[3] J. C. Slater, Insulators Semiconductors, and Metals; Quantum Theory Molecules and Solids, Vol. 3, p. 271. McGraw-Hill (1967).

[4] T. Holstein, Annls Phys. 8, 325 (1959).

[5] T. Holstein, Annls Phys. 8, 343 (1959).

[6] S. Urnes, X-ray diffraction studies of glass, Modern Aspects of the Vitreous State, Vol. 1, p. 10, edited by J. D. Mackenzie. Butterworths (1960).

[7] N. F. Borrelli and G. J. Su, Mat. Res. Bull. 3, 181 (1968).

[8] R. J. Bell, N. F. Bird and P. Dean, J. Phys. C 1, 299 (1968).

[9] E. DeDycker and P. Phariseau, Physica 34, 325 (1967).

[10] G. J. Morgan, J. Phys. C 1, 347 (1968).

[11] P. W. Anderson, Phys. Rev. 109, 1492 (1958).

[12] N. F. Mott and W. D. Twose, Adv. Phys. 10, 107 (1961).

[13] R. E. Borland, Proc. R. Soc. A274, 529 (1963).

[14] A. Miller and E. Abrahams, Phys. Rev. 120, 745 (1960).

[15] L. Pauling, The Nature of the Chemical Bond. Cornell University Press (1960).

[16] M. Pollack and T. H. Geballe, Phys. Rev. 122, 1742 (1961).

[17] L. L. Hench and A. E. Clark, to be published.

[18] L. L. Hench and D. L. Kinser, to be published.

[19] L. L. Hench, Structure and properties of glass-ceramics, Engineering Progress at the University of Florida, Vol. 21, No. 6 (1967) p. 2. Engineering and Industrial Experiment Station, Gainesville, Florida.

B. THE EARLY STAGES OF CRYSTALLIZATION OF GLASS (L. L. Hench, D. L. Kinser and S. W. Freiman)

1. INTRODUCTION

It has been well known for many years that when glass is heated at a temperature in the softening range, physical and chemical properties change irreversibly and eventually lead to complete crystallization. Tamman[1] established that the bulk crystallization sequence in glasses consists of two distinct processes, nucleation and crystal growth. These processes may occur separately or concurrently during the crystallization of glasses. Thermodynamic theories have since been developed that describe the kinetics of nucleation and growth in terms of activated complexes[2,3]. The effect of heterogeneities on nucleation and growth kinetics have also been described by thermodynamic arguments. Application of these concepts has been the subject of considerable research[4,5,6] and has led to the development of a new class of glass-ceramic materials[7,8].

However, in spite of the above advances, there is still considerable question as to the structural mechanisms involved in the nucleation of crystal phases in a glass. In particular, little is known about the relationship between the mechanisms of nucleation and growth and the rates of bulk crystallization of glasses. There are at least several reasons responsible for this state of affairs, including the added complexity of including phase separation in structural theories, the difficulty of interpreting changes in multicomponent commercial glass systems, and perhaps most important, the scale of observation required to observe nucleation processes.

It is the objective of the present paper to establish a model for the nucleation process in binary Li_2O-SiO_2 and Na_2O-SiO_2 glasses based on a variety of analytical results. A second objective is to relate the nucleation

process to bulk crystallization kinetics of the glass and the microstructure developed during devitrification.

2. EXPERIMENTAL PROCEDURE

Sample Preparation: The glass was prepared for these experiments by blending 99.9% silica (5μ Min-u-Sil) and 99.3% lithium carbonate in a jar mill and melting for 18-70 hours in air in a covered platinum crucible. The glass compositions and melting temperatures employed are given in Table I. Samples 2.5 cm long and 1.3 cm in diameter of 1.8 cm diameter and 0.5 cm thick were cast in a steel mold, placed in a furnace at a temperature range of 230° C - 300° C and heated for 1-4 hours to relieve stresses to a level sufficient to prevent sample breakage. The cast specimens were subsequently given nucleation and crystallization heat treatments in nichrome wound tube furnaces equipped with aluminum blocks to eliminate temperature gradients. Temperature control was maintained at ± 1°C.

Dielectric Relaxation and D. C. Conductivity: Dielectric absorption spectra were measured on polished glass samples with vapor deposited gold electrodes over a frequency range of 20 Hz to 5 MHz using Wayne Kerr bridges. The source and detector system, sample holder configuration and environmental control system have been discussed in a previous publication[9]. Dielectric loss peaks were measured as a function of temperature over a range of -80° to 200° C with a control of ± 1° C. The oscilloscope, VTVM, and picoammeter system employed to make D. C. conductivity measurements within a range of times of 10^5 sec to 10^{-4} sec have also been described previously[9].

X-Ray Analysis: Bulk crystallization kinetic data were obtained on -200 mesh powders according to the technique of Munch and Pierron (10) using a Norelco x-ray diffractometer with a fine focus Cu tube and curved crystal monochromator. Quantitative analysis of the x-ray data has been discussed in

a recent publication[11].

X-ray identification of the crystals produced in the early stages of the reaction sequence was obtained through the use of a vacuum Guinier-DeWolff camera using CuKα radiation[12].

X-ray small angle scattering (SAS) measurements were made on samples thinned to 0.1 to 0.2 mm thickness after thermal treatments in the form of 1.3 cm diameter by 2.5 cm long cylinders[13]. A Siemans Kratky camera using CuKα radiation and entrance slits of 150μ and exit slits of 50μ was used to measure the scattering intensity over the range of .01° - .2° 2θ.

Microscopy: Microscopy of the reaction sequence occurring in the early stages of crystallization was obtained using hot stage transmission electron microscopy[14]. Samples were reduced to transmission thickness using a special etching procedure[14]. A Philips EM 200 was used for bright field, dark field, and diffraction photographs.

Analysis of the microstructures of the intermediate stages of crystallization was made using carbon replicas of Pt preshadowed etched fracture surfaces.

A Bausch and Lomb Dynoptic polarizing microscope and a Leitz research metallograph were used for quantitative analysis of the microstructures of the final stages of crystallization.

3. EVIDENCE FOR A METASTABLE REACTION SEQUENCE

The compositions of the glasses studied in the Li_2O-SiO_2 system are shown on the phase diagram of the system in Figure 1. Only the disilicate composition in the Na_2O-SiO_2 system has been investigated to date. The as-cast glasses prepared from the compositions outside the disilicate contain microheterogeneous regions, as seen in the replica electron micrograph of Figure 2. It has been concluded in this laboratory[12] and by other investigators[15,16,17] that the heterogeneous microstructure consists of SiO_2 droplets
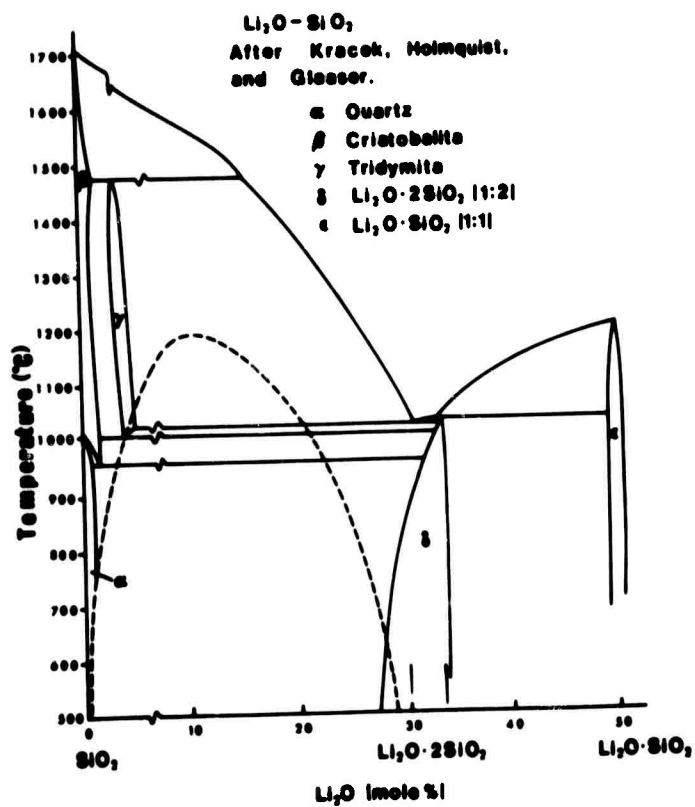
Figure 1 Phase diagram of the lithia-silica system

Figure 2 Replica electron micrograph of 30 mole % lithia-
silica glass as cast.

in a disilicate matrix. It has also been concluded[12,17] that a secondary phase separation of alkali-rich regions occurs within the disilicate matrix.

Of concern is what happens structurally when the microheterogeneous glass is heat treated at temperatures in the nucleation range. Quantitative dielectric absorption has been an important tool in following such structural changes because the alkali-rich regions of the glass gradually lower their free energy by increasing in modifier content, forming isolated islands of near alkali metasilicate composition. When an A.C. field is applied, the presence of the high conductivity, modifier-rich regions in a low conductivity SiO_2-rich matrix gives rise to interfacial polarization. The interfacial polarization results in large Maxwell-Wagner-Sillars (MWS) heterogeneous dielectric losses[12].

It can be observed in Figure 3 that the magnitude of the loss peaks developed in the initially loss-free 30 mole percent Li_2O-SiO_2 glass decreases as the duration of thermal treatment is increased. The decrease in absorption indicates that either the size of the highly conductive regions is decreasing or that the compositional difference between the modifier-rich regions and the SiO_2-rich phases is decreasing with thermal treatment.

A similar sequence of appearance and disappearance of loss peaks has also been observed in other alkali-silicate glasses[18]. The summary of these results in Figure 4 also shows that the changes in loss peak height vary for the different glasses. Consequently, it appears that the kinetics of precipitation and resorption of the modifier-rich phase varies with the modifier content of the parent glass.

Small angle x-ray scattering is also sensitive to heterogeneous structures in glasses[19] and can be used to determine the size of the heterogeneous regions, the composition of the regions, and a number of other structural features[20].
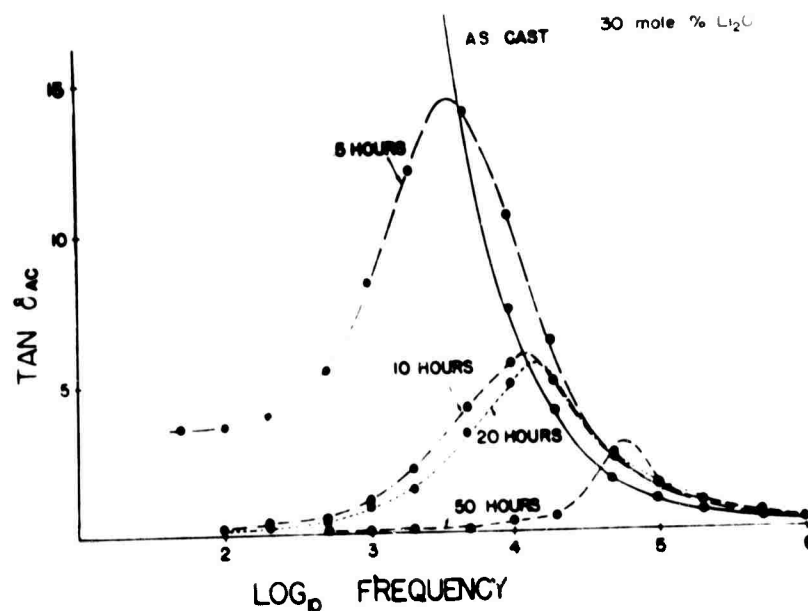
Figure 3   Summary of the dielectric loss behavior at 80°C of a 30 mole % lithia-silica glass thermally treated at 500°C for the times indicated
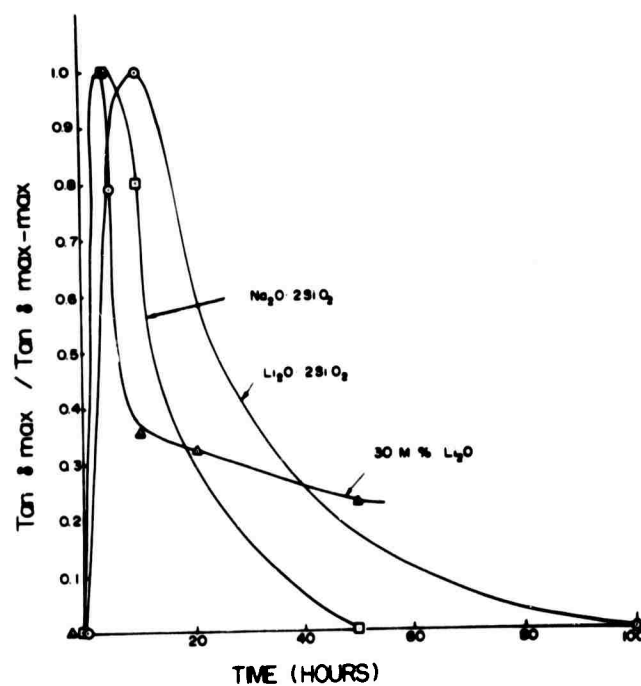
Figure 4   Normalized tan δ behavior at 80°C for various glasses as a function of thermal treatment at 500°C

A parameter (M) directly proportional to the total integrated small angle x-ray scattering intensity is plotted as a function of thermal treatment of the lithia silicate glasses in Figure 5. M is defined as $M = Q_o/K'$ and $K' = 4\pi\tau_o/\lambda^2$ where τ_o is a factor involving the distance between the sample and the detector slit, and λ is the x-ray wavelength. Figure 5 shows that the scattering intensity increases to a maximum with thermal treatment followed by a decline in scattering. The magnitude of scattering intensity is a function of the total volume of the scattering particles and the electron density difference between the particles and the matrix[22]; $Q_o = V \overline{(\rho - \rho_o)^2}$. Therefore, it appears that either the total volume of the scattering particles is changing with thermal history or the compositional difference between the particles and the matrix is changing. The total volume of particles can increase by two alternative methods. The particles can grow during thermal treatment, causing the average radii to increase. Or, new particles may be grown during thermal treatment which would cause the size distribution of particles to change.

Table I represents a summary of the Guinier radius and the Porod radius measured from the scattering curves for various heat treatments. Two features of the data can be noted. First, since both sets of measured radii are close to the same value, the size distribution of the scattering particles is very narrow[23] and does not change with time. Secondly, the size of the scattering particles does not change appreciably with thermal treatment.

Consequently, the stability of the particle size and the size distribution indicates that the change in scattering intensity is due to the compositional difference between the scattering particles and the matrix becoming greater during the first part of the thermal treatment, followed by a reduction in compositional differences in the later stages. Thus, the x-ray small angle

Figure 5a   Transmission electron micrograph of 30 mole %
             lithia-silica glass at 480°C after 35 minutes at
             480°C in the microscope.   Bright field

Figure 5b   Transmission electron micrograph of 30 mole %
             lithia-silica glass at 480°C after 35 minutes at
             480°C in the microscope.   Dark field.

scattering results are consistent with the interpretation that metastable metasilicate particles precipitate in the glass and then resorb as the equilibrium crystal phase appears.

Confirmation that it is the alkali-metasilicate that appears as the isolated metastable phase in the above experiments was obtained from both x-ray and transmission electron microscopic analysis. Lithium metasilicate crystals were detected in the 30 mole percent Li_2O-SiO_2 glass using a Guinier-DeWolff vacuum x-ray diffraction camera[12]. A concentration of approximately 0.1% was observed at heat treatment times corresponding to the maximum scattering intensity and maximum dielectric losses. Additional diffraction lines in the metasilicate pattern indicate that a transition phase of lower symmetry or extensive solid solution may be present. With longer thermal treatments the metasilicate phase disappears, within the detection limits of the diffraction system, leaving only diffuse glass peaks. For longer thermal treatments of up to 50 hours at 500°C, the equilibrium lithium disilicate phase appears.

Figures 6 and 7 show the appearance of the metasilicate crystals in a 30 mole percent Li_2O-SiO_2 glass after a thermal treatment of the electron transmission specimen for five minutes at 480°C. A bright field image and the diffraction pattern of the metasilicate crystals are shown. Indexing the diffraction pattern shows that some disilicate crystals are also present (Table III). A complete sequence of the precipitation and resorption process will be reported in another publication including a discussion of the increased reaction rate due to beam heating and sample thickness.[14]

The simultaneous appearance of both lithium metasilicate and lithium disilicate in selected area diffraction patterns also provides evidence that the resorption of the metasilicate is not completed before the equilibrium phase begins to grow. This observation lends support to the latter argument that the disilicate growth proceeds at the decomposing metasilicate interface.

Figure 6 Electron diffraction pattern of 30 mole %
lithia-silica glass at 480°C after 26 minutes
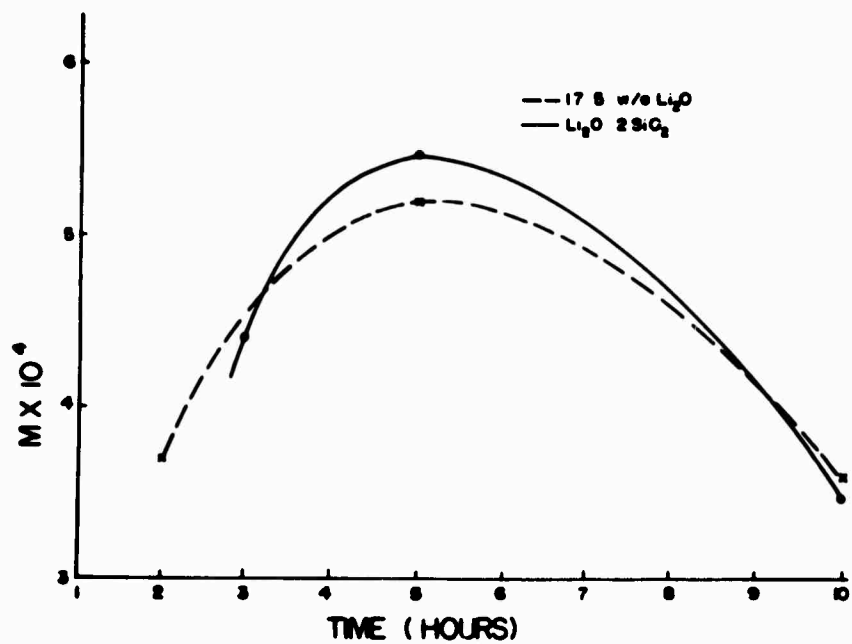at 480°C in the microscope

Figure 7 The effect of thermal treatment time at 500°C on
a parameter related to the total integrated small
angle intensity for two compositions in the
Li_2O-SiO_2 system

As summarized in Table IV, all alkali-silicate compositions investigated appear to follow a metastable reaction sequence similar to that observed for the 30 mole percent Li_2O-SiO_2 glass. The major distinction between the various compositions is that glasses of the disilicate composition do not undergo a liquid-liquid phase separation prior to the metastable precipitation.

By using available thermodynamic data, it has been possible to construct a free energy-composition diagram for the various glasses studied[12,18]. One of the diagrams reproduced in Figure 8 shows that the metastable reaction sequence observed experimentally is consistent with a sequential lowering of the free energy of the system. Crystallization of the alkali-rich regions such as the metasilicate is favored because of its structural simplicity relative to the glass structure. The average free energy of the system is decreased by the amount $G_3 - G_6$ through the metasilicate crystallization.

Reaction of the metasilicate with the SiO_2-rich matrix produces the structurally more complex disilicate crystals and further lowers the free energy by the amount $G_6 - G_8$. Thus, it is the kinetic barriers to nucleation of the structurally complex equilibrium phases that is responsible for the intermediate reaction sequence observed.

4. RELATION OF THE METASTABLE REACTION TO CRYSTALLIZATION KINETICS

A recent publication by two of the authors demonstrated that the crystallization kinetics of a 33 mole percent Li_2O-SiO_2 glass which has had a three hour nucleation treatment at 475°C, insufficient to form a significant concentration of the metasilicate phase, is appreciably slower than a glass of the same composition which has had a 24 hour nucleation treatment at 475°C[11]. The 24 hour treatment produces a large concentration of metastable metasilicate crystals. The accelerating effect of the metasilicate phase on the crystallization rate of the glass is shown in Figure 9. The rate of crystallization is increased by a factor of 1.5. However, it can also be noted that the incu-
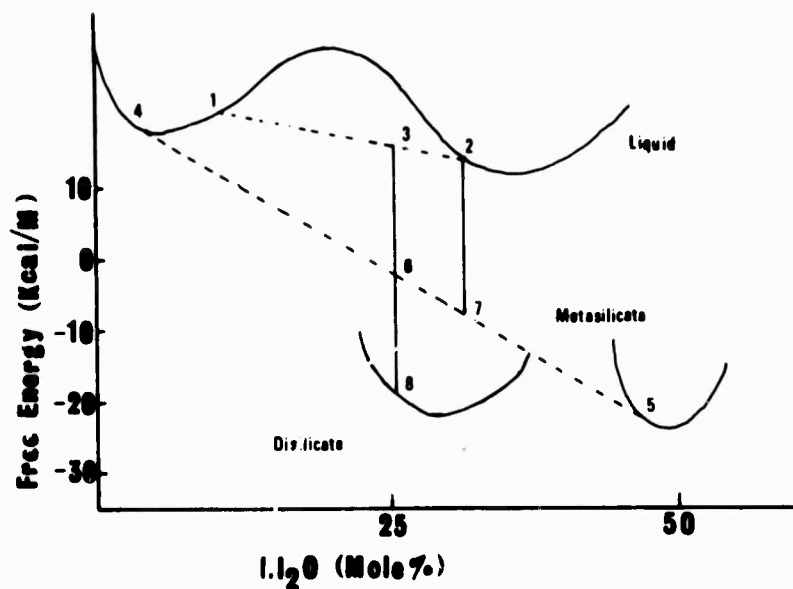
Figure 8   Free energy-composition diagram for lithia-silica
system at 500°C.
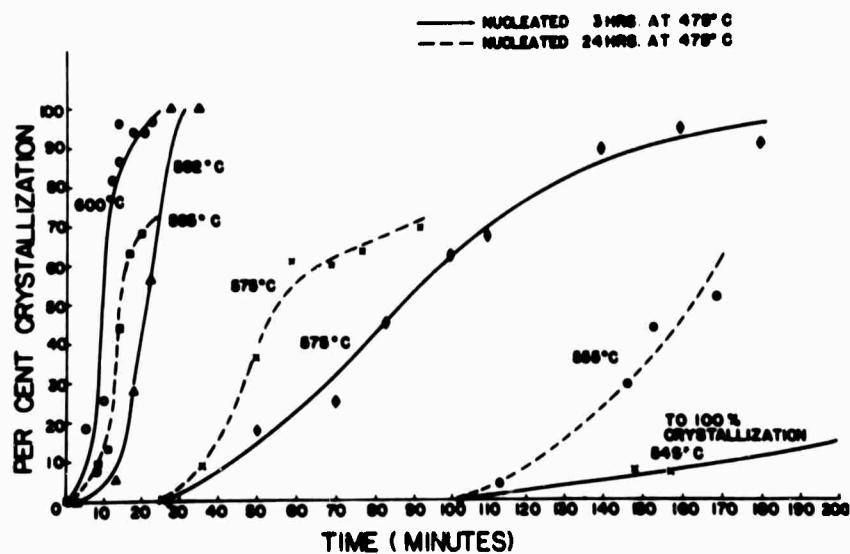
Figure 9   Crystallization of $Li_2Si_2O_5$ from a $Li_2O-2SiO_2$
glass for two nucleation treatments

bation period is constant for the two samples at all temperatures. There-
fore, the activation energy of the incubation process for both samples is
independent of the metastable reaction process.

The activation energy for bulk crystallization is strongly dependent on
prior nucleation treatment. The activation energy for samples with a 24
hour treatment corresponds to that of crystal growth in these systems
(52 kcal/mole), while a sample with a three hour nucleation treatment exhibits
a much higher activation energy (92 kcal/mole). Application of the Johnson-
Mehl-Avrami [JMA] [24,25] analysis to the crystallization data reveals that the
growth of the disilicate crystals is rod-like[11], as is observed in the spheru-
lites grown in the glass studied. The JMA analysis also showed that it is
the activation energy of nucleation that is decreased when the sample has been
given a heat treatment that produces metasilicate as a nucleation step.

The question to be answered is what is the role of the metasilicate particles
in controlling the kinetics of nucleation of the equilibrium disilicate crystals.
Figure 10 depicts a structural model that is proposed to describe the relation
between the metastable reaction sequence and the equilibrium crystallization. The
structural model shows the structural simplicity of the metasilicate lattice and
the structural similarity of the disilicate lattice when alternate Li_2O groups
are removed. Thus, it is proposed that metasilicate crystals form in the glass
by diffusion of Li_2O into Li_2O-rich regions because of preferred Li coordinations
and the relative structural similarity of the metasilicate to the initial
glass structure. With additional heating, Li_2O groups diffuse out of the meta-
silicate, probably as ionic species, producing a disilicate structure from
the SiO_2-rich matrix at the metasilicate interface. It is this diffusional
step which is responsible for the incubation period measured. When a critical
size of disilicate region is reached, the growth proceeds rapidly towards

- ● Silicon
- ○ Oxygen
- △ Lithium
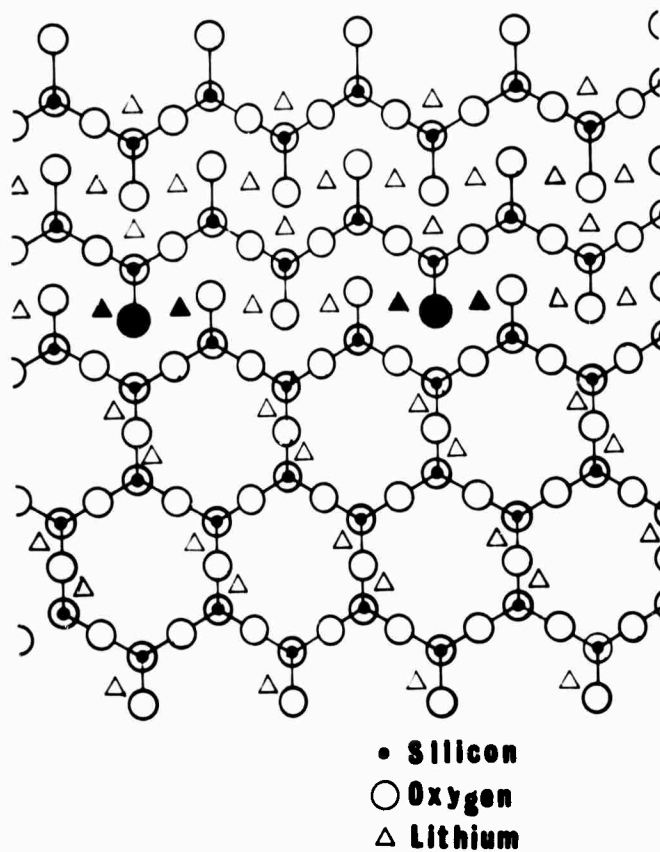
Figure 10   Structural model of the lithium metasilicate nucleation of lithium disilicate crystals. Upper chain structure is a planar representation of the Li_2O-SiO_2 lattice. The lower sheet-like structure is a planar projection of the $Li_2O \cdot 2SiO_2$ lattice

completion. Because of the difficulty of Li_2O groups diffusing through the disilicate structure, it is energetically easier for the diffusion to occur at the ends of the dendrite arms, thus producing the spherulitic structures occurring in these glasses.

When a glass has been given a nucleation treatment which develops a large concentration of the highly ordered metasilicate regions, rapid crystal growth proceeds from many sites. The final spherulite size is small, the number per unit volume is large, and the size distribution is small, as observed. As the spherulites envelop the ordered regions developed around each metasilicate site, the nucleation barrier in the growth of new dendrite arms is lowered, as observed, and the overall bulk crystallization rate is accelerated, also as observed. This is the process the authors refer to as internally activated nucleation.

The basis for internally activated nucleation may be seen thermodynamically if one looks at the equation given for heterogeneous nucleation rate[26].

$$I = \sum_{j=0}^{j=max} \frac{N_j}{V} \; K_j \; exp - \frac{\Delta F_j^* + \Delta F_a}{kT}$$

I is the nucleation rate; N_j/V is the number of nucleation sites per unit volume; K_j is the frequency factor; ΔF_j^* is the energy necessary to form a stable nucleus at a particular site j; ΔF_a is the activation energy for a molecule to detach itself from the glass and attach itself to the growing nucleus. At large degrees of supercooling, such as occurs in the crystallization of glass, ΔF_a is the predominant term and, therefore, governs the rate of crystallization. It is essentially this energy that is measured as the activation energy for nucleation. It is easy to see that ordering around the metasilicate

regions should reduce the energy barrier which must be overcome in order to transfer a molecule from the glass to the crystalline state, thereby reducing the activation energy for nucleation.

When the nucleation treatment has been insufficient to develop a large concentration of ordered metasilicate regions, the incubation time for crystal growth remains the same as the internally activated process because the diffusional step must still occur. The incubation activation energy remains the same, 100 kcal/mole as observed. Much fewer sites reach critical size, however, and the bulk crystallization rate is therefore slow. The spherulites do not envelop ordered regions during growth and the nucleation activation energy is high.

5. SUMMARY

The appearance of metastable phases as a step in a transformation sequence is not without precedent. Ordered regions in super-saturated metallic solid solutions called Guinier-Preston zones appear and eventually disappear prior to equilibrium precipitation[27,28]. Roy proposed metastable reaction processes in the thermal treatment of glass several years ago[29]. McMillan and Partridge suggested that the presence of a metastable lithium metasilicate phase influenced the properties of $Li_2O-ZnO-SiO_2$ glass-ceramics[30]. Recently, several investigators have reported variations in properties with thermal treatments which cannot be explained by liquid-liquid immiscibility effects and imply that metastable phases are present[31,32].

Consequently, it appears that the metastable reaction sequence investigated in the Li_2O-SiO_2 and Na_2O-SiO_2 glasses may be generally observed as a precursor to equilibrium crystallization. It also appears likely that the influence of ternary or multicomponent additions in the crystallization behavior of alkali-silicate glasses could be one of either enhancing or retarding the

development of the metastable phase. For example, the retardation of

crystallization of Li_2O-SiO_2 glasses by 3% TiO_2 additions is apparently due

to the metasilicate failing to appear because of the titanium ion compe-

tition for oxygen ions[11]. When the metastable phase does precipitate, it

is a very efficient nucleating site; consequently, it is possible to control

particle sizes through the use of internally activated nucleation without

adding heterogeneous agents to the glass[33].

Another consequence of the metastable reaction sequence is the possibility

of drastic structural and property changes in a glass without crystals appear-

ing in a quantity detectable by routine diffraction methods. This may mean

that glasses which have been given an extended annealing at high temperatures

or have been heated for long durations at elevated temperatures, such as

diffusion experiments or many property measurements, can yield data character-

istic of a heterogeneous glass-crystal morphology and not that intrinsic to

the glass itself. Detailed documentation of the thermal history of all glass

experiments must therefore be deemed essential in light of these results.

REFERENCES

1. Tamman, G. (1925) J. Soc. Glass Tech. 9, 166.

2. Turnbull, D. and Cohen, M. H. (1963) Modern Aspects of the Vitreous State, p. 45. Butterworths Scientific Publications, London.

3. Hillig, W. B. and Turnbull, D. (1956) J. Chem. Phys. 24, 914.

4. Morley, J. G. (1965) Glass Technology 6 (3) 77-89.

5. Reser, M. K., editor (1962) Symposium on Nucleation and Crystallization in Glasses and Melts. The American Ceramic Society, Columbus, Ohio.

6. Porai-Koshits, E. A., editor (1958-65) The Structure of Glass, Volumes 1-5. Consultants Bureau, New York.

7. Stookey, S. D. and Maurer, R. D. (1967) Progress in Ceramic Science, Volume 2, pp. 77-103. Pergamon Press, New York.

8. McMillan, P.W. (1964) Glass-Ceramics. Academic Press, New York.

9. Hench, L. L., "Applications of Dielectric Relaxation in Materials Analysis," Society of Aerospace and Mechanical Process Engineers Fourteenth Symposium, November 5, 1968, Cocoa Beach, Florida.

10. Munch, R. H. and Pierron, E. D. (1963) Norelco Reporter X (2) 75-76.

11. Freiman, S.W. and Hench, L.L. (1968) J. Am. Ceram. Soc. 51 (7) 382-387.

12. Kinser, D. L. and Hench, L. L. (1968) J. Am. Ceram. Soc. 51 (8).

13. Freiman, S. W., Gould, R. W. and Hench, L. L., "An X-Ray Small Angle Scattering Study of Crystallization in Glass," presented at the 1968 American Ceramic Society Convention, Chicago. To be published.

14. Kinser, D. L., Hench, L. L. and Hren, J. J., "Direct Observation of Crystallization of Li_2O-SiO_2 Glasses by High Temperature Transmission Electron Microscopy." To be published.

15. Charles, R. J. (1963) J. Am. Ceram. Soc. 46 (5) 234-243.

16. Vogel, W. and Byhan, H.G. (1964) Silikattechnik 15 (7) 212-218.

17. Kalinina, A.M., Filipovich, V.N., Kolesova, V.A. and Bondar, I.A. (1964) The Structure of Glass, Volume 3, pp. 53-64. Consultants Bureau, New York.

18. Kinser, D. L. and Hench, L. L., "Electrical Properties of Thermally Treated Alkali-Silicate Glasses." To be published.

19. Goganov, D. A. and Porai-Koshits, E. A. (1965) <u>The Structure of Glass</u>, Volume 5, pp. 82-89. Consultants Bureau, New York.

20. Gould, R. W. (1967) Proceedings of Fourth Space Congress; Technical Paper No. 378, Engineering Progress at University of Florida (June 1967).

21. Gerold, V. (1967) <u>Small Angle X-Ray Scattering</u>, edited by H. Brumberger. Gordon and Breach, New York.

22. Guinier, A. (1963) <u>X-Ray Diffraction</u>, p. 338. W. H. Freeman and Company, San Francisco.

23. Harkness, S. D., Gould, R. W., and Hren, J. J., "A Critical Evaluation of X-Ray Small Angle Scattering Parameters by Transmission Electron Microscopy: GP Zones in Al Alloys." Accepted for publication in <u>Phil. Mag</u>.

24. Johnson, W. A. and Mehl, R. F. (1939) <u>Trans. AIME</u> <u>135</u>, 416.

25. Avrami, M. (1939) <u>J. Chem. Phys</u>. <u>1</u>, 1103.

26. Fine, M. E. (1964) Phase Transformations in Condensed Systems, p. 43. MacMillan Company, New York.

27. Thomas, G. (1961-62) <u>J. Inst. Metals</u> <u>90</u>, 57.

28. Guinier, A. (1959) <u>Solid State Physics</u>, Volume 9, p. 294. Academic Press, New York.

29. Roy, R. (1962) <u>Symposium on Nucleation and Crystallization in Glasses and Melts</u>. American Ceramic Society, Columbus, Ohio.

30. McMillan, P. W.,Phillips, S. V. and Partridge, G. (1966) <u>Journal of Materials Science</u> <u>1</u>, 269-279.

31. Filipovich, V. N. and Kalinina, A. M., "On the Mechanism of the Influence of Precrystallization Heat Treatment on the Crystallization Kinetics of Silicate Glasses," presented as paper 46 at the Int. Glass Congress, London, 1968.

32. Connen, M., "Kinetics of Crystallization and Segregation in Na_2O-SiO_2 Melts," presented as paper 44 at the Eighth Int. Glass Congress, London 1968.

33. Freiman, S. W. and Hench, L. L., "Mechanical Behavior of Lithia-Silicate Glasses," presented at the Eighth Int. Glass Congress, London, 1968. To be published.

III. Measurement Techniques and Analysis (R. W. Gould, J. J. Hren, L. L.
      Hench, and J. K. Watson

A. X-RAY ANALYSIS (R. W. Gould and J. J. Hren)

The x-ray research conducted during this period comprises two related
efforts: 1) supporting analytical analysis and 2) basic x-ray oriented
research. Both will be discussed in this report.

The basic x-ray research has been largely devoted to particle size dis-
tribution analysis as determined by small angle x-ray scattering. This work,
which has been under development for approximately one year, has been stimu-
lated by the need for such information in connection with the degenerate
semiconductor research program.[1] Small angle x-ray scattering research has
been augmented by the optical diffraction analog approach, which will also
be discussed in this report.

A new laboratory for x-ray topographic analysis (Lang technique) has
been set up during the summer of 1968. This laboratory will be utilized for
basic and support research in the degenerate semiconductor program.

A significant portion of the research effort of the x-ray group has been
devoted to the solution of analytical problems arising from various THEMIS
research groups. The most notable problem has been the quantitative micro-
probe analysis of Permalloy thin films (See Section III-B). In addition, crystal
orientation analysis has been performed for various groups.

1. PARTICLE SIZE ANALYSIS BY SMALL ANGLE X-RAY SCATTERING

Small angle x-ray scattering has been used to find the average dimensions
of particles in dispersed suspensions. It is especially convenient in studies
of small particles with diameters of the order of 30 to 5,000 angstroms. A
knowledge of the average particle dimension is often insufficient to character-
ize a particle system, and information must be obtained on the distribution

of particles if meaningful correlation with properties is to be obtained.

X-ray methods for the determination of particle distribution analysis have been attempted for some 20 years. The early work of Schull[2], Roess[3], and Risemann[4] independently showed that, in principle, small angle x-ray scattering could be used to determine the distribution of particle diameters in dilute suspensions of spherical particles. It must be emphasized that the systems in which particle distribution analysis has been successful have been dilute systems containing, in general, less than 2 vol. % of dispersed phase. This early work of Roess and Risemann was never applied to experimental scattering data since at the time of their work (1940's and early 1950's) small angle scattering theory and techniques were not sufficiently developed to make the method practical.

Recent investigations by Schmidt[5,6] and his students suggest that, by modifying the earlier work of Roess and Risemann, diameter distributions can be found from small angle x-ray scattering provided that the systems are dilute and the particles are equiaxed.

The restriction for dilute particle densities is based upon the need for independent particle scattering. When particle densities exceed a certain lower limit, interferences occur between scattering originating at the individual particles. The interparticle interference causes great difficulty with interpretation of the small angle scattering data, especially with regard to the determination of particle size distribution by the integral transform method.

Schmidt and his students have approached the matter of particle size distribution from an elegant point of view that was originally taken by Roess. This school obtains the particle size distribution directly from the integral transform of the small angle scattered intensity. This method has the advan-

-87-

tage that it requires no assumptions concerning the type of particle distribution found in the real systems. The integral transform is conveniently evaluated by numerical analysis techniques, and Schmidt has tested the practicality of his method on theoretical scattering curves and some experimental scattering curves of Ludox (small spherical particles of silica of known size distribution).

Small angle x-ray scattering has been applied to pre-precipitation metallurgical systems for the past ten years. These systems contain 5 to 10% by weight of scattering particles and thus cannot be considered dilute. In general, interparticle interference effects are clearly evidenced in the small angle scattering curves of metallic alloys. Thus the methods described by Roess, Risemann and Schmidt are clearly out of their theoretical bounds when alloy systems are being considered.

For this reason, the work in this laboratory has been largely devoted to determining a system which could provide the particle diameter distributions in systems where interparticle interference did occur. Recently, Harkness, Gould and Hren[7] have addressed this problem and derived a method for obtaining particle diameter distributions from systems such as aluminum-zinc and aluminum-silver, where the particles are spherical but the system is not dilute. This method has been described in a recent paper and will be briefly outlined below.

The basis of this system is a presupposition concerning the form of the particle distribution function. This particle distribution function is then related to parameters which can be obtained from the small angle scattering curve. Harkness, Gould, and Hren[7] showed that the size distribution function, in this case log normal, could be written in terms of simple small angle scattering parameters. Equation (1) is the log normal size distribution function.

$$f(x) = \frac{1}{(\sqrt{2\pi})(x)(\ln \sigma)} \quad \exp - \frac{1}{2} \left(\frac{\ln \mu - \ln x}{\ln \sigma}\right)^2 \tag{1}$$

The geometric mean and the variance σ may be expressed as shown in Equation (2) in terms of a general moment equation of the log normal distribution function.

$$r^n = \exp[n \ln \mu + \left(\frac{n^2}{n}\right) \ln^2 \sigma] \tag{2}$$

Baur and Gerold[8] showed (for a line shaped x-ray beam) that the Guinier radius, R_G, could be expressed by Equation (3) and the Porod radius, R^*, by Equation (4).

$$R_G = \left[\frac{<R^7>}{<R^5>}\right]^{1/2} \tag{3}$$

$$R^* = \frac{<R^3>}{<R^2>} \tag{4}$$

These equations are simply ratios of moments of the particle size distribution function. Thus, if the size distribution function is assumed, these ratios may be easily calculated.* When this is done for the log normal distribution, Equations (5) and (6) are obtained.

$$R^* = \exp(\ln \mu + 2.5 \ln^2 \sigma) \tag{5}$$

$$R_G = \exp(\ln \mu + 6 \ln^2 \sigma) \tag{6}$$

when Equations (5) and (6) are solved for μ and σ, one obtains the following expressions:

$$\ln = \ln R_G - 1.71 \ln \frac{R_G}{R^*} \tag{7}$$

---

* While this is true for the log normal distributions, calculations of this nature for the normal distributions prove to be extremely difficult.

$$\ln^2 \sigma = \frac{\ln \dfrac{R_G}{R^*}}{3.5} \tag{8}$$

This then gives the form of the size distribution curve in terms of the small angle scattering parameters alone, for if μ and σ are substituted into Equation (1), $f(x)$ may be obtained for any x desired.

During the summer of 1968 Gould and Bates[9] have applied this method of analysis to the determination of larger particle sizes, such as those found in dispersion hardened nickel alloys. The details of this work appear in Section III-A-2. This effort demonstrated the applicability of this method to larger particle sizes than are normally found in the GP zone metal systems.

In addition, Harkness and Gould[10] have also utilized this method to follow the growth of Guinier-Preston zones by following the change in the particle size distributions with time. This is a major advance over previous methods in which only one particle diameter could be monitored during the growth of a dispersed phase.

Utilizing the data obtained by Letcher and Schmidt[5], Gould in some unpublished results has applied the HGH[6] analysis to known particle distribution systems, such as Ludox* spheres. Figure 1 shows the small angle scattering intensity obtained by Schmidt's students for three Ludox samples. Figures 2 and 3 show the particle distribution results from the Letcher-Schmidt[4] analysis (integral transform method) and Figure 4 is the corresponding result obtained by the simpler HGH analysis.

In Ludox I (Figure 2) the most probable particle diameter as obtained from the manufacturer was approximately 70 angstroms. For Ludox III (Figure 3) the average diameter obtained by Schmidt was 55 angstroms, while the manufacturer's average diameter was 140 angstroms. Note that the present analysis (Figure 4)

----

* Ludox samples were colloidal silica obtained from Dupont Chemical Corporation whose particle size distribution has been determined by electron microscopy.
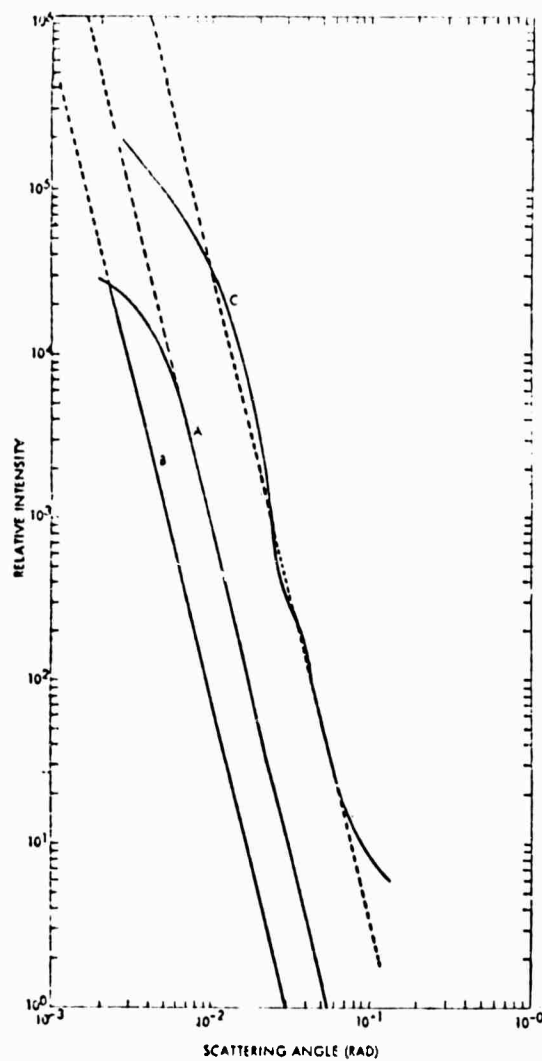
Figure 1
   Slit Corrected xray Scattering Curves for Ludox Samples.
Curves A, B, and C represent Ludox III, Ludox II and Ludox I
respectively (after Letcher and Schmidt   (4)
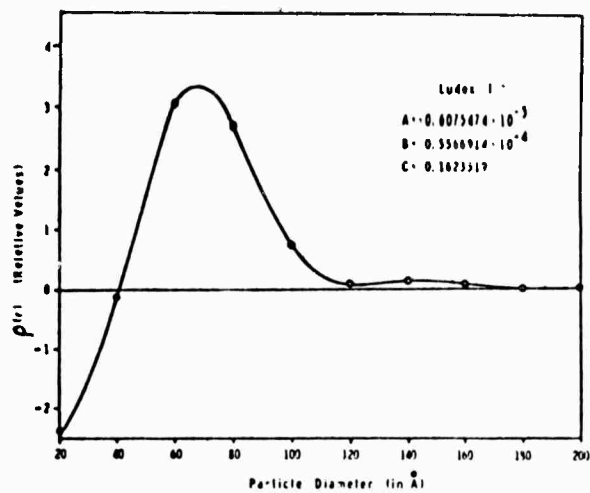
Figure 2
   Particle Size Distribution for Ludox I   (4)
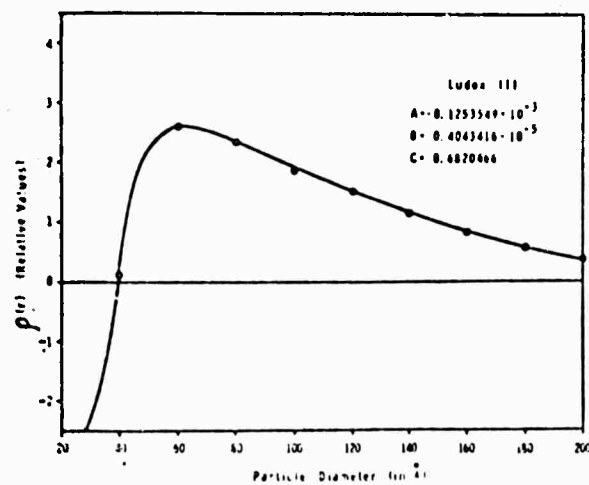
Figure 3
   Particle Size Distribution for Ludox III   (4)

FIG. 4
LUDOX III Data from J. H. Letcher and
P. W. Schmidt

$2R_G = 264$ Å

$R_P = 42$ Å

Particle Diameter (Å)

$F(X) \times 10^3$
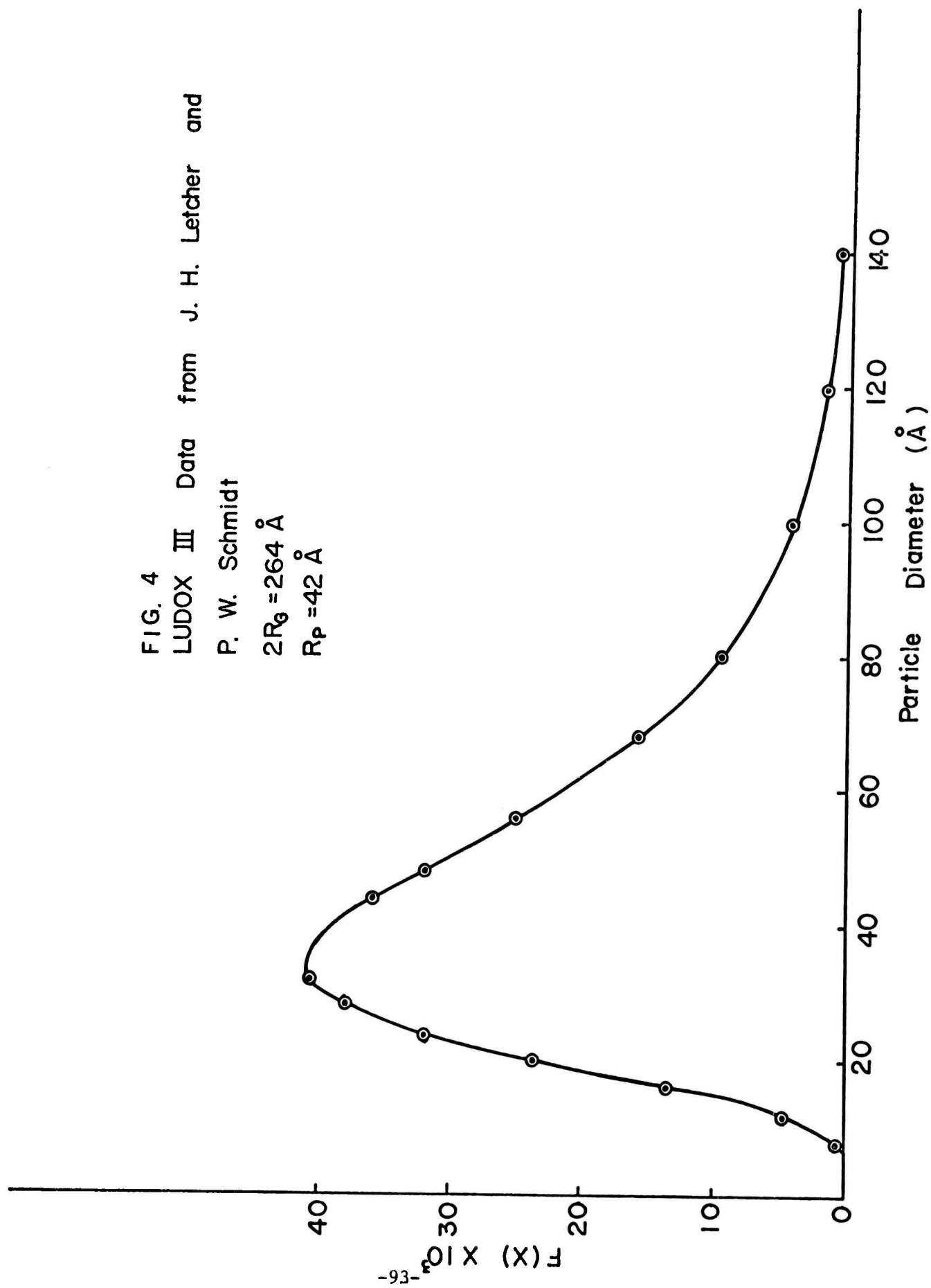
shows an average particle diameter of approximately 40 Å, which is also lower than the manufacturer's data.

Note also that the curves given by Schmidt do not appear to have a realistic size distribution, particularly at the large particle end of the size distribution. This, Schmidt explains, is due to a series termination effect and has been corrected somewhat in a later paper[6]. In order to carry out the analysis of the Schmidt data, it was necessary to rederive the equations given in the HGH paper since the Schmidt data had been "desmeared" to obtain collimation corrected data. These equations for the mean and the variance of the log normal distribution for "desmeared" small angle scattering intensity are given below.

$$R_G = \left[\frac{<R^8>}{<R^6>} \right]^{1/2} = \exp[\ln \mu + 7 \ln^2 \sigma] \tag{9}$$

$$R^* = \frac{<R^3>}{<R^2>} = \exp[\ln \mu + 2.5 \ln^2 \sigma] \tag{10}$$

$$\ln^2 \sigma = \frac{\ln R_G/R^*}{4.5} \tag{11}$$

$$\ln \mu = 1.56 \ln \frac{R_G}{R^*} \tag{12}$$

Note for point collimation that

$$R^* = \frac{<R^3>}{<R^2>} = \frac{3Q(0)}{2\pi^2 (1-c) s^4 I(s)} \tag{13}$$

and

$$Q(0) = \int_0^\infty s^2 I(s)ds \qquad \text{where} \tag{14}$$

$$\int_0^\infty s^2 I(s)ds = s \sum_0 s^2 I(s_o) s_o^3 \tag{15}$$

The Harkness-Gould-Hren method has also been applied to some additional Ludox scattering data obtained from a paper by Rothwell[11]. Figure 5 shows the small angle scattering curves for various concentrations of type AS Ludox, where $h = 2\pi(\frac{2\theta}{\lambda})$. Note the interparticle interference effects appearing in the 0.16 vol. % sample, as evidenced by the small interference peak at $h \cong 2.6 \times 10^{-2}$.

Figure 6 shows the effect that concentration has upon the Guinier radius which is often used to characterize a particle system. Note that in this figure it is given as a diameter where $D = 2x$(Guinier radius). Note also that the diameter changes markedly with concentration and, in this case, the diameter decreases as the concentration of particles increases.

Figure 7 shows the small angle scattering curves for glassy carbon containing a rather high concentration of small spherical voids. The curve marked with the small circles represents a sample that was heat treated at 3000° C, producing voids having a Guinier radius of approximately 25 $\overset{\circ}{A}$ and containing approximately 5×10^{-18} particles.

One of these curves was analyzed with the HGH method described in the previous paragraphs and the size distribution obtained is shown in Figure 8. The analysis of all of these results has not been completed, but indications are that the method described by Harkness, Gould, and Hren can be applied to particle size distribution analysis in non-dilute systems. It appears to suffer somewhat from interparticle interference effects, probably due to the effect of interparticle interference on the determination of the Guinier radius.

Figures 5A and 5B show the result of the HGH analysis when applied to the Ludox scattering data given by Rothwell (10).
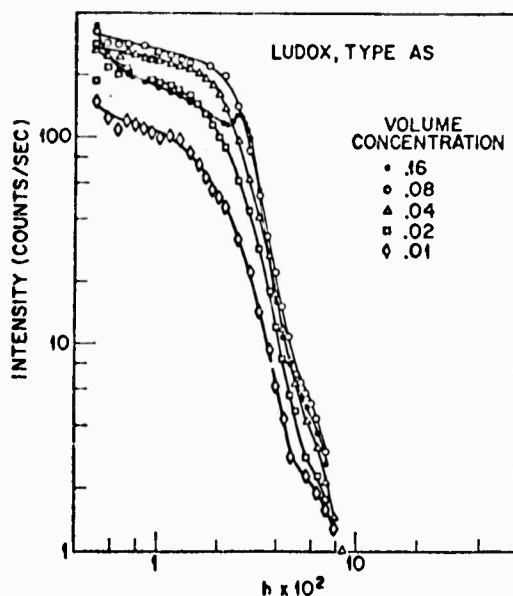
Figure 5
Small Angle X-Ray Scattering Curves for Various
Concentration Solutions of Type AS Ludox, $h = 2\pi (2\theta/\lambda$
(Ref. 10)
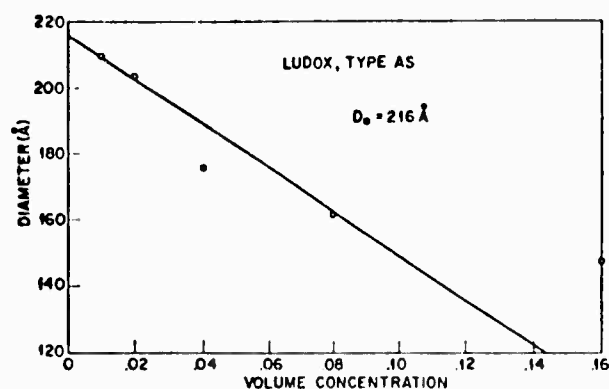
Figure 6
Effect of Concentration of Ludox on Particle
Diameter Measurement. Diameter = 2 x (Guinier radius)
Ref. 10)

FIG 5A
LUDOX TYPE AS

$C_V = 0.01$ Data from W. S. Rothwell

$2R_G = 210 \text{Å}$

$R_P = 68 \text{Å}$

Particle Diameter (Å)

$F(X) \times 10^3$
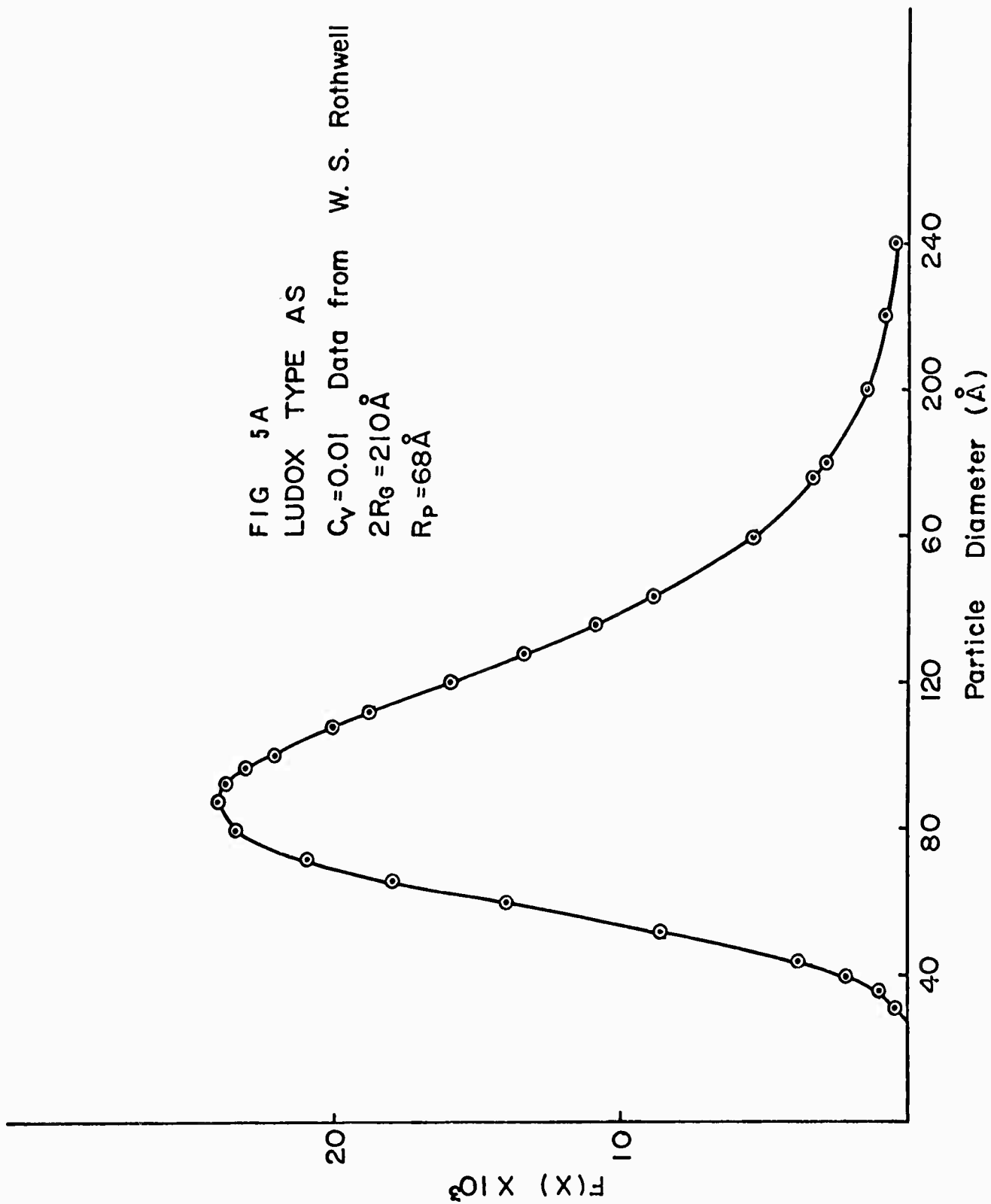
FIG 5i
LUDOX TYPE AS

$C_v = 0.08$ Data from W. S. Rothwell
$2R_G = 160 \text{ Å}$
$R_P = 73 \text{ Å}$

F(X) X 10^3

Particle Diameter (Å)
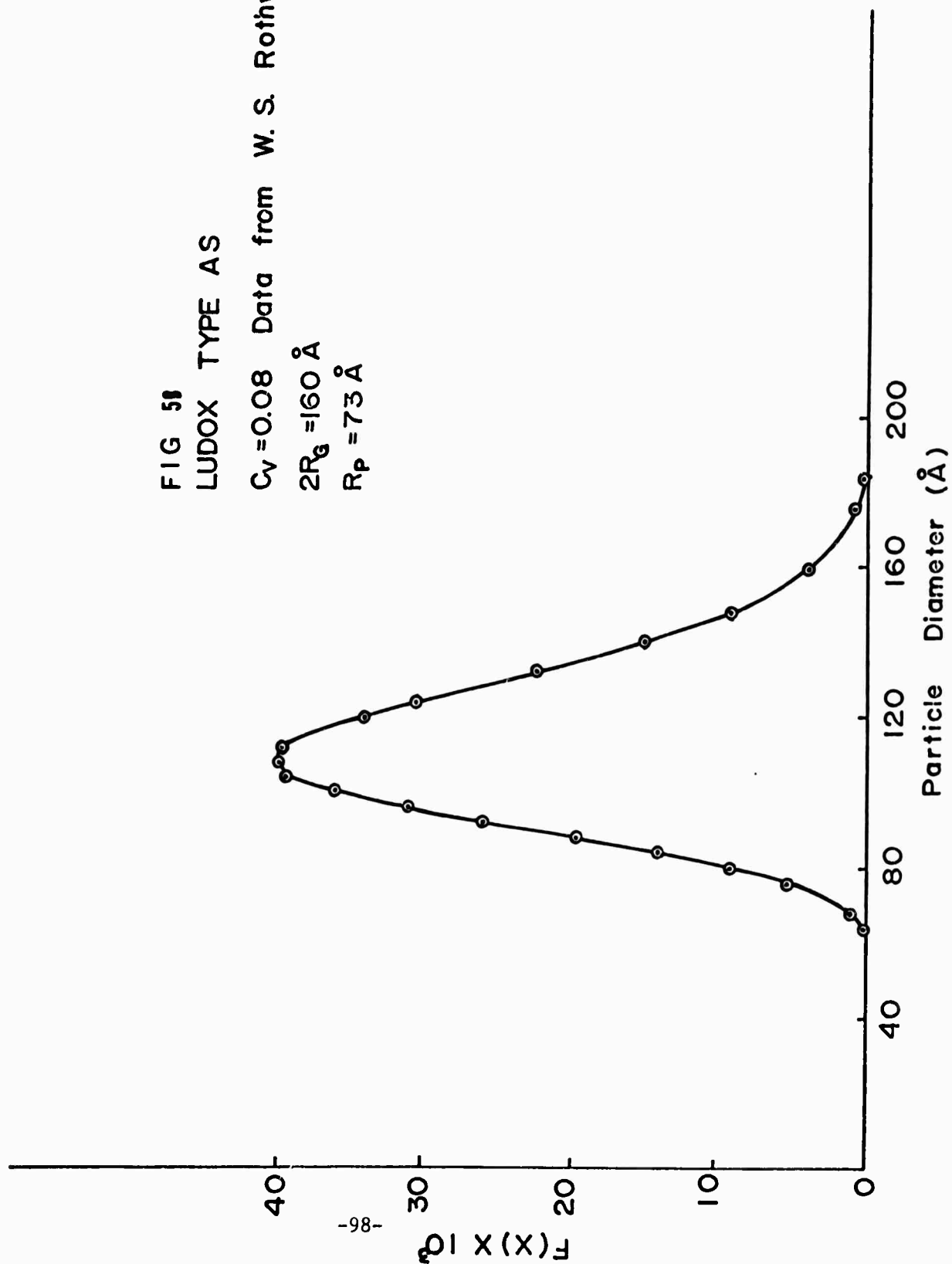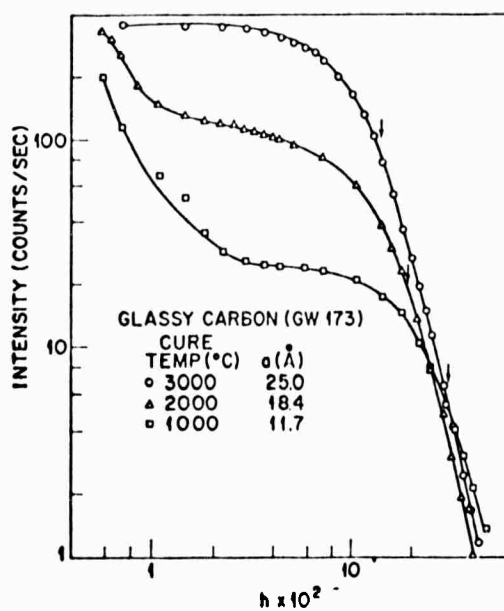
Figure 7

Small Angle Scattering data for Glassy Carbon after Rothwell (10)

FIG 8
VOIDS IN GLASSY CARBON (GW 173)
Data from W. S. Rothwell
$2R_o = 50\text{Å}$
$R_P = 15.5\text{Å}$

Particle Diameter (Å)

$F(X) \times 10^3$
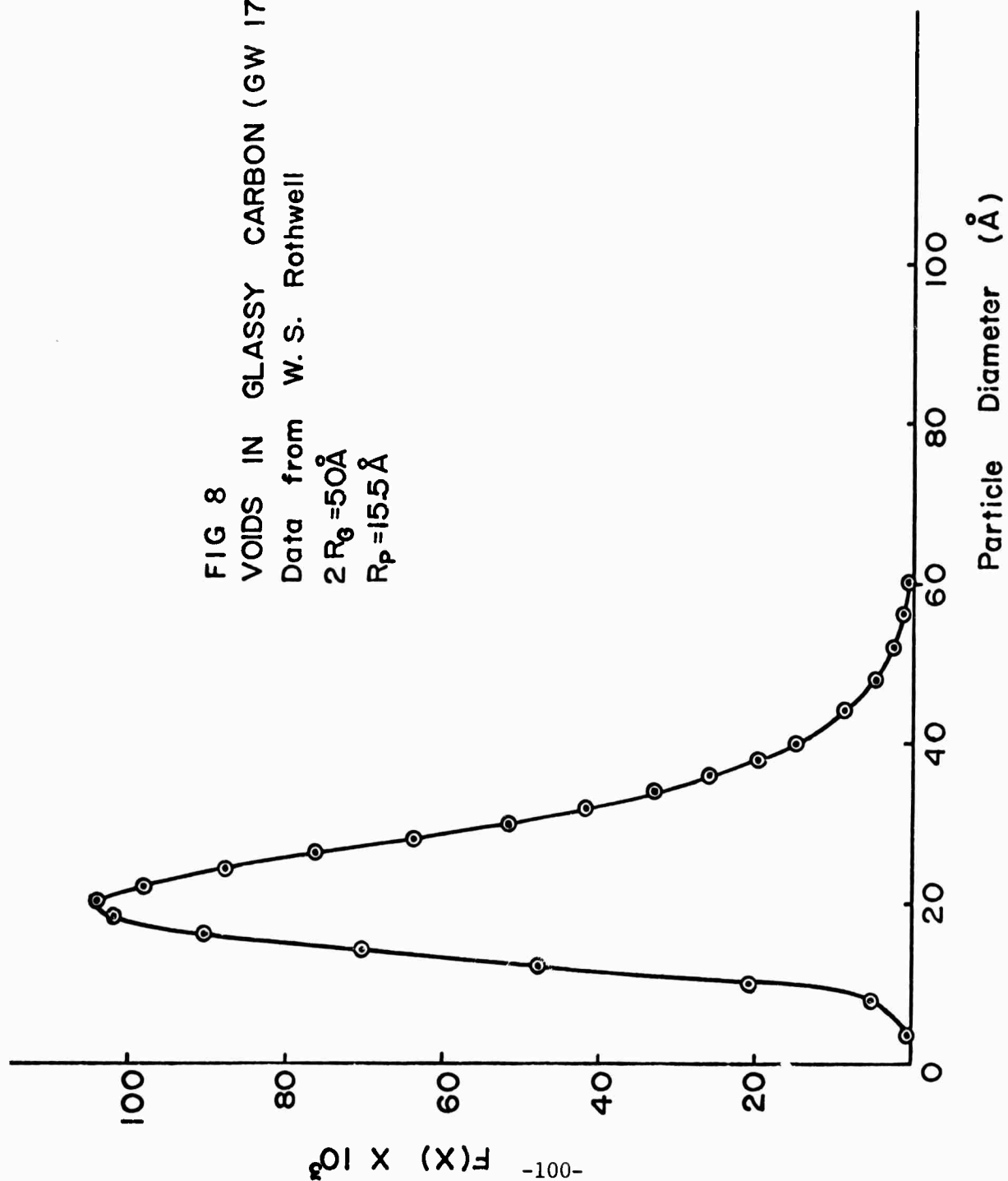
a. OPTICAL DIFFRACTION MODELING IN PARTICLE SIZE DISTRIBUTION ANALYSIS

When applied to x-ray diffraction, Fourier transform theory states that the observed diffraction pattern is directly related to the Fourier transform of the real crystal. This Fourier transform of the real crystal may be shown to consist of a product of Fourier transforms of various factors: a peak function representing the crystal lattice, a shape function to represent the size and shape of the crystal, and a function representing the contents of the single repeat unit in real space. When the Fourier transforms of these functions are convoluted with the Fourier transform of the several instrument factors, the result is directly proportional to the observed diffraction pattern.

It may be shown that this approach is not limited to crystalline materials, but may easily be applied to other states of matter. Bragg in 1939 constructed a diffraction grating consisting of holes drilled in an opaque plate at the relative positions of reciprocal lattice points. When light was transmitted by these holes, the diffraction pattern was formed. This diffraction pattern is remarkably similar to the x-ray diffraction pattern obtained form the real crystal whose reciprocal lattice net was used as a model for the optical mask. This correspondence is an exposition of the fundamental of image formation expounded by Abbe in 1873.

This analogy between the scattering of light by a series of regularly spaced holes and the diffraction of x-rays or electrons by regularly spaced atoms on a periodic lattice has been utilized to understand diffraction theory more fully. The Fourier transform method requires that the position of the various scattering centers (atoms, molecules, clusters, etc.) be specified. Equation (16) shown below then gives the scattering wave amplitude, $G(\vec{S})$, from n scattering

units whose positions are given by a vector (r_n).

$$G(\vec{S}) = \sum_{n=1}^{N} f_n(\vec{S}) \; 2\pi \; i\vec{r}_n \cdot \vec{S} \qquad (16)$$

The scattering amplitude may be evaluated in a computer and the resulting function G(S) may be obtained over a portion of reciprocal space.

A far easier and more convenient way of carrying out this Fourier transform is by means of optical diffraction analogs. Utilizing this method, models may be made by simple drafting techniques, photographically reduced, and a diffraction pattern obtained in a matter of minutes. Thus rapid testing of various models is facilitated. An optical diffraction laboratory has been set up in the Department of Metallurgical and Materials Engineering by Dr. R. W. Gould. At the heart of the laboratory is a Rank-Pullin optical diffract-ometer which has been modified to be used with a gas laser light source. This device is being used to model particle distribution scattering theory. Scattering from such lattice heterogeneities, including dislocations, vacancy clusters, and GP zones is being compared with theoretical scattering equations and with experimental results from small angle x-ray scattering.

Such optical diffraction modeling is not new. Hosemann[12], Taylor and Lipson[13], among others, have been active in this field although it has not obtained the attention that it justly deserves. Recently, the optical diffraction method has been applied to the interpretation of low energy electron diffraction patterns[14], providing a new and powerful method for the unraveling of these sometimes complex surface diffraction effects. Figure 9 shows some optical diffraction models of systems containing spherical particles of varying concentration and polydispersity. These figures were obtained by Hosemann[12] and the corresponding optical diffraction patterns are given below each model.
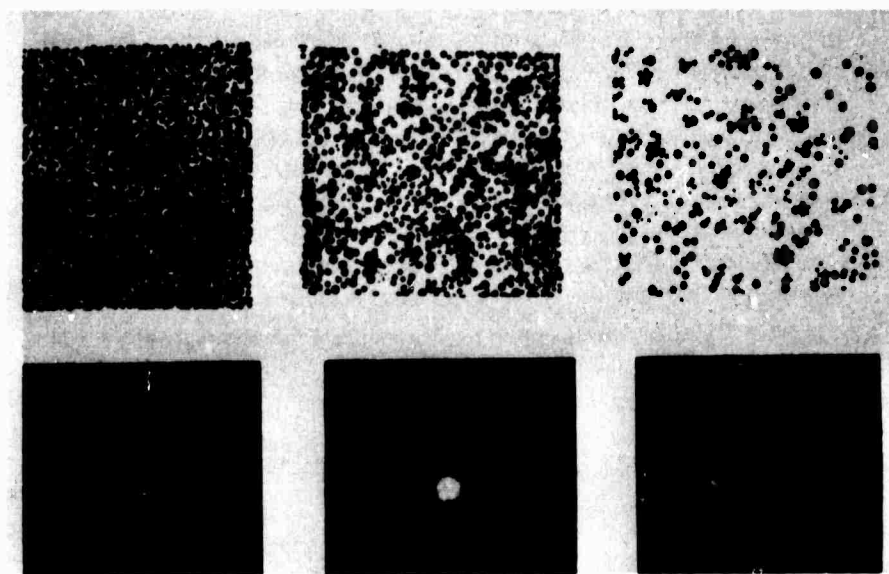
Figure 9
Optical Diffraction Models and Patterns for Spherical
Particle Systems of Varying Concentration (after Hosemann 11)

Microdensitometer curves through these optical diffraction patterns (after suitable correction for intensity) are shown in Figure 10. These curves are analogous to small angle x-ray scattering curves. Thus, in this case, the particle system is completely under control and one can analyze scattering effects from a predetermined distribution of sizes with a far greater freedom than is available in natural particle systems.

b. APPLICATION TO DEGENERATE SEMICONDUCTORS

The optical diffraction method will be used to model the distribution of scattering particles in degenerate silicon and germanium. Observed scattering curves will be interpreted with the aid of optical models, such as the ones shown in Figure 9. Note that a large number of scattering centers are required to simulate natural conditions. The models shown in Figure 9 contain an average of 2,000 or more spherical particles. In order to eliminate diffraction "ghosts" it is necessary to rotate these masks in the optical diffracto- meter during exposure.
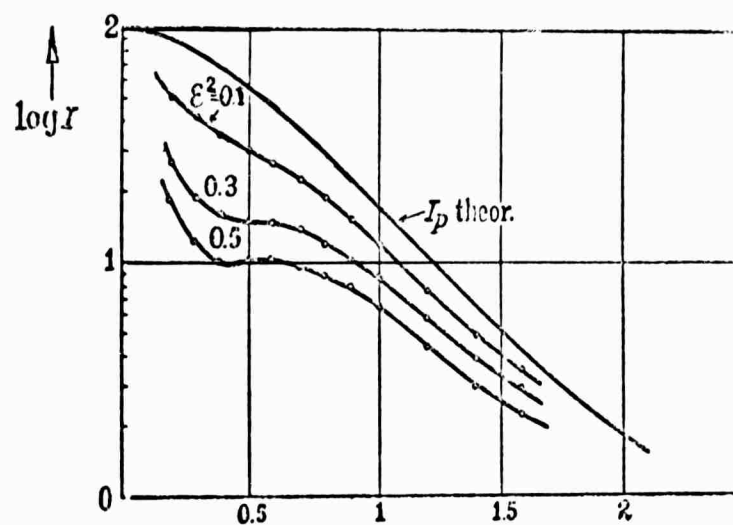
Figure 10
    Microdensitometer Trace of Middle Optical Diffrac-
tion Pattern of Figure 9. Log intensity plotted versus
diffraction angle.

REFERENCES

1. F. A. Lindholm et.al., Scientific Report No. 1, Contract No. F 19628-68-C-0058, College of Engineering, University of Florida, pp 64-65, 10 April 1968 (prepared for AFCRL, United States Air Force, Bedford, Mass.)

2. C. G. Schull and L. C. Roess, "X-Ray Scattering at Small Angles by Finely Divided Solids. I. General Approximate Theory and Applications," J. Applied Physics 18 (1947) 295.

3. L. C. Roess and C. G. Schull, "X-Ray Scattering at Small Angles by Finely Divided Solids. II Exact Theory for Random Distribution of Spheroidal Particles," J. Applied Physics 18 (1947) 308.

4. J. Riseman, Acta Crystallographica 5 (1952) 193.

5. J. H. Letcher and P. W. Schmidt, "Small Angle X-Ray Scattering Determination of Particle-Diameter Distributions in Polydisperse Suspension of Spherical Particles," J. Applied Physics 37 [2] (1966) 649-655.

6. O. L. Brill and P. W. Schmidt, "Small Angle Scattering Determination of Diameter Distributions," J. Applied Physics 39 [5] (1968) 2274-2281.

7. S. D. Harkness, R. W. Gould, and J. J. Hren, "A Critical Evaluation of X-Ray Small Angle Scattering Parameters by Transmission Electron Microscopy: GP Zones in Al Alloys," to be published in Phil. Mag. 1968.

8. R. Baur and V. Gerold, Acta Metallurgica 12 (1964) 1449.

9. R. W. Gould and S. R. Bates, "Determination of Particle Size Distribution in a Dispersion Hardened Nickel Alloy Using Small Angle X-Ray Scattering," to appear in 1968 Proceedings of the Denver X-Ray Conference.

10. S. D. Harkness and R. W. Gould, "A Study of G.P. Zone Growth Kinetics Through the Use of X-Ray Small Angle Scattering," to appear in 1968 Proceedings of the Denver X-Ray Conference.

11. W. S. Rothwell, "Small Angle X-Ray Scattering from Glassy Carbon," J. Applied Physics 39 [3] (1968) 1840-45.

12. R. Hosemann, and S. N. Bagchi, Direct Analysis of Diffraction by Matter. North Holland Publishing Co., Amsterdam, 1962.

13. C. A. Taylor and H. Lipson, Optical Transforms. Cornell University Press, New York, 1965.

14. B. D. Campbell and W. P. Ellis, "Laser Simulation of LEED Patterns," Surface Science 10 (1968) 724.

2. DETERMINATION OF PARTICLE SIZE DISTRIBUTION IN A DISPERSION HARDENED NICKEL ALLOY USING SMALL ANGLE X-RAY SCATTERING (R.W. Gould and S.R. Bates)

a. INTRODUCTION

An effective method for strengthening a ductile matrix is the inclusion of a finely dispersed second phase. Physical properties of such dispersion strengthened materials are strongly influenced by the particulate nature of the dispersant. Particle parameters such as size, shape, number fraction and distribution of particle sizes will influence the physical properties of the final products made from such alloys. Many of these particle paremeters are difficult to measure owing to the small size of most dispersants. A typical example may be found in dispersion strengthened nickel base alloys such as the "TD nickels." In this example, finely divided thoria (ThO_2) is incorporated into pure nickel or a nickel alloy. The thoria particles are generally less than 1000 angstroms in diameter, making it necessary to use transmission electron microscopy (TEM) to observe any direct particle-matrix interactions.

Particle size distribution measurements by TEM are time consuming and tedious; thus, in most cases only a few thousand particles will be measured. This paper will describe another technique for obtaining particle size distributions from dispersion strengthened alloys such as TD nickels. The technique to be described in this paper utilizes small angle scattering to determine the particle parameters.

b. THEORETICAL BACKGROUND

General small angle x-ray scattering, hereafter SAXS, theory has been discussed thoroughly in the literature[1,2]. In this section we will only present those SAXS equations that have particular bearing on the problem at hand. Letcher and Schmidt[3] have used an integral transform of the scattered

intensity to obtain particle size distribution of polydisperse spherical particles. Their method does not require assumptions about the form of the distribution function but is more difficult to apply than the method described in this paper. Harkness et al[4] have recently shown that in certain particulate systems it is possible to obtain the particle size distribution in a very simple manner using SAXS if one apriori assumes a size distribution function. Naturally the particle system must meet all the requirements for SAXS. Furthermore, the analysis has been carried out only for spherical particles having either a log normal or a normal distribution of particle diameters. In this section we will briefly discuss the theoretical background of this type of analysis.

Size Distribution and Small Angle X-ray Scattering

Harkness[4] has shown that a size distribution function, in this case log normal, could be written in terms of simple SAXS parameters. Equation (1) is the log normal size distribution function.

$$F(x) = \frac{1}{(\sqrt{2\pi})(x)(\ln \sigma)} \exp - \frac{1}{2} \left[\frac{\ln \mu - \ln x}{\ln \sigma} \right]^2 \qquad (1)$$

The geometric mean and the variance may be expressed as shown in Equation (2) in terms of a general moment equation for the log normal distribution function.

$$r^n = \exp \left[n \ln \mu + \frac{n^2}{2} \ln^2 \sigma \right] \qquad (2)$$

Baur and Gerold[5] showed that the Guinier radius, R_G, could be expressed by Equation (3) and the Porod radius, R^*, by Equation (4).

$$R_G = \left[\frac{<R^7>}{<R^5>} \right]^{1/2} \qquad (3)$$

$$R^* = \frac{\langle R^3 \rangle}{\langle R^2 \rangle} \tag{4}$$

These equations are simply ratios of moments of the particle size distribution function. Thus, if the size distribution function is assumed, these ratios may be easily calculated. When this is done for the log normal distribution, Equations (5) and (6) are obtained.

$$R^* = \exp(\ln \mu + 2.5 \ln^2 \sigma) \tag{5}$$

$$R_G = \exp(\ln \mu + 6 \ln^2 \sigma) \tag{6}$$

When Equations (5) and (6) are solved for   and   one obtains the following expressions.

$$\ln \mu = \ln R_G - 1.71 \ln \frac{R_G}{R^*} \tag{7}$$

$$\ln^2 \sigma = \frac{\ln \frac{R_G}{R^*}}{3.5} \tag{8}$$

This then gives the form of the size distribution curve in terms of the SAXS parameters alone, for if μ and σ are substituted into Equation (1), F(x) may be obtained for any x desired. This analysis has also been carried out for a normal distribution.

Small Angle X-ray Scattering Parameters

It is evident then that only two SAXS parameters are necessary to characterize the size distribution and these parameters may be obtained easily from line collimated SAXS data provided that the small angle camera is properly aligned. R_G is obtained using the familiar Guinier approximation for spherical particles, Equation (9), where ε is the scattering angle in radians.

$$I(\varepsilon) = n^2 \exp - \left(\frac{4\pi^2 R_G^2 \varepsilon^2}{5\lambda^2} \right) \tag{9}$$

Gerold[7] has shown that R^*, the so-called Porod radius, can be obtained from line collimated SAXS data if the "infinite" beam conditions are met. This relationship is given in Equation (10) where $s = \epsilon/\lambda$ is the modulus of s, the diffraction vector, and s_o is a value of s lying in the Porod region of the SAXS curve, i.e., where the slope of ln I(s) versus ln of s has a value three for

$$R^* = \frac{3}{8\pi (1 - f)} \frac{\int_0^\infty s\ I(s)\ ds}{s_o^3\ I(s_o)} \qquad (10)$$

In Equation (10) f is the volume fraction of scattering particles. The integral in Equation (10) is evaluated using a finite sum with an appropriate termination approximation[7,8].

c. EXPERIMENTAL RESULTS

Alloy Preparation

A sample of TD NiC (Ni-2.13 wt. % Cr-2.6 wt. % ThO_2) was kindly provided by Dr. B. A. Wilcox of the Metals Science Group at Battelle Memorial Institute, Columbus, Ohio. Dr. Wilcox[9] has studied the creep behavior of this alloy, and in the process, has measured the particle size distribution using TEM (see Figure 1). Other investigators[10] have measured the particle size distributions in basic TD nickel alloys containing no chromium. Some typical results on alloys of this latter type are shown in Figure 2. Unfortunately, alloys such as these were not available for this research.

The alloy used in this research was cold rolled to a thickness of 0.10 millimeters and stress relieved at 1000° C in vacuum for two hours. Prior to x-ray examination the sample was chemically thinned to a uniform thickness of 0.027 ± 0.003 millimeters.
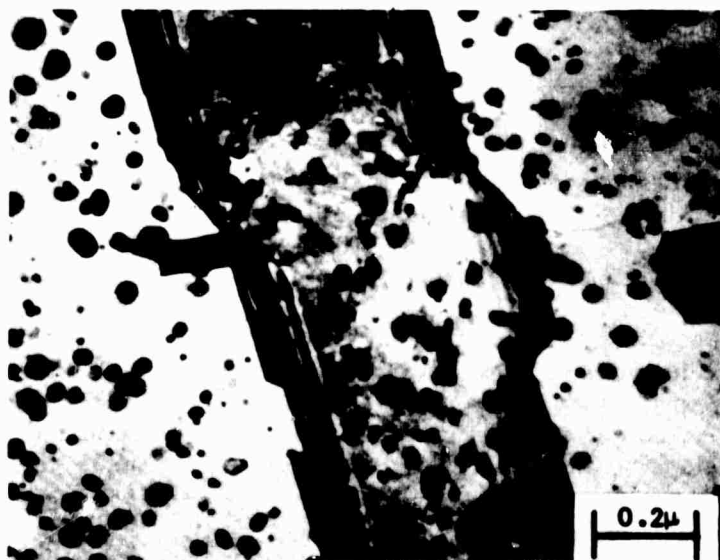
Figure 1. Transmission electron micrograph of Ni - 20 Cr - 2 ThO₂
used in this research, after Wilcox et al[9].
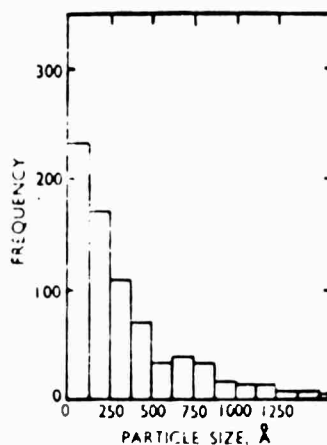
Figure 2. Particle size distribution of ThO₂ particles in a
dispersion hardened nickel alloy containing no
chromium, after Mee and Sinclair[10].

Small Angle X-Ray Scattering

A Kratky small angle scattering camera and a Kratky special anode copper tube was used in this research. The camera was carefully aligned to obtain the "infinite" beam condition using a special alignment device. Entrance slits of 100 microns appeared to give satisfactory resolution and scattering intensity. All measurements were made using balanced nickel-cobalt filters together with pulse height selection. Data was obtained by slow scanning (25 microns per minute) over the angular range of interest. The background intensity was measured using a pure nickel foil. The absorption ratio of the sample with respect to the nickel foil was taken into consideration in the data analysis. All data were analyzed using a simple computer program described elsewhere.[8]

Experimental Results

Table I presents the small angle scattering results of this investigation. The Guinier radius, R_G, and the Porod radius, R^*, were obtained using Equations (9) and (10), respectively. N_v was calculated from Equation (11) below, using Equation (2) to obtain a value for $<R^3>$. The volume fraction, f, of ThO_2 particles was 2.2% in the alloy used in this research.

$$\frac{4}{3} \pi <R^3> N_v = f \tag{11}$$

The parameters given in Table I have been used to obtain the quantities $\ln \mu$ and $\ln^2 \sigma$ by means of Equations (7) and (8). These values were then substituted into Equation (1) from which the particle size distribution curve (Figure 3) was established.

d. DISCUSSION

Wilcox[9] obtained a particle size distribution for the same alloy that was used in this research. The particle diameters that he measured by trans-

TABLE I

Small Angle X-ray Scattering Results from the

TD Ni-C Alloy Used in This Research

$$R_G = 110 \pm 10 \text{ Å}$$

$$R* = 60 \pm 5 \text{ Å}$$

$$N_v = 2.4 \times 10^{16} \text{ particles per cm}^3$$
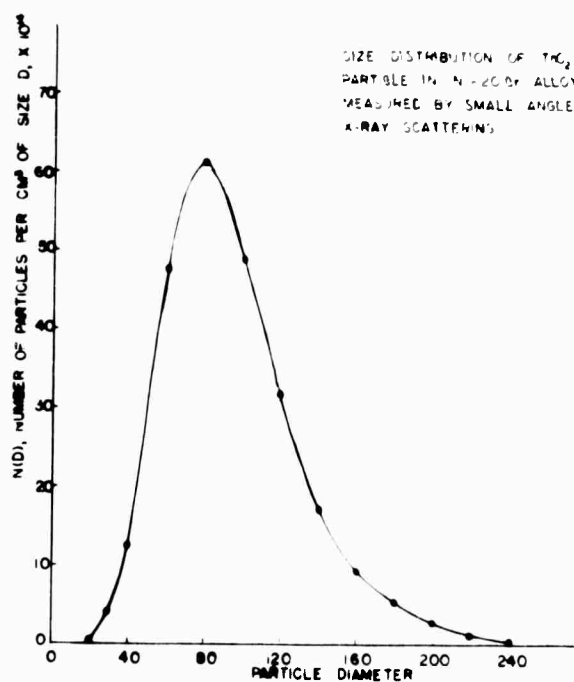
Figure 3. Size distribution of ThO$_2$ particles in TD NiC measured by small angle x-ray scattering.

mission microscopy ranged from 25 angstroms to 460 angstroms, with the average diameter being 145 angstroms. These data are not inconsistent with the results obtained in this study. As can be seen from Figure 3, the SAXS results give an average particle diameter of approximately 80 angstroms, with particle diameters ranging from 20 angstroms to 250 angstroms. These differences may have been the result of the resolution of the SAXS arrangement being too low to measure particles near the large end of the size distribution. Investigations are currently underway using a high resolution entrance slit arrangement on the Kratky camera. It is also evident that the position of the maximum in the size distribution curve determined by SAXS is very sensitive to R_G and to the ratio of R_G/R^*, as can be seen in Equation (7). In the present research, we did not obtain a long straight line portion in the $\ln I(\epsilon)$ versus ϵ^2 plot used to obtain the Guinier radius [see Equation (9)]. This occurs as a result of the particle size distribution and interparticle interference effects and will cause some uncertainty in the determination of R_G and, therefore, in the mean (μ) of the log normal distribution.

e. SUMMARY

The results of this research indicate that the small angle x-ray scattering method can be used to estimate the particle size distribution of thoria particles in dispersion strengthened nickel alloys if a particle size distribution function can be assumed. The method described is rapid and may be easily applied to other alloys of this type. Current investigations are underway on nickels containing no chromium.

REFERENCES

1. A. Guinier et al, <u>Small Angle Scattering of X-rays</u>, J. Wiley and Sons, New York, 1955.

2. V. Gerold, "Application of Small Angle X-ray Scattering to Problems in Physical Metallurgy and Metal Physics," in H. Brumberger, Editor, <u>Small Angle X-ray Scattering</u>, Gorden and Breach, New York, 1955, p. 277-317.

3. J. H. Letcher and P. W. Schmidt, "Small Angle X-ray Scattering Determination of Particle-Diameter Distributions in Poly disperse Suspensions of Spherical Particles," J. Applied Physics <u>37</u>; 649-655, 1966.

4. S. D. Harkness, R. W. Gould and J. J. Hren, "A Critical Evaluation of X-ray Small Angle Scattering Parameters by Transmission Electron Microscopy: GP Zones in Al Alloys," <u>Phil Mag</u>., 1968 (accepted for publication).

5. R. Baur and V. Gerold, "Vergleichende röntgengraphische und electronmikroskopische Untersuchungen der Grösse von Guinier-Preston-Zonen in Aluminium-Silber," Acta. Met. <u>12</u>; 1449-1453, 1964.

6. P. L. Bousquet, Masters Degree Thesis, Department of Metallurgical and Materials Engineering, University of Florida, 1968.

7. V. Gerold, "Die Zonenbildung in Aluminium-Zink Legierungen," Physica Status Solidi <u>1</u>; 37-49, 1961.

8. R. W. Gould and R. C. Sanwald, "A Computer Program for Simple Small Angle Scattering Calculations," Norelco Reporter <u>XIV</u>; 22-24, 1967.

9. B. A. Wilcox, A. H. Clauer and W. S. McCain, "Creep and Creep Fracture of a Ni-20Cr-2ThO$_2$ Alloy," Trans. AIME <u>239</u>; 1791-1795, 1967.

10. P. B. Mee and R. A. Sinclair, "Cold Rolling and Annealing Behavior in Nickel-Thoria Sheet, with Particular Reference to Preferred-Orientation Development," J. Inst. Metals <u>94</u>; 319-326, 1966.

B. ELECTRON MICROPROBE ANALYSIS OF PERMALLOY THIN FILMS (R. W. Gould and
    J. K. Watson)

The fundamental problem in the quantitative analysis of Permalloy thin
films resides in the thickness of the samples: they are too thin to utilize
the normal quantitative microprobe technique applicable to an "infinitely"
thick specimen.

There are few techniques described in the literature which are capable
of analyzing alloy thin films. Thick films (greater than 3,000 angstroms)
will often be analyzed using the infinitely thick approach if the alloy
linear coefficient is large enough. Ultra-thin films, less than 500 angstroms,
may be analyzed by the so-called infinitely thin sample technique (which
neglects absorption) if the take-off angle of the emergent x-rays is suffi-
ciently large. Unfortunately, the microprobe in the Department of Metallurgy
has an 18° take-off angle which necessitates films less than 200 to 300
angstroms if the infinitely thin sample method is to be used successfully.

A general "infinitely thin" technique for binary alloys of A and B
atoms has been developed and is described by Equation (1) given below.

$$I_A = K_A W_A (1 + K_F)(ABS)P_z \tag{1}$$

where, K_A =   the proportionality constant which contains factors such as
              crystal and detector efficiency, etc. Unless element A and
              element B are near neighbors on the periodic chart, K_A will
              vary markedly with different atoms.

W_A =   the weight fraction of element A

K_F =   the enhancement coefficient

P_z =   the atomic number correction factor where z equals the
            atomic number

ABS   =   the absorption factor for A radiation by the sample $[\exp(-\mu D)]$
          where μ equals a linear absorption coefficient of the sample
          for A radiation and D is the absorption path length.

For element B a similar expression is obtained

$$I_B = K_B W_B (1 + K_F)(ABS) P_z \qquad (2)$$

The absorption factor is generally the most troublesome when the infinitely thick approximation cannot be used. In order to calculate ABS, a composition and path length must be assumed. From Equations (1), (2) and (3), W_A and W_B could be calculated and these values inserted in the ABS factor.

$$W_A + W_B = 1 \qquad (3)$$

Iteration of this process should yield progressively better values of W_A and W_B. Unfortunately, the emergent path length of the x-rays cannot be known accurately unless the film thickness is determined with great accuracy. The approach being attempted by the x-ray group assumes that the ABS factor is nearly unity; i.e., the product μD is very small. Another assumption which is justified for elements of small δz, such as iron and nickel is that P_z is the same for both I_{Ni} and I_{Fe} and that $K_A = K_B$.

Since NiK radiation enhances FeK, K_F may be calculated for the assumed Permalloy composition as shown in Equation (4) below.

$$K_F = (0.6)(E_{FeNi}) \, W_{Ni} \, \frac{\mu_{FeNi}}{\mu_{Alloy}^{Ni}} \, \frac{(V - V_c^{Ni})^2}{(V - V_c^{Fe})^2} \qquad (4)$$

μ_{FeNi} = mass absorption coefficient of Fe for NiKα (400 cm^2/g).

μ_{Alloy}^{Ni} = the mass absorption coefficient of alloy for NiKα = radiation (128 cm^2/g).

$_c^{Ni}$ = critical excitation potential for nickel radiation in kilovolts

E_{FeNi} = excitation efficiency of iron by NiKα radiation = 0.213.

For the excitation voltage of 25 kv, K_F is

$$K_F]_{25 \text{ kv}} = (0.6)(0.213)(0.82)[3.20] \frac{(25 - 8.3)^2}{(25 - 7.1)^2} = 0.292 \qquad (5)$$

Combining Equations (1), (2) and (5) and imposing the simplifying assumptions discussed above, one obtains

$$\frac{I_{Fe}}{I_{Ni}} = \frac{W_{Fe}}{W_{Ni}} (1.292) \qquad (6)$$

which can be combined with Equation (3) to obtain the weight fraction of nickel.

$$W_{Ni}]_{25 \text{kv}} = \frac{1}{1 + (\frac{I_{Fe}}{I_{Ni}}) \, 0.774} \qquad (7)$$

Table I presents some calculated nickel compositions using Equation (7) for a Permalloy thin film whose thickness was not known accurately but believed to be approximately 1,000 angstroms.

TABLE I

I_{Nickel}	I_{Iron}	I_{Iron}/I_{Nickel}	Weight % Nickel
651	108	0.166	88.6
642	110	0.171	88.3
647	109	0.168	88.4
658	110	0.167	88.6
662	111	0.168	88.4

The values of Table I are considerably higher than the expected value of 82% nickel; thus the assumption of the infinite thickness is probably not justified for this film. Work is currently in progress utilizing very thin (less than

300 angstroms) films which have been removed from the glass substrate and placed on a wire mesh holder. This latter step removes the uncertainty caused by substrate electron back scatter with its resulting increased x-ray excitation.

C. FACILITIES FOR PERMALLOY THIN FILM FABRICATION AND EVALUATION
(J. K. Watson)

During the past six months we have established facilities for the routine vacuum deposition of planar permalloy thin films and for the measurement with fair accuracy of thickness, coercive force H_c, and anisotropy field H_k. A previously-developed pulsed-field system has been adapted to the measurement of dispersion. Magnetic domains can now be observed routinely using the Kerr magnet-optical effect.

The vacuum deposition process, dispersion measurements, and preliminary observations of magnetic domains are each discussed briefly below. Metallurgical measurements of alloys composition are discussed by Dr. Gould elsewhere in this report.

1. VACUUM DEPOSITION PROCESS

Film fabrication is by vapor deposition in vacuum from an alloy which is heated by induction from a 5-kw Lepel RF generator. A Sloan OMNI crystal oscillator provides both thickness and deposition rate information, with capability for automatic control of these parameters in the future. We usually deposit films at the rate of 25 angstroms per second, with our present source configuration, Figure 1, and with the RF generator at about 2/3 of maximum plate current. Thus, there is a reasonable margin for varying the deposition rate. The source is nominally 5 grams and the source-substrate distance is 13 inches. The 1-cm diameter films are deposited through a mask onto 5/8 inch square substrates of Corning 7059 pyrex of .030 inch thickness. Substrate temperature is controlled (by a Barber Colman 471-P) using a standard 500 watt quartzline lamp as the heating element for the OFHC copper heat sink which backs the substrates.

Molten permalloy

Nested crucibles
(99. 7% Al_2O_3)

Crucible holder
[Machined from Grade A Aluminum
Silicate (Lava)]

Water-cooled
OFHC copper work-coil
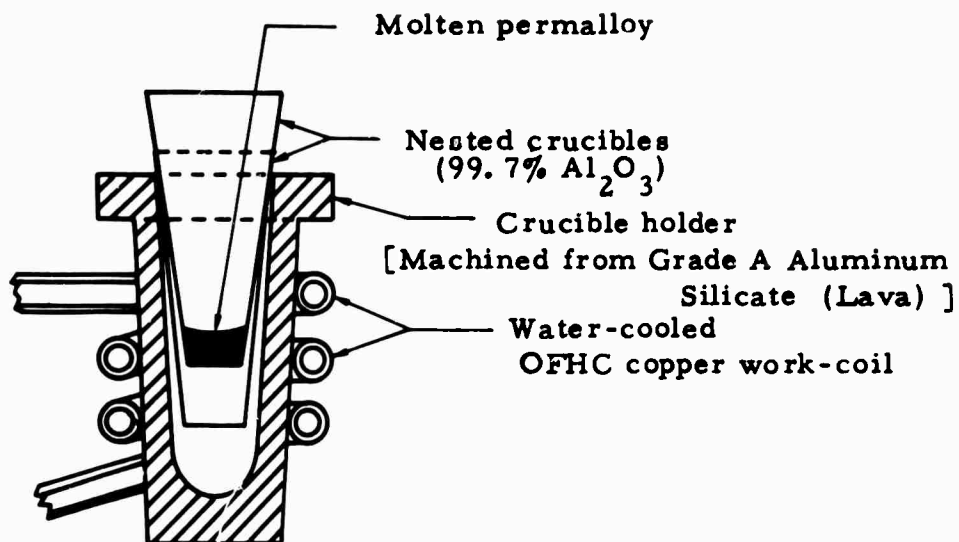
Figure #1

Source Configuration for Vacuum Deposition

Several problems with this system still prevent its operation as origi-

nally intended. First, the background pressure in the system rises by 2 to 3

orders of magnitude during deposition, such that the purity of the films is

degraded by capture of an estimated 1 to 2 atomic percent of residual gas

during deposition. Although this is not an unreasonable level of contamination,

we seek an order of magnitude improvement, by the addition of a Meissner trap and by improving outgassing and deposition techniques. Two tougher problems are concerned with the melt confinement: first, the crucible usually breaks after only one deposition; and second, a thin layer of contaminant sometimes forms over the surface of the melt, causing inconsistent evaporation. Breakage has been reduced by changing the crucible support to reduce the thermal gradients during deposition, and seems to be further reduced by a slow heat-up to the evaporation temperature. Since the surface contaminant does not always form over the melt, it is thought to be affected by the smoothness of the crucible inner surface.

The surface contaminant now seems to be under control, by prior outgassing of crucible at 1500°C, followed by the addition of 0.1 percent gadolinium to the permalloy melt.

Further plans call for the continuing evaluation of other crucible materials, and for the exploration of the feasibility of using a levitation work coil. These developments are expected to move gradually, as we are able to make more sophisticated characterizations of film performance parameters.

2. DISPERSION

We have identified dispersion (of the easy axis of magnetization) as a key parameter for systematic investigation. Together with skew, film dispersion is the parameter which determines the minimum required reset bit-current in a film memory application. At high values, gross dispersion has been found to be affected by annealing procedures, alloy composition, and film thickness. It is difficult to achieve consistent low values of dispersion, thus it is a sensitive parameter of the process variables. We have made an arbitrary definition of six categories of dispersion in a geometric progression ranging from "very low" (less than 0.6°) to "very high" (greater than 9.2°) plus two

-122-

additional categories for peculiarities.

Some investigators have found a thickness dependence of dispersion, attributed to a magnetization buckling caused by the demagnetizing field. It is too early for our investigation to be conclusive but our approach is:

In the ill-understood range of moderate to very low dispersion, we attribute dispersion to several effects which can be identified initially by "thickness dependence" and "other". By hypothesis, for any thickness there is a minimum value of dispersion, as suggested in Figure 2 we are attempting to experimentally identify the components of dispersion, and to establish their meaning theoretically.

3. DOMAIN OBSERVATION BY KERR EFFECT

Earlier investigations have suggested that a simple dispersion measurement is inadequate as a statistical film description. We have initiated a companion study of magnetic domain configurations as a way of gaining additional insight into the influence of micromagnetic structure. It is found that residual domain configurations depend not only on the film properties but also on the procedure for demagnetizing the film. For a given domain pattern, we seek an identification of its key attributes, and to identify those attributes with demagnetizing procedures and/or appropriate parameters of film properties.

Demagnetization of the film by a slowly-decaying a-c magnetic field has been found to cause strikingly different domain patterns, as a function of the angle of the applied field relative to the film easy-axis. Typical patterns are shown in Figure 3 for easy-axis and hard-axis demagnetization, where far fewer domains are found for the easy-axis case. Preliminary observations indicate an increase in domain density with film thickness, with surprisingly little correlation with film dispersion. For high dispersion films, the optimum polarizer/analyzer orientation for best domain contrast is found to vary over the surface of the film. For an occasional film, the domain edges are not straight as in Figure 3 but are curved, due to local skew.

Figure. 2 Preliminary Measurements of Magnetic Film Dispersion vs Thickness
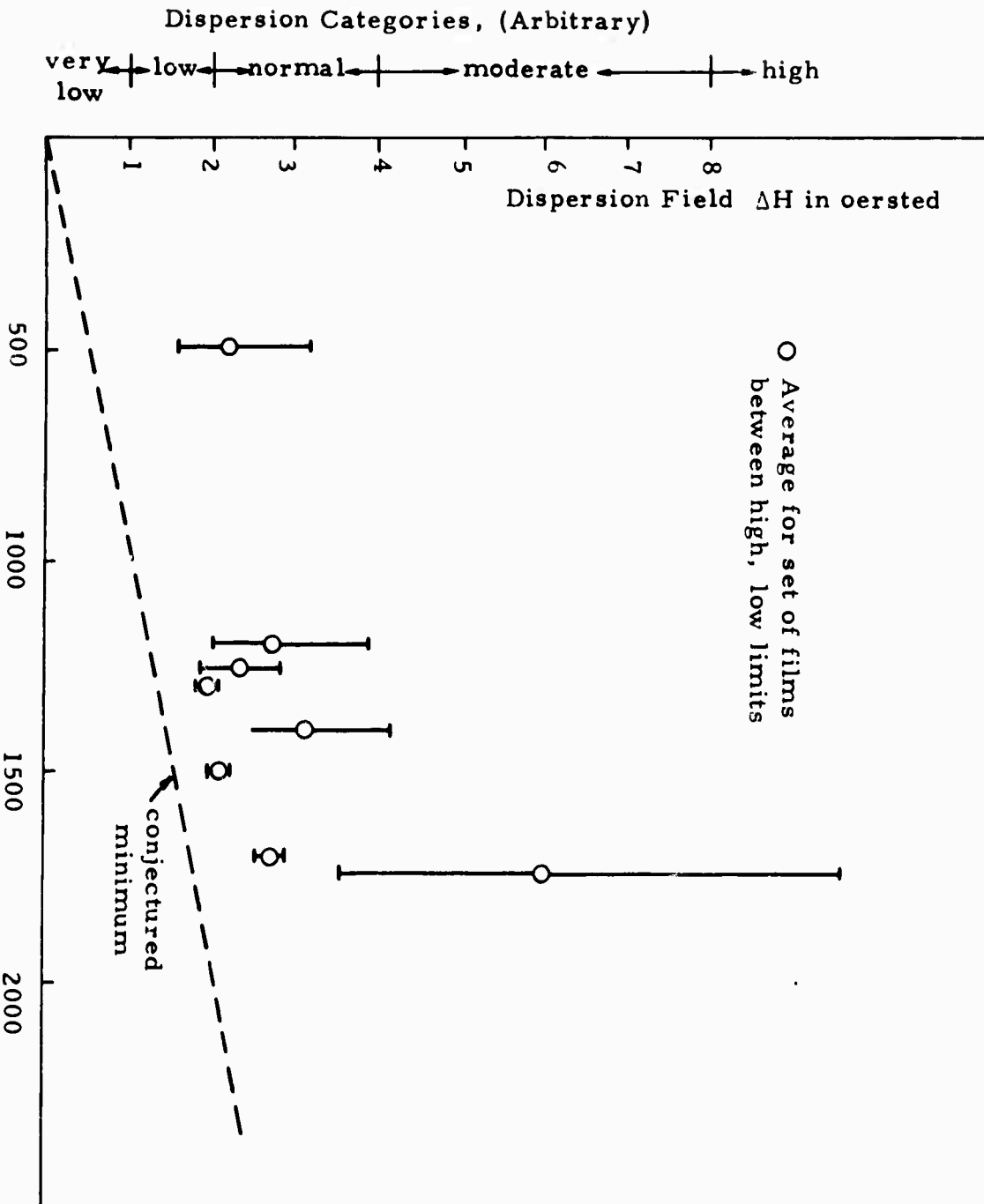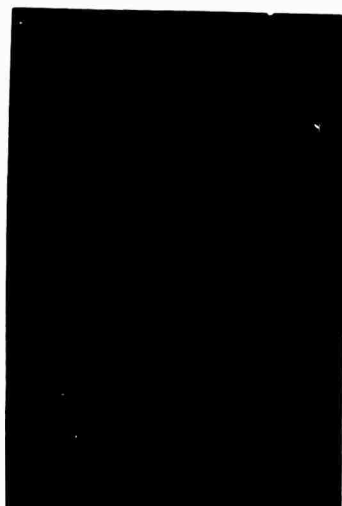
a) AFTER EASY-AXIS DEMAGNETIZATION
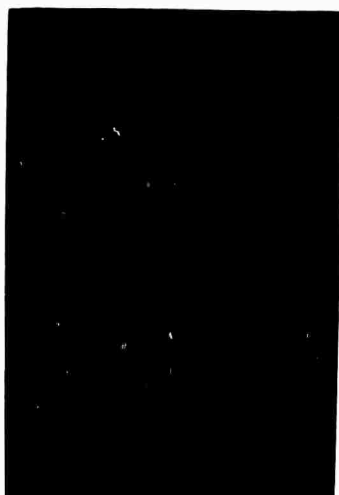
b) AFTER HARD-AXIS DEMAGNETIZATION

FIG. 3 TYPICAL DOMAINS IN A MAGNETIC FILM AFTER A-C
DEMAGNETIZATION

Demagnetization of the films by a hard-axis pulse requires precise film alignment and excellent homogeneity of the field, yet causes domain configurations which are not only difficult to interpret but are apparently dependent on the derivatives of the pulsed field. We have not yet seriously considered these problems.

In summary, we have established a facility for creating and observing domain configurations in magnetic films. A simple procedure of a-c demagnetization has helped identify some inhomogeneous films with easy-axis skew. We are attempting to establish a more quantitative interpretation of observations on typical films.

D. AN ANALYSIS OF THICKNESS ERROR IN QUANTITATIVE TRANSMISSION MICROSCOPY OF CERAMICS (C.V. Gokularathnam, S.W. Freiman, R.T. DeHoff and L.L. Hench)

1. INTRODUCTION

Optical microscopy has been a fundamental tool in the identification of crystals for over a century, and electron microscopy has been essential for analysis of structural defects for nearly two decades. However, only since the development of quantitative stereology in recent years has it been possible to quantitatively analyze structural features such as volume fraction, surface area of phases, number of particles per unit volume, etc. from microscopic measurements. It is well recognized that accurate quantitative analysis of defects and phase assemblages is essential if correlations between structure and properties are to be developed. It has been shown that the counting measurements and mathematical analysis necessary for quantitative structural determinations are relatively simple and straightforward as long as the microscopy is conducted on a sample illuminated in reflection.[1] The surface of the sample in such illumination is a planar section of the microstructure and corresponds to the model employed in deriving the fundamental stereological parameters, P_P, N_L, and N_A. (The definitions of the stereology terms and their methods of measurement are reviewed in the appendix.)

However, in many microscopic analyses, it is necessary to employ transmitted illumination. For example, electron microscopy is limited to transmission measurements when particles or defects are less than 100 Å in size. The optical transparency of many ceramic crystals, glasses and multiphase bodies makes transmission microscopy of thin sections necessary.

The problem that arises in transmission microscopy is that the thickness of the sample must be taken into account in order for quantitative evaluations of structure to be valid. When the sample thickness to particle diameter ratio (t/b) is greater than about 2, a considerable error can be introduced if the effect of thickness is neglected. It is the objective of the present

paper to examine the magnitude of error resulting from thickness effects when the t/b ratio is in the range of 2. In many electron or optical microscopy studies it is possible to achieve a t/b ratio of 20 or more and in these cases, the potential thickness error is even greater than that herein reported.

An additional objective of the present paper is to demonstrate that complete stereological treatment of the transmission microscopic analysis does yield calculated values comparable to the experimental values obtained from reflection measurements on the same samples.

The system employed in this study was a partially devitrified $Li_2O-2SiO_2$ glass which could be examined in both reflection and transmission over a range of volume fractions of crystals. These petrographic studies could also be compared with the detailed x-ray analysis previously reported on the same samples.[2]

2. THEORY

In reflection microscopy, there exist three fundamental stereological relationships that permit the estimation of geometric properties of a three-dimensional structure from simple counting measurements made upon a random plane section:[1]

$$P_P = V_V \tag{1}$$

(I)
$$N_L = \frac{1}{2} S_V \tag{2}$$

$$N_A = N_V \overline{D_V} \tag{3}$$

The quantities on the left of these equations are the counting measurements, which are performed under the microscope, or on photomicrographs; they are fully explained in the Appendix. The quantities on the right are properties of the structure which may be estimated from these measurements. V_V is the

-128-

volume fraction of the phase of interest in the sample. S_V is the total area of interface between the matrix and the phase of interest, in unit volume of sample. N_V is the number of particles in unit volume, and $\overline{D_V}$ their average size (caliper diameter). These relationships are valid for structures of arbitrary geometry, i.e., for aggregates of particles of arbitrary shape and size distribution.

When a sample is observed in transmission microscopy, the image contains a projection of all of the structure contained within the volume of the thin section under study. Particles that intersect the top and bottom surface of the section contribute to the projected image in proportions that are essentially equal to those that would be observed in reflection microscopy. Two additional kinds of contributions to the projected image must also be accounted for; these alter and complicate the relationships between the counting measurements and the properties of the three-dimensional structure in the thin section.

Particles whose centers lie within the volume of the section contribute projected images which must be added to those that result from particles that intersect the surfaces of the section. The equations in set (I) become:[1,3]

$$P_P' = V_V + N_V t \overline{A}_{proj} \tag{4}$$

(II)
$$N_L' = \frac{1}{2} S_V + \frac{2}{\pi} N_V t \overline{L}_{proj} \tag{5}$$

$$N_A' = N_V \overline{D_V} + N_V t \tag{6}$$

where P_P', N_L', and N_A' are the values of the counting measurements described in the Appendix measured in transmission microscopy, $\overline{A}_{proj}$ is the average projected area of particles in the structure, $\overline{L}_{proj}$ is the average perimeter of the projections of all particles in the structure, and t is the section thickness. Thus, if the equations in set (I) are used to estimate properties of the

structure, the values of these properties will tend to be <u>overestimated</u> by amounts corresponding to the second term in each of these equations.

If the section thickness is large compared to the particle size, the projections of some particles will be partially or wholly obscured by the projections of other particles in the system. This effect of particle overlap, called the Holmes Effect,[3-4] will tend to yield an underestimate of the geometric parameters of the structure. The Holmes effect increases as the section size increases, and as the volume fraction of the second phase increases. The Holmes effect has been neglected in the present study, because both the volume fraction and section thickness are small.

If it is assumed that all of the particles in the structure are the same size and shape, the geometric properties of the structure may be written in terms of the particle size, b, and shape factors:

$$\overline{D_V} = k_1 b \tag{7}$$

$$S_V = N_V S = N_V k_2 b^2 \tag{8}$$

(III)
$$V_V = N_V V = N_V k_3 b^3 \tag{9}$$

$$\overline{L}_{proj} = k_4 b \tag{10}$$

$$\overline{A}_{proj} = k_5 b^2 \tag{11}$$

where the constants, k_1, k_2, k_3, k_4, and k_5 are shape factors which must be evaluated for given particle shape and choice of size parameter. Further, it can be shown, that for convex particle shapes,

$$k_4 = \pi k_1 \tag{12}$$

$$k_5 = \frac{1}{4} k_2 \tag{13}$$

-130-

Substitution of these results into equations (II) gives:

$$P_P' = N_V b^2 [k_3 b + \frac{1}{4} k_2 t] \tag{14}$$

$$(IV) \qquad N_L' = N_V b [\frac{1}{2} k_2 b + 2k_1 t] \tag{15}$$

$$N_A' = N_V [k_1 b + t] \tag{16}$$

The experimental determination of the three counting measurements on the projected image, coupled with the evaluation of the three shape factors, thus yields three simultaneous equations which may be solved for the three unknowns, N_V, b, and t. The insertion of the number of particles and their size into equations (8) and (9) then yields a complete description of the structure in terms of its extensive geometric properties: volume, surface area, number, and size of particles. In practice, it is necessary to obtain an independent measurement of sample thickness (t) in order to solve the equations in Set IV with accuracy.

3. EXPERIMENTAL PROCEDURE

The partially crystalline $Li_2O-2SiO_2$ glass used in this experiment was prepared according to the procedure outlined by Freiman and Hench.[2] The heat treatment shcedule consisted of a 3 hr nucleation treatment at 475°C followed by a crystallization treatment of 1 minute at 595°C for sample 1, 15 minutes at 592°C for sample 2, and 140 minutes at 555°C for sample 3. A petrographic thin section, 20 ± 5 microns thick, was prepared from each sample. The remainder of each sample was retained for use in the reflection studies.

The thin sections were studied in transmission in a Bausch and Lomb model LI dynoptic polarizing microscope. Due to the birefringence of the devitrified phase, the $Li_2Si_2O_5$ crystals appeared light against a dark background when the section was viewed under crossed nicols. A typical microstructure is shown in Figure 1.

The quantitative stereological parameters, P_P', N_L' and N_A', were measured in transmission by placing an 8 x 8 grid in the eyepiece of the microscope. Twenty-five measurements of each parameter were made on each section. and their average was calculated. At any given position of the microscope stage, a constant fraction of $Li_2Si_2O_5$ crystals was invisible under crossed nicols because of partial extinction. The quantitatve measurements were corrected for this effect by multiplying the calculated average values of P_P', N_L' and N_A' by a factor which accounted for the invisible fraction of the particles. By measuring the angular extinction of 100 particles this factor was determined to be 1.2

Specimens were prepared for measurements in reflection by polishing through 0.3 micron alumina grit, and etching for 10 minutes in 2.5% HF.[5] A typical microstructure after such a treatment is shown in Figure 2. An average of the twenty-five measurements of P_P, N_L and N_A made in a Bausch and Lomb Research Metallograph was calculated. The thickness of each thin section was also measured in the metallograph. A typical cross-sectional view of a thin section is shown in Figure 3.

The evaluation of the average particle size and number of particles in the system requires a determination of the three shape factors, k_1, k_2, and k_2. This requires an assumption or determination of the shape of the particles involved. Examination of the microstructure of the system under study suggested that the particles could be modeled as ellipsoids of revolution. The shape of particles is specified in terms of the axial ratio, q, of the generating ellipse, where q is the ratio of the minor to major axis (b/a). Values of the three shape factors have been calculated as a function of q,[6] and are plotted in Figure 4.

It has been shown that the average axial ratio of sections through ellipsoids, $\overline{F}$, is related to the value of q for the structure;[7] this relationship

is plotted in Figure 5. The value of $\bar{F}$ was determined for each sample by measuring the axial ratio of 100 particle sections chosen at random. The axial ratio of the three-dimensional particles, q, was then determined from Figure 5, and the corresponding shape factors read from Figure 4.

4. RESULTS

The results of the present investigation are summarized in Tables I and II. In Table I the values of the parameters measured in transmission are given in the first column for each sample, the calculated reflection values in the second column, and the values measured in reflection in the third column. The fourth column lists the "thickness error", the error which would be encountered if the values measured in transmission were not corrected for the thickness of the thin section. The last column gives the error after correction, the difference between the calculated values and the values measured in reflection.

The "correction error" can be attributed to a number of causes. There was approximately 4% error in determining P_P, N_L and N_A, resulting from human subjectivity in counting and from reproducing counting measurements. There was probably some error due to the Holmes effect, especially for the sample of higher volume fraction. Rather than the particle size being constant, as assumed in the theoretical analysis, there was approximately a 3% dispersion in particle size, producing an error in the transmission correction factor. Finally, there appeared to be a small variation in section thickness which will influence transmission values.

Table II summarizes the complete microscopic analysis of the devitrified glass samples measured in transmission and corrected for thickness effects.

The volume fraction of lithium disilicate spherulites, the number of spherulites per unit volume, spherulite size, the surface area of the spherulites,

Figure 5. The average axial ratio of cells through prolate ellipsoids as a function of the axial ratio of the generating ellipse.

Figure 4. Various shape factors used for estimating the number and size of ellipsoidal particles from the counting measurements; q is the ratio of the minor to major axis of the generating ellipse.

TABLE I

SUMMARY OF THICKNESS ERROR ANALYSIS

$$\text{Thickness Error} = \frac{\text{Transmission} - (\text{Reflection})_{cal}}{(\text{Reflection})_{cal}}$$

$$\text{Correction Error} = \frac{(\text{Reflection})_{cal} - (\text{Reflection})_{meas}}{(\text{Reflection})_{meas}}$$

Sample Number	Trans-mission	Reflection Calculated	Reflection Measured	Thickness Error %	Correction Error %
P_P					
1	0.090	0.023	0.020	291	15.0
2	0.106	0.025	0.029	324	14.0
3	0.213	0.045	0.053	373	15.1
N_L					
1	177	103	107	71	3
2	154	86	85	79	1
3	232	135	106	72	27
N_A					
1	9.3×10^4	5.0×10^4	4.8×10^4	66	4
2	7.0×10^4	4.1×10^4	4.1×10^4	71	0
3	8.2×10^4	3.4×10^4	4.6×10^4	141	26

TABLE II

SUMMARY OF PARTICLE PARAMETER ANALYSIS

Sample Number	Section Thickness	Volume Fraction V_V	Number Particles per Unit Volume N_V	Average Particle Size $\underline{b}$	Surface Area of Particles/ Unit Volume S_V	Average Distance Between Particles λ
1	9.9 µ	0.023	5.3×10^7/cc	7.5 µ	207 cm^2/cc	188 µ
2	12.2 µ	0.025	3.2×10^7/cc	9.2 µ	172 cm^2/cc	227 µ
3	20.4 µ	0.045	2.5×10^7/cc	12.8 µ	270 cm^2/cc	141 µ

and the average distance between the particles is presented for three samples.
The average distance between particles is obtained in the relation $\lambda = 2[1-\bar{P}_p]/\bar{N}_L$.
It can be seen that although the same volume fraction of crystals can always
be obtained from different heat treatment schedules, the other structural
parameters may vary depending on nucleation treatments employed, differences
in glass composition, experimental scatter or other factors.

5. DISCUSSION OF RESULTS

It is clear from Table I that the quantitative stereological parameters
measured from transmission specimens differ considerably from the true
parameters. This is demonstrated by the magnitude of the "thickness error".
The measured and calculated reflection values agree very closely, however,
justifying the assumptions made in the analysis regarding particle size and
shape. Comparison of the values of V_V determined in this study with those
expected from the crystallization kinetics determined by Freiman and Hench[2]
from x-ray diffraction data also confirms the accuracy of the present analysis.

Examination of Table II reveals that more insight into the behavior of
the devitrified glass samples is possible when all the structural parameters
are known than when volume fraction alone is measured. For example, Hasselman
and Fulrath[8] have shown the strength of glasses containing second phase
oxide particles is dependent on the mean free path between particles. Two
of the authors have recently demonstrated the same dependence for partially
devitrified glasses.[9] The porosity dependence of strength of polycrystalline
ceramics is also probably related to the mean free path between pores. As
shown in Table II, measurement of average mean free path between particles
can be determined analytically rather than assumed from volume fraction
measurements.

Surface area per volume is another parameter which can be determined analytically and is often overlooked in the evaluation of the behavior or processing of ceramics. DeHoff and Rhines have recently shown that the sequence of geometric changes occurring in the densification of a sinterbody are directly related to the change in surface area of the porosity.[10] Surface area analysis is also important in the analysis of catlysis, permeability, and sorption-desorption processes.

Quantitative measurements of particle size and number of particles per unit volume are particularly useful in evaluating process variables. Pore and particle size distributions that result from density gradients in forming, or temperature gradients in firing, can be determined from fired ware in this manner.

6. CONCLUSIONS

The results of this investigation show that quantitative stereological parameters can be overestimated by as much as 300% when measured in transmission if corrections for thickness effects are not made. It has also been shown that structural parameters corrected for thickness effects correspond with values obtained from reflection measurements and x-ray analysis within about 10%. Consequently, it is possible to obtain quantitative correlations of physical properties and process variables with ceramic microstructures from either reflection or transmission microscopy if the aoove analysis is followed.

References

1. R. T. DeHoff, "Quantitative Microstructural Analysis", <u>Fifty Years of Progress in Metallographic Techniques</u>, ASTM STP 430, American Society for Testing and Materials (1968) pp 63-95.

2. S. W. Freiman and L. L. Hench, "The Kinetics of Crystallization In Li_2O-SiO_2 Glasses", <u>Journal of the American Ceramic Society</u>, <u>51</u> (1968) 7.

3. J. E. Hilliard, "The counting and sizing of particles in transmission microscopy", <u>Trans. Met. Soc. AIME</u>, <u>224</u> (1962) 906.

4. A. N. Holmes, <u>Petrographic Methods and Calculations</u>, Murphy and Co., London (1927).

5. Werner Vogel and Hans-Günter Byhan, "Zur Struktur binäter Lithiumsilikikat-gläser II. Das Lösungsverhalten in verdünnter Flussäure", <u>Sikikattechnik</u>, 15 [8] (1964) 239-244.

6. R. T. DeHoff, "The Determination of the Geometric Properties of Aggregates of Constant-Size Particles from Counting Measurements Made on Random Plane Sections", <u>Trans. Met. Soc. AIME</u>, <u>230</u> (1964) 764.

7. R. T. DeHoff and F. N. Rhines, "Determination of Number of Particles per Unit Volume from Measurements made on Random Plane Sections: The General Cylinder and the Ellipsoid", <u>Trans. AIME</u>, <u>221</u> (1961) 975.

8. D. P. H. Hasselman and R. M. Fulrath, "Proposed Fracture Theory of a Dispersion Strengthened Glass Matrix", <u>Journal of the American Ceramic Society</u>, <u>49</u> [2] (1966) 68-72.

9. S. W. Freiman and L. L. Hench, "Mechanical Behavior of Partially Devitrified Lithia-Silica Glasses", to be published.

10. R. T. DeHoff, R. A. Rummel, H. P. LaBuff and F. N. Rhines, <u>Modern Developments in Powder Metallurgy</u>, Vol. 1, Plenum Press, New York (1966) p 310.

APPENDIX

NOMENCLATURE AND DEFINITIONS OF QUANTITIES MEASURED IN THE MICROSTRUCTURE

1. The point fraction, P_P (Figure A1). A grid is superimposed on the structure and the number of points lying within the phase of interest is counted. P_P is this number divided by the total number of points in the grid.

2. The number of intersections per unit length of test line, N_L (Figure A2). A test line is superimposed on the structure. The number of times this line intersects particle outline, divided by the total length of test line on which measurements are made is the intercept count, N_L.

3. The particle count, N_A (Figure A3). This parameter is defined as the total number of particles observed in the structure, divided by the area of observation. Particles intersecting the edge of the area of observation are counted as 1/2 particle.
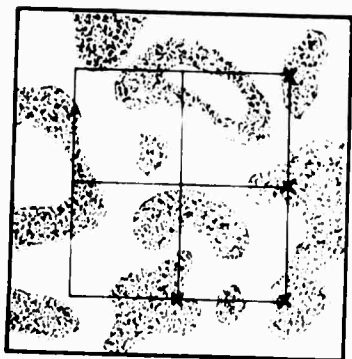
$$P_P = \frac{4}{9}$$

A1

$$N_L = \frac{8}{L}$$

A2

AREA = A

$$N_A = \frac{9+5/2}{A} = \frac{11.5}{A}$$

A3

Figures A1, A2 and A3. Illustration of the method of measurement of N_L, and N_A.

IV. Semiconductors and Semiconductor Devices (F. A. Lindholm, S. S. Li,
A. J. Brodersen, E. R. Chenette, J. Salz, R. W. Gould, J. J. Hren,
L. L. Hench, C. T. Sah)

A. THE DENSITY OF STATES IN DEGENERATE N-TYPE GERMANIUM AND SILICON
(S. S. Li and J. Agraz-G)

In a nondegenerate semiconductor, the conventional expression for the
density of states in the conduction band is given by:

$$g_o(E) = \frac{4\pi(2M^*_d)^{3/2}}{h^3} (E - E_c)^{1/2} \qquad [1]$$

Equation [1] predicts a zero density of states at the edge of conduction band
(i.e., at $E = E_c$). However, as a result of the interaction of conduction elec-
trons with donor impurities, the density of states in a heavily-doped semi-
conductor does not become zero at the bottom of the conduction band: the
region of permitted energies is shifted downward. Sharp band edges disappear
and a tail in the density of states, extending directly into the forbidden
gap, appears.

Recent experiments on tunneling (1), optical absorption (2), and lumi-
nescence (3) have yielded experimental evidence for a "tail" in the density
of states associated with impurities in degenerate semiconductors. In addition,
a considerable amount of theoretical work has been done in determining the
effect of a high density of impurities on the density of states (4). None of
these theories has been used extensively to the study of the effects of doping
on the density of states in either germanium or silicon.

The present work deals with theoretical estimates of the density of states
as a function of impurity concentrations for degenerate n-type silicon and
germanium. The study of Halperin and Lax (H-L)[4] gives the density of states
deep in the forbidden gap and the results of Bonch-Bruyevich (B-B)[5] gives
the density of states continuously for energies slightly below and above the
conduction band edge (i.e. $E > E_c$) and approaches asymptotically the parabolic

approximation (see Eqn. [1]) for energies exceeding the Fermi level.

The H-L (4) approach predicts the density of states deep inside the forbidden gap as given below:

$$g(E) = [(Q\ E_Q)^3/\zeta^2]\ a(\nu)\ \exp\ [-E_Q^2\ b(\nu)/2\zeta] \qquad [2]$$

where

$$\zeta = \frac{2\pi}{Q}\ \frac{e^4}{\varepsilon^2}\ N_I;\ \frac{1}{Q}$$ is the screening length, N_I is the impurity concentration. ε denotes dielectric constant.

$$E_Q = \frac{\hbar^2 Q^2}{2M^*}\ ;$$ $$M^* = 3(\frac{1}{M_\ell} + \frac{2}{M_t})^{-1}$$ is the electron effective mass.

$$Q^2 = [4M_d^*\ e^2/\varepsilon\hbar^2]\ (3N_I/\pi)^{1/3},\ M_d^*$$ is the density of states effective mass.

$$\nu = (E_o - E)/E_Q$$ is the energy below mean potential E_o in units of E_Q, $$E_o = -\frac{4\pi e^2\ N_I}{\varepsilon Q^2}$$

$a(\nu)$ and $b(\nu)$ are given in reference (4).

We have made use of Equation [2] to estimate the density of states deep in the forbidden gap for degenerate N-type Germanium and Silicon for different doping concentrations. The results are displayed in Fig. 1 and Fig. 2.

For energies slightly below and above the conduction band edge, the density of states $g(E)$ is given by B - B (5):

$$g(E) = \frac{(2M_d^*\ E)^{3/2}}{16\pi^{3/2}\ a\hbar^3}\ \exp(-x)\ [I_{1/4}(x) + I_{-1/4}(x) + I_{3/4}(x) + I_{-3/4}(x)] \qquad [3]$$

where

$$a^2 = \frac{\pi e^4}{\varepsilon^2 Q}\ \cdot\ N_I,\ \text{and}\ x = \frac{E^2}{8a^2}$$

The $I_r(x)$ are Bessel functions with imaginary arguments.

In the energy region $E = E_F$ (Fermi level), Equation [3] reduces to:

$$g(E) = g_o(E) \left(1 - \frac{a^2}{E^2}\right) \qquad [4]$$

Near the bottom of the conduction band (i.e. $|E| \doteq 0$), the density of states changes radically. In this region, Equation [3] reduces to:

$$g(E) = g_o(E) \sqrt{\frac{\pi a}{E}} \frac{1}{\Gamma(\frac{1}{4})} \left[1 + \frac{\Gamma(\frac{1}{4})}{4\Gamma(\frac{3}{4})} \cdot \frac{E}{a} \right] \qquad [5]$$

where $\Gamma(r)$ denotes the Gamma function.

Equations [2], [4] and [5] provide a direct means for displaying the density of states $g(E)$ as a function of energy E for arbitrary impurity concentrations. Fig. 1 and Fig. 2 demonstrate $g(E)$ versus E for N-type germanium and silicon with donor concentrations varying from 10^{19} to $10^{21} cm^{-3}$. Note that in the intermediate region where the two approaches (i.e. H-L and B-B approaches) fail, certain approximations have been made to smooth out the $g(E)$ curves.

Fig. 1 shows that in an N-type germanium with $10^{19} cm^{-3}$ donor impurities, the band edge shifted downward by 0.022 ev from the unperturbed conduction band edge; the density of states in the tail decreases rapidly with depth into the forbidden bands (faster than exponentially). As a result of screening, the number of states in the forbidden band turn out to be small compared with the number of states inside the conduction band. Shepherd et al (1) have observed an exponential band edge in degenerate N-type germanium doping of $1.2 \times 10^{19} cm^{-3}$ Sb. This gives reasonable agreement with the present results.

Deep in the conduction band (in particular, near the Fermi-level of N-type uncompensated semiconductors), the density of states in degenerate semiconductors differs only slightly from the conventional parabolic approximations (See Fig. 1 and Fig. 2).

-144-

Fig. 1

N-type Germanium

Fig. 2

N-type Silicon
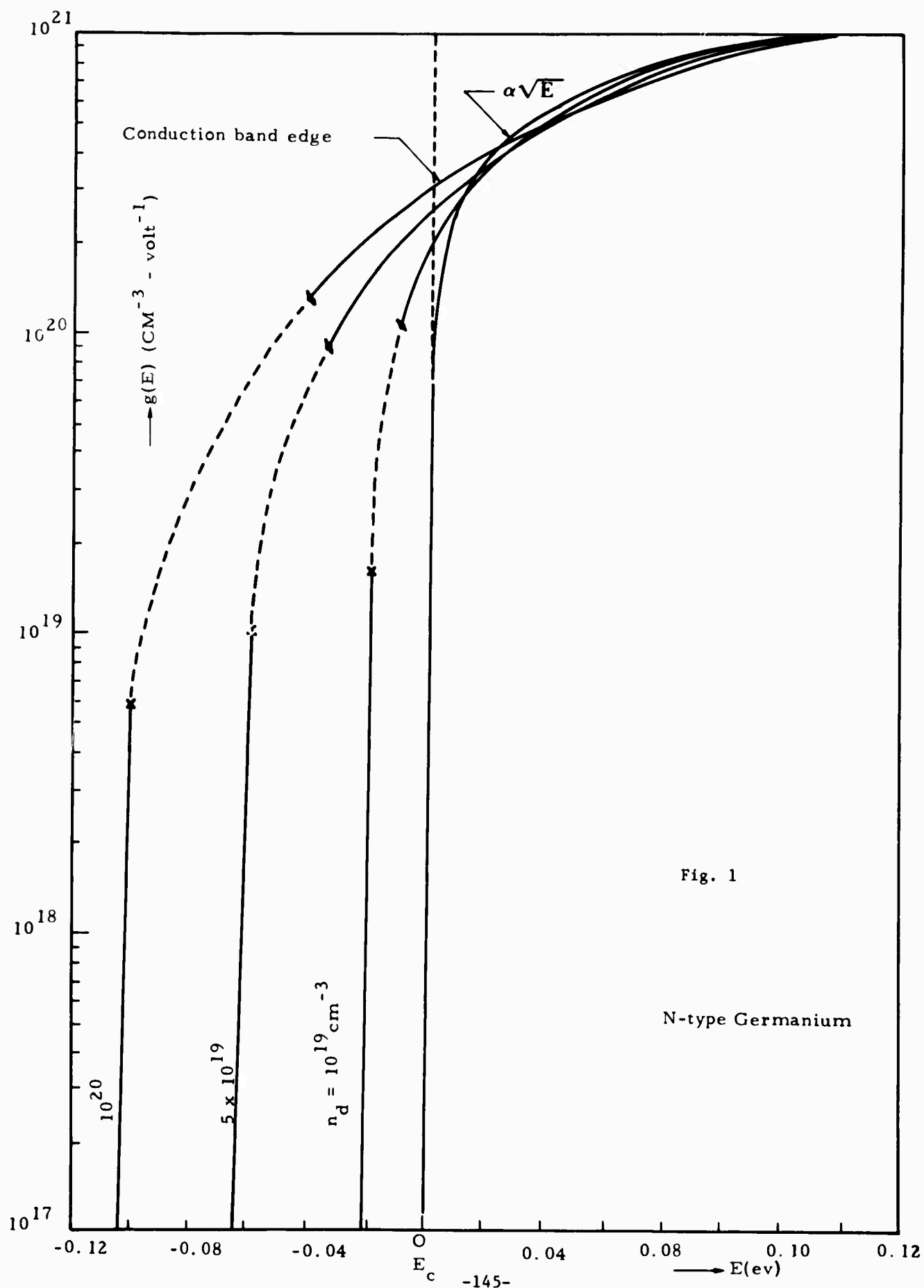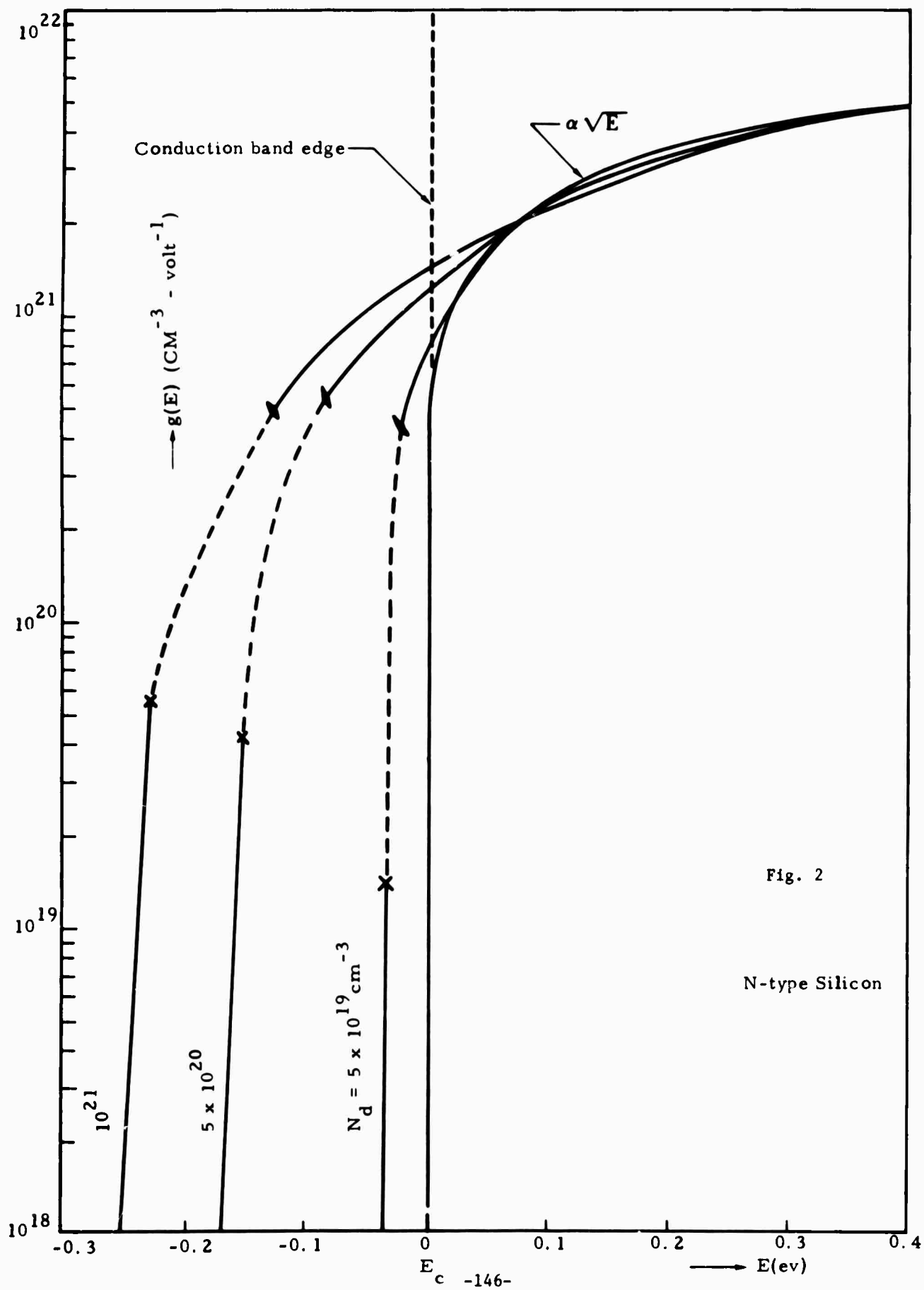
The above approaches yield single-band approximations and are valid
only for the uncompensated or weakly-compensated degenerate materials.

REFERENCES

1. F. D. Shepherd, Jr., V. E. Vickers and A. C. Yang, <u>Proc. IEEE</u> vol. 53 No. 11, pp. 1759-1760, Nov. 1965.

   F. D. Shepherd, Jr., A. C. Yang, V. E. Vickers and T. R. King, Jr., <u>Proc. IEEE</u> (Correspondence) vol. 53, p. 175, Feb. 1965.

2. J. I. Pankove, <u>Phy. Rev</u>. 140, A 2059 (1965).
   G. Lucovsky, <u>Solid State Commun</u>. 3, 105 (1965).

3. T. N. Morgan, ibid, 139, A 343 (1965).
   J. C. Sarace, R. H. Kaiser, J. M. Whelan, and R. C. C. Leite, <u>Phy. Rev</u>. 137, A 623 (1965).

4. B. I. Halperin and M. Lax, <u>Phy. Rev</u>. 148, No. 2, 722 (1966).
   E. O. Kane, <u>Phy. Rev</u>. vol. 131, No. 1, pp. 79-88, July 1963.

5. V. L. Bonch-Bruyevich, <u>The Electronic Theory of Heavily-doped Semiconductors</u>, New York: Elsevier, 1966, pp. 65-76.

Fig. 1   Density of states $g(E)$ vs energy $E(ev)$ for N-type germanium

for $N_D = 10^{19}$, 5×10^{19}, $10^{20} cm^{-3}$ respectively.

◆ denotes the lower limit of B-B approach (5)

x denotes the upper limit of H-L approach (4)

Fig. 2   Density of States $g(E)$ vs energy $E(ev)$ for N-type silicon

for $N_D = 5 \times 10^{19}$, 5×10^{20}, $10^{21} cm^{-3}$ respectively.

◆ denotes the lower limit of B-B approach (5)

x denotes the upper limit of H-L approach (4)

B. EXTENSIONS OF THE THEORY OF PN JUNCTIONS: PART I (D. D. Kleppinger, F. A. Lindholm)

I. INTRODUCTION

This interim report extends the conventional equations for non-degenerate pn step junctions by removing the Boltzmann approximation for carrier densities. The major approximation underlying the present analysis is that the density of states is not a function of impurity concentration. The validity of this approximation is discussed in Section VII.

The problem of describing junctions in material for which Fermi-Dirac statistics must be used is important since most practical devices are made with such material. The emitter-base diode of a diffused, planar transistor is an example.

The works of Bonch-Bruyevich [1] and Ivanchik [2] are examples of the theoretical treatments of degenerate material and junctions that have appeared in the literature. The results that they report are unsuited for direct use in engineering design.

The brief review of some aspects of semiconductor theory that follows is intended to provide a basis for the remainder of the paper and to introduce some of the approximations to be used.

The assumption of non-degeneracy, which is employed in conventional junction theory, permits the use of Maxwell-Boltzmann statistics,

$$f(E) = \exp\left(\frac{E_F - E}{kT}\right), \tag{1}$$

instead of the Fermi-Dirac statistics,

$$f(E) = \left[1 + \exp\left(\frac{E - E_F}{kT}\right)\right]^{-1} \tag{2}$$

This replacement [3,4,5] makes the resulting equations tractable in junction design and is appropriate when the Fermi-level E_F is several kT units of energy

away from the energy of interest, E. For intrinsic germanium and silicon, the Fermi-level lies near the middle of the forbidden energy gap and thereby reflects the non-degeneracy of the material. As impurities are added to the material the Fermi-level approaches one of the band edges [4] and, at great enough impurity concentrations, enters the allowed band. Since in junction analysis the energy of interest which determines the use or non-use of Boltzmann's statistics is the band edge, the Fermi-Dirac statistics must be used at high impurity concentrations.

The equation for the conduction electron density, for example is given by [6]

$$n_o = \int_{E_C}^{\infty} \frac{4\pi(2m_c^*/h^2)^{3/2}(E-E_C)^{1/2}}{1 + \exp[(E-E_F)/kT]} \, dE \qquad (3)$$

where (1) and the density of states function

$$g(E)dE = 4\pi(2m_c^*/h^2)^{3/2}(E-E_C)^{1/2} \qquad (4)$$

have been used. Two assumptions are made in the derivation of (3). The first is that the upper limit of integration can be justified by arguing that $f(E)$ decreases more rapidly than $g(E)$ increases. The dependence of the density of states function on the square root of energy is also an assumption that is valid near the conduction band edge. The basis for this assumption also allows us to use the scalar effective mass. Some further comments on this assumption are made in Section VII. An equation analogous to (3),

$$p_o = \int_{-\infty}^{E_V} \frac{4\pi(2m_v^*/h^2)^{3/2}(E_V-E)^{1/2}dE}{1 + \exp[(E_F-E)/kT]} \quad , \qquad (5)$$

holds for holes and is subject to similar assumptions. Equation (3) has the form

$$n_o = N_C \, \mathfrak{F}_{1/2}(E_F' - E_C') \qquad (6)$$

-151-

where
$$N_C = \frac{2(2\pi m_C^* kT)^{3/2}}{h^3} \tag{7}$$

and
$$\mathcal{F}_{1/2}(E_F^{\iota}-E_C^{\iota}) = 2\pi^{-1/2} \int_0^\infty (E'-E_C^{\iota})^{1/2} [1 + \exp(E'-E_F^{\iota})]^{-1} d(E'-E_C^{\iota}) \tag{8}$$

is a Fermi-Dirac integral [6]. We will assume (6) correctly describes the electron density but we will discuss, in Section VII, the approximation for g(E) and its implications.

Quasi-Fermi levels are used in the development to describe the densities of carriers in non-equilibrium [4,7]. Sah has shown [8] that the quasi-Fermi levels in space charge regions, for the special case of a symmetric step junction,are constant to a good approximation in material doped at high impurity concentrations. In our analysis, we will assume that the quasi-Fermi levels are constant in junction regions.

The remainder of this report proceeds in the following order. In Section II we introduce an approximation for the Fermi-Dirac integral and use it to calculate the np product in equilibrium and non-equilibrium. Section III describes the development of equations for the contact potential of a junction and the Fermi-level. An equation for the excess minority carrier density at the edge of the space charge region is developed in Section IV. Section V presents a quantitative definition of the voltage limit for low injection in terms of impurity concentration. In Section VI we derive an equation for the current density and show, through the use of an extension of the Einstein relationship, that it is identical to the non-degenerate equation. Section VII discusses the results and the assumptions made in obtaining them. Each of the new equations reduces to or is identical with its non-degenerate counterpart in the limit of low impurity concentration.

Illustrative calculations are made for silicon. The values of the material

parameters and various constants used in the calculations are listed in Appendix B. A .able of symbols used throughout the paper is also included, as Appendix A.

2. THE NP PRODUCT

The Fermi integral (8) cannot be integrated analytically but it can be approximated by [6]

$$\mathcal{F}_{1/2}(E_F' - E_C') \approx \frac{\exp(E_F' - E_C')}{1 + 0.27 \exp(E_F' - E_C')} \qquad (9)$$

which is a tractable function for engineering design of junctions. This approximation is accurate to within $\pm$ 3% for $(E_F' - E_C') \leqslant 1.3$ and is applicable to impurity concentrations of interest in this paper.

The equilibrium density of conduction electrons is, from (6) and (9),

$$n_o = N_C \frac{\exp(E_F' - E_C')}{1 + 0.27 \exp(E_F' - E_C')} \qquad (10)$$

The hole density is

$$p_o = N_V \frac{\exp(E_V' - E_F')}{1 + 0.27 \exp(E_V' - E_F')} \qquad (11)$$

in thermal equilibrium. For non-equilibrium, the carrier densities can be expressed in terms of quasi-Fermi levels [4,7]

$$n = N_C \frac{\exp(E_{Fe}' - E_C')}{1 + 0.27 \exp(E_{Fe}' - E_C')} \qquad (12)$$

and

$$p = N_V \frac{\exp(E_V' - E_{Fh}')}{1 + 0.27 \exp(E_V' - E_{Fh}')} \qquad (13)$$

The product of (12) and (13) is

$$np = \frac{N_C N_V \exp(-E_G') \exp(qV')}{1 + \left\{ 0.27[\exp(E_{Fh}' - E_C') + \exp(E_V' - E_{Fe}')] + 0.0729 \exp(-E_G') \right\} \exp(qV')} \qquad (14)$$

-153-

The energy equivalent of the applied voltage, qV', is equal to the difference between the quasi-Fermi levels because of our assumption that the quasi-Fermi levels are constant. Equation (14) can be rewritten as

$$np = \frac{n_i^2 \exp(qV')}{1 + K \exp(qV')} \tag{15}$$

where

$$n_i^2 = N_C N_V \exp(-E_G') \tag{16}$$

The factor K can be evaluated at the n- and p-type edges of the space charge region as follows:

$$K_n = 0.27 \left[\exp(E_F' - E_C' - qV')_n + \exp(E_V' - E_F')_n\right] + 0.0729 \exp(-E_G') \tag{17}$$

and

$$K_p = 0.27 \left[\exp(E_F' - E_C')_p + \exp(E_V' - E_F' - qV')_p\right] + 0.0729 \exp(-E_G'). \tag{18}$$

In (17) and (18), E_F' is to be interpreted as the Fermi-level, normalized with respect to the thermal energy kT, which accounts for the equilibrium carrier densities in the n-type material for (17) and the p-type material for (18). In other words, it is the quasi-Fermi level far enough from the junction that the carrier densities have attained equilibrium values. E_F' appears only with respect to a band edge in the equations and each of the terms are subscripted to remind us to calculate the energy differences on particular sides of the junction.

The equilibrium $(qV' = 0)$ form of (15),

$$n_o p_o = \frac{n_i^2}{1 + 0.27 \left[\exp(E_F' - E_C') + \exp(E_V' - E_F')\right] + 0.0729 \exp(-E_G')} \tag{19}$$

reduces to the conventional non-degenerate form

$$n_o p_o = n_i^2 \tag{20}$$

in the limit of low doping. Equation (19) is valid in bulk material as well as at space charge regions.

Figure 1 shows the behavior of the np product in silicon predicted by (15). The product decreases from that expected from the conventional expression as the impurity concentration increases. This decrease follows from consideration of the statistics which show that the minority carrier density decreases faster with increasing doping than the majority carrier density increases. The denominator of (15) is a function of voltage as well as impurity concentration but the voltage dependence does not become important until the applied voltage is within a few percent of the low injection voltage limit to be defined in Section V. Figure 1 is therefore applicable to low injection non-equilibrium in addition to equilibrium.

Equation (14) is actually more general than we have thus far implied since it can be applied to any situation where the differences $(E'_{Fh} - E'_C)$ and $(E'_V - E'_{Fe})$ can be evaluated. In particular these differences can be determined from the equations which describe the spatial variation of the band edges throughout a junction region and the resulting np product can be used to study recombination in the junction region as a function of position and applied voltage.

3. THERMAL EQUILIBRIUM: THE FERMI LEVEL AND THE CONTACT POTENTIAL

Equations for the Fermi-levels may be obtained by using charge neutrality along with (10) for n-type material or (11) for p-type material. Let us consider uncompensated n-type material which is sufficiently extrinsic that the number of holes is negligible. Space charge neutrality then requires that

$$n_o = N_D^+ \tag{21}$$

where

$$N_D^+ = \frac{N_D}{1 + 2 \exp(E'_F - E'_D)} \tag{22}$$

The factor of 2 in (22) accounts for the degeneracy of the impurity level [9].

-155-

Figure 1
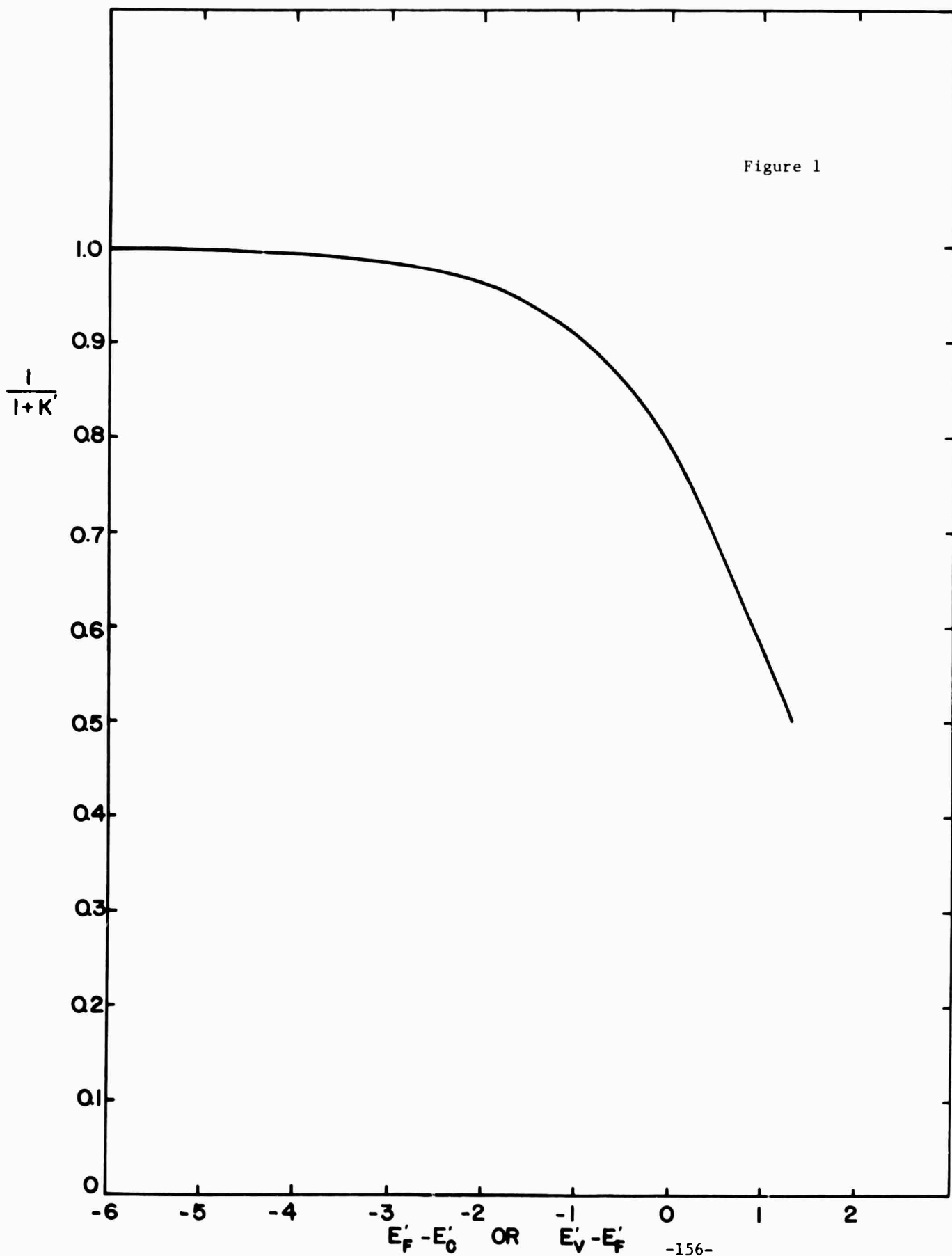
Therefore,

$$\frac{N_C \exp(E_F' - E_C')}{1 + 0.27 \exp(E_F' - E_C')} = \frac{N_D}{1 + 2 \exp(E_F' - E_D')} \tag{23}$$

When the substitutions

$$\alpha = \exp(E_F'), \quad \beta_C = \exp(-E_C'), \quad \text{and} \quad \beta_D = \exp(-E_D') \tag{24}$$

are made, (23) becomes

$$\frac{N_C \alpha \beta_C}{1 + 0.27 \alpha \beta_C} = \frac{N_D}{1 + 2 \alpha \beta_D} \tag{25}$$

The solution for α is

$$\alpha = -\frac{N_C - 0.27 N_D}{4 N_C \beta_D} + \left[\frac{(N_C - 0.27 N_D)^2}{(4 N_C \beta_D)^2} + \frac{N_D}{2 N_C \beta_C \beta_D} \right]^{1/2} \tag{26}$$

where the positive square root is chosen so that E_F' is real. Using the identity

$$\ln(x + \sqrt{x^2 + a^2}) = \ln a + \sinh^{-1} \frac{x}{a} ,$$

we can obtain the Fermi-level as

$$E_F = \frac{1}{2}(E_C' + E_D') + \frac{1}{2} \ln\left(\frac{N_D}{2N_C}\right) - \sinh^{-1}\left[(N_C - 0.27 N_D)(8 N_C N_D)^{-1/2} \exp\left(\frac{E_D' - E_C'}{2}\right) \right]. \tag{27}$$

Similarly, in uncompensated p-type material under the assumption of negligible electron density, the Fermi-level is

$$E_F' = \frac{1}{2}(E_V' + E_A') - \frac{1}{2} \ln\left(\frac{N_A}{2N_V}\right) + \sinh^{-1}\left[(N_V - 0.27 N_A)(8 N_V N_A)^{-1/2} \exp\left(\frac{E_V' - E_A'}{2}\right) \right]. \tag{28}$$

If the impurity concentration is such that 0.27 N_D may be neglected with respect to N_C in (27), the equation reduces to the non-degenerate expression [9],

$$E'_F = \frac{1}{2}(E'_C + E'_D) + \frac{1}{2}\ln(\frac{N_D}{2N_C}) - \sinh^{-1}\left[(N_C/8N_D)^{1/2}\exp(^{E'_D - E'_C})\right] . \quad (29)$$

When N_D has increased to a value such that the reduction of (27) to (29) cannot be allowed in good conscience, we may define that level of doping as the border-line separating non-degeneracy and degeneracy. This is an arbitrary definition but (27) does permit a comparison directly between the impurity concentration and the effective density of states for the particular material. The arbitrariness of the definition arises from the need to choose how large N_{ι} will be allowed to get with respect to N_C before (29) is not a valid reduction of (27).

Figure 2 illustrates the behavior predicted by (27) and (28) for phosphorous or boron doped silicon. The Fermi-level monotonically approaches the band edge as the impurity concentration increases. At equal impurity concentrations, the Fermi-levels are not in the same position relative to the nearest band edge in n- and p-type material because of the difference between the effective density of state values. A difference between activation energies for the donors and acceptors would also cause a difference between the relative Fermi-level positions. (See Appendix B for values used in the illustrative calculations).

Equations 10 and 11 may be solved for the Fermi-level:

$$E'_F = E'_C - \ln\left[\frac{N_C - 0.27\,n_{no}}{n_{no}}\right] \quad (30)$$

in n-type material and

$$E'_F = E'_V + \ln\left[\frac{N_V - 0.27\,p_{po}}{p_{po}}\right] \quad (31)$$

in p-type material. Equations (30) and (31) can be used to calculate the Fermi-

-158-
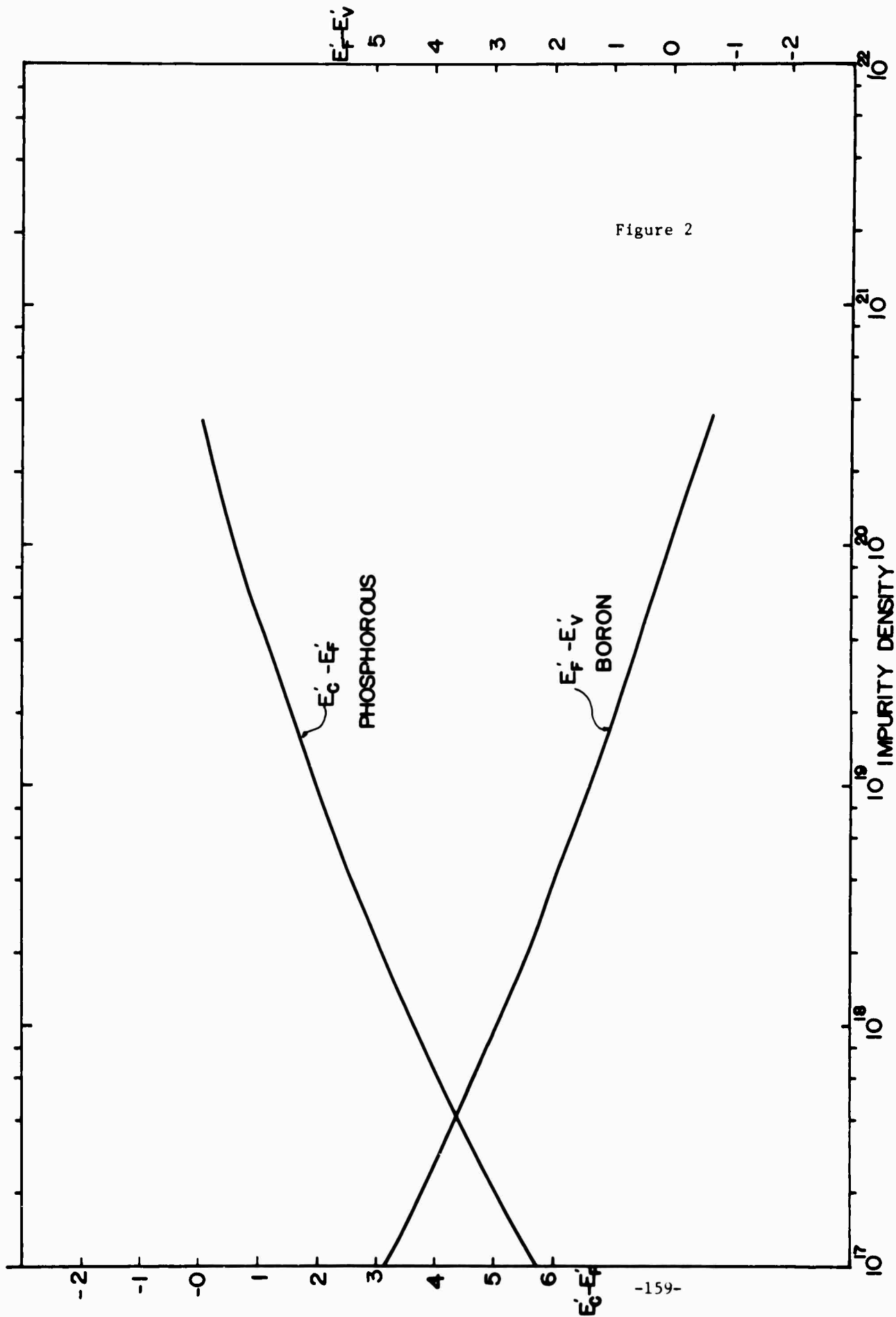
Figure 2

level position as a function of carrier density while (27) and (28) show the dependence of the Fermi-level on the concentration and the characteristics of the impurities through the activation energy. The two sets of equations therefore provide complementary information and additional insight.

Equations (10) and (11) can be used together to develop an equation for the contact potential of a pn junction. The definition for N_V is analogous to (7) for N_C.

$$N_V = \frac{2(2\pi m_V^* kT)^{3/2}}{h^3} \tag{32}$$

Then N_C is related to N_V by

$$\frac{N_C}{N_V} = \left(\frac{m_C^*}{m_V^*}\right)^{3/2} \tag{33}$$

so that (16) may be rewritten

$$N_C = \left(\frac{m_C^*}{m_V^*}\right)^{3/4} n_i \exp\left(\frac{E_G'}{2}\right) \tag{34}$$

or

$$N_V = \left(\frac{m_V^*}{m_C^*}\right)^{3/4} n_i \exp\left(\frac{E_G'}{2}\right) \tag{35}$$

The density of electrons on the n-type side of the junction is by (10)

$$n_{no} = \frac{n_i \left(\frac{m_V^*}{m_C^*}\right)^{3/4} \exp(E_F' - E_C' + \frac{E_G'}{2})}{1 + 0.27 \exp(E_F' - E_C')} \tag{36}$$

and the density of holes on the p-type side of the junction is by (11)

$$p_{po} = \frac{n_i \left(\frac{m_V^*}{m_C^*}\right)^{3/4} \exp(E_V' - E_F' + \frac{E_G'}{2})}{1 + 0.27 \exp(E_V' - E_F')} \tag{37}$$

Choosing the reference energy as $E_V' = 0$ (therefore $E_C' = E_G'$) and taking the

logarithm of these equations, we obtain

$$\ln \frac{n_{no}}{n_i \left(\frac{m_C^*}{m_V^*}\right)^{3/4}} = (E_F' - \frac{E_G'}{2}) - \ln[1 + 0.27 \exp(E_F' - E_C')] \qquad (38)$$

and

$$\ln \frac{P_{po}\left(\frac{m_C^*}{m_V^*}\right)^{3/4}}{n_i} = -E_F' + \frac{E_G'}{2} - \ln[1 + 0.27 \exp(E_F' - E_C')] \qquad (39)$$

The contact potential can be obtained as the potential equivalent of the energy difference between any two identically defined energies on the two sides of the junction. In the present case, the contact potential can be obtained from the difference in energy between the mid-gap energies ($E_G'/2$) shown in the above equations. If (38) and (39) are rearranged and subtracted, the result is

$$\frac{E_G'}{2}\bigg|_p - \frac{E_G'}{2}\bigg|_n = \ln\left[\frac{n_{no}}{n_i\left(\frac{m_C^*}{m_V^*}\right)^{3/4}} \frac{P_{po}\left(\frac{m_C^*}{m_V^*}\right)^{3/4}}{n_i}\right]$$

$$+ \ln[1 + 0.27 \exp(E_F' - E_G')] + \ln[1 + 0.27 \exp(-E_F')] \qquad (40)$$

from which

$$qV_D' = \ln\left[\frac{n_{no}P_{po}}{n_i^2}\right] + \ln[1 + 0.27 \exp(E_F' - E_C')_n]$$

$$+ \ln[1 + 0.27 \exp(E_V' - E_F')_p] . \qquad (41)$$

In (41) the reference energy has been changed so that the exponentials explicitly show dependence on the position of the Fermi-level with respect to the band edges. The subscripts on the arguments of the exponentials are to remind us exactly what energy difference is required. Equation (41) correctly predicts that the

-161-

potential of the n-type region is positive with respect to the p-type region. (Recall that qV_D' is a normalized energy equivalent of the contact potential V_D.)

The form of (41) is interesting. The conventional non-degenerate contact potential equation is

$$qV_D' = \ln \frac{n_{no}p_{po}}{n_i^2} \tag{42}$$

or more usually,

$$qV_D' = \ln \frac{N_D N_A}{n_i^2} \tag{43}$$

where 100% ionization is assumed in (43). The first term of (41) is the same as (42) hence the last two terms of (41) can be thought of as correction terms to the non-degenerate equation. Equation (41) reduces to (42) when the correction terms are negligible and this occurs for low doping concentrations on both sides of the junction. The form of (41) makes it clear that there will be a correction term even if only one side of the junction is heavily doped. The correction terms are always positive so (42) underestimates the contact potential. Equation (43) always overestimates the contact potential for doping densities greater than 10^{16}cm^{-3}. The estimates made by using (42) or (43) become less accurate as doping increases with (43) leading to very considerable errors, as is discussed below.

Figure 3 illustrates the behavior predicted by (41) for junctions in silicon doped with phosphorous and boron. The contact potential increases as either or both sides of the junction become more heavily doped.

Figure 4 indicates the magnitude of the correction terms in (41) and therefore the error which would arise from using (42). The error involved in using (43) is also shown for the single case of equal doping on both sides of the junction. The errors do increase with increasing doping as mentioned above.

-162-
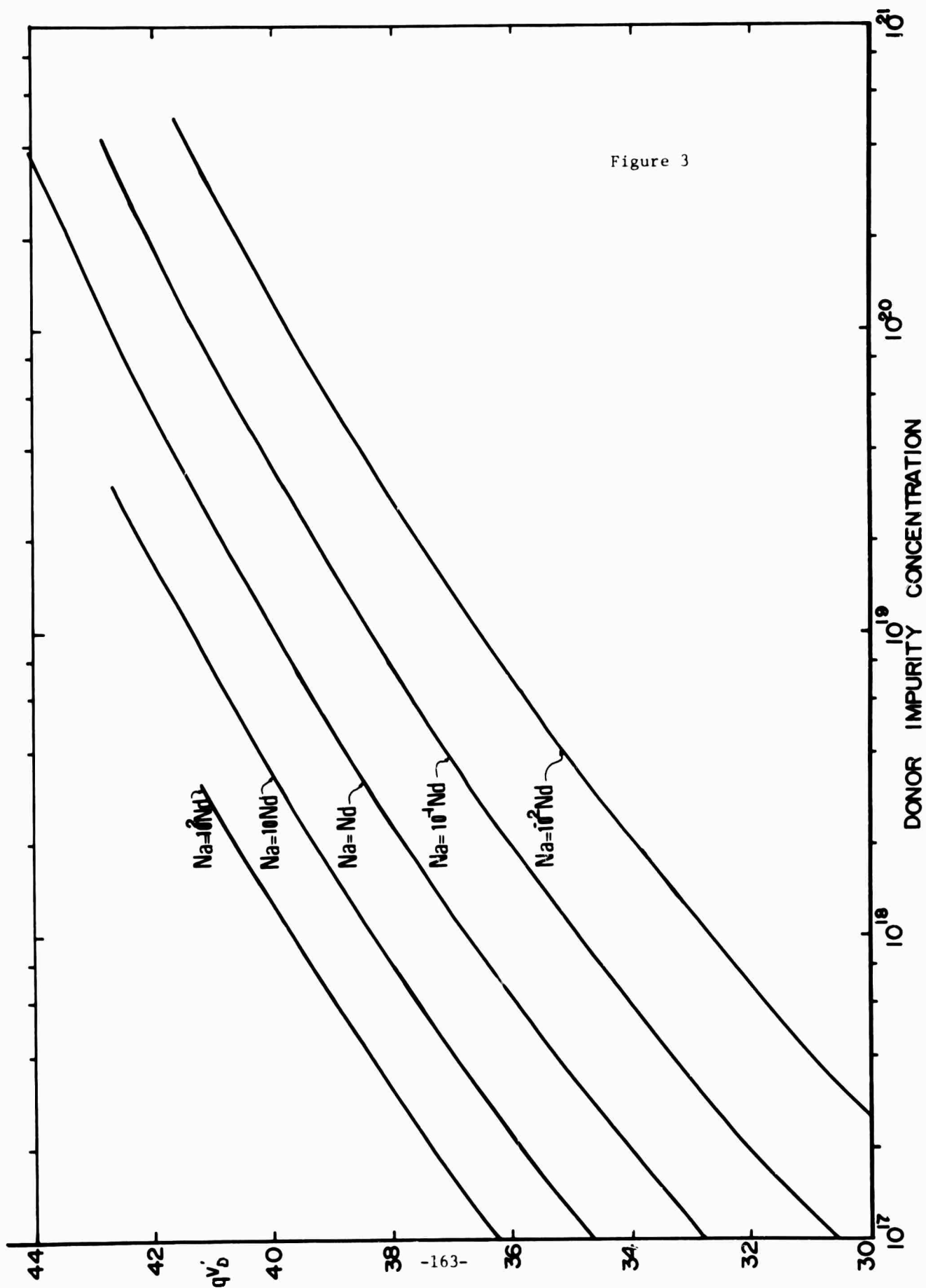
Figure 3
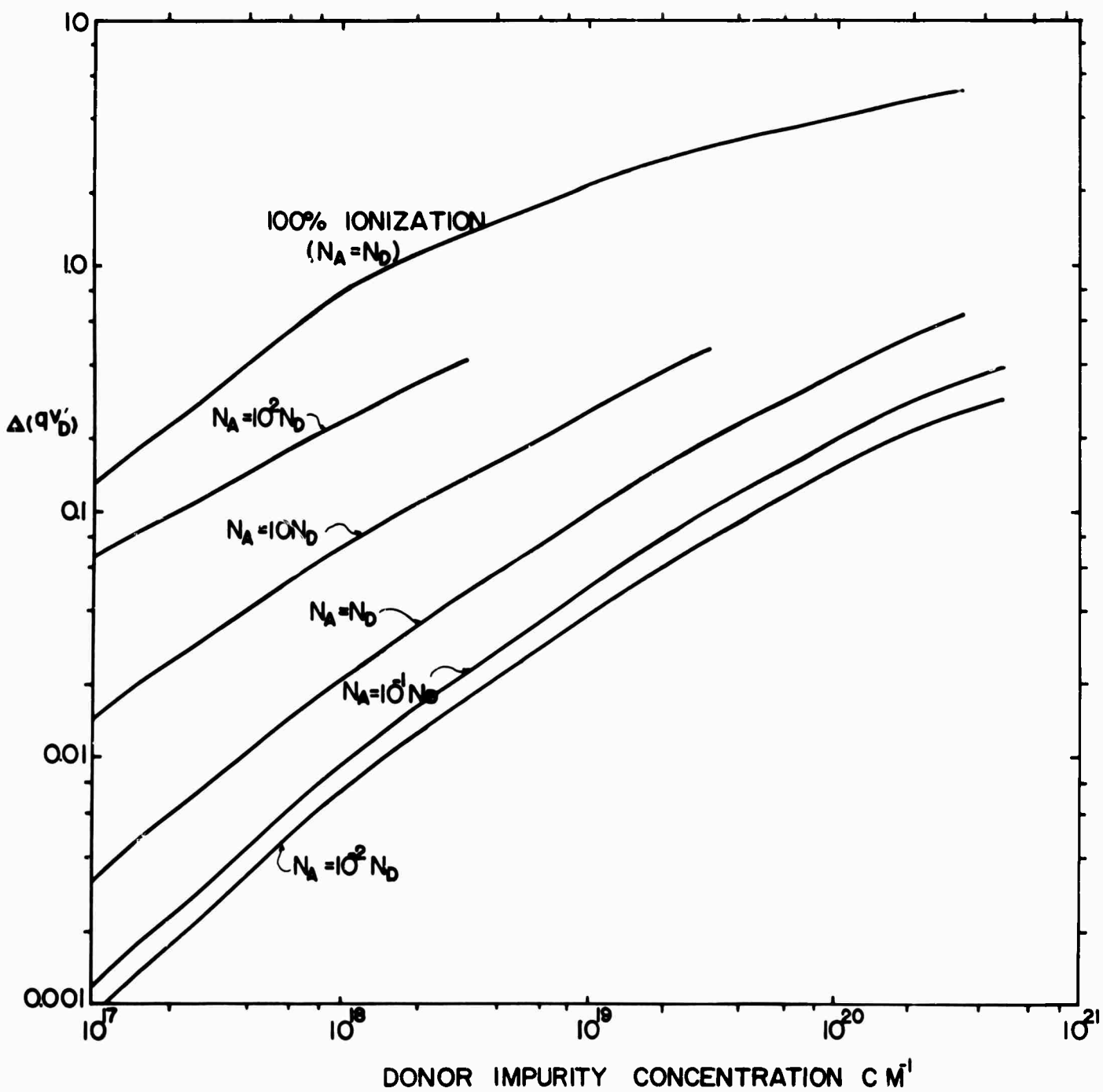
Figure 4

Figure 4

Figure 5 was generated in the course of the investigation and is included for reference. The curves clearly show that 100% ionization is a poor approximation over most of the range of useful impurity densities. The difference between the curves for phosphorous and boron is due to the difference in the carrier effective masses and hence the effective density of states, (7) and (32). The ionization energy of the impurity will also determine the position of the curve. The values shown in Figure 5 were calculated using (41) and (10) or (11).

An alternative equation for the contact potential is

$$(qV_D') \; = \; E_G' + (E_F' - E_C')_n + (E_V' - E_F')_p. \tag{44}$$

Equation (44) can be obtained by combining (41), (9), (10), and (16) or by inspection from an energy band diagram of a junction in equilibrium. Figure (10) in Appendix A is such a diagram. Equations (44) and (41) are valid in general; however, (41) shows explicitly the correction terms while (44) provides ease of computation since both equations require the same energy differences to be known.

4. THE EXCESS MINORITY CARRIER DENSITY AT THE SPACE CHARGE REGION EDGE

An equation which gives the excess hole concentration at the edge of the space charge region at the n-type side of the junction can be obtained by starting with (13). For a forward biased junction, the excess minority hole density in the n-type quasi-neutral region achieves its largest value at the edge of the space charge region. If the total density of holes, equilibrium plus excess, at the edge of the space charge region is small compared to the density of majority electrons present, we define this condition as low injection. Equation (13) can be rewritten as

$$P_n \; = \; \frac{N_V \exp(E_V' - E_F') \exp(E_F' - E_{Fh}')}{1 + 0.27 \exp(E_V' - E_F') \exp(E_F' - E_{Fh}')}. \tag{45}$$

The majority carrier density is assumed to deviate negligibly from its equilibrium

Figure 5
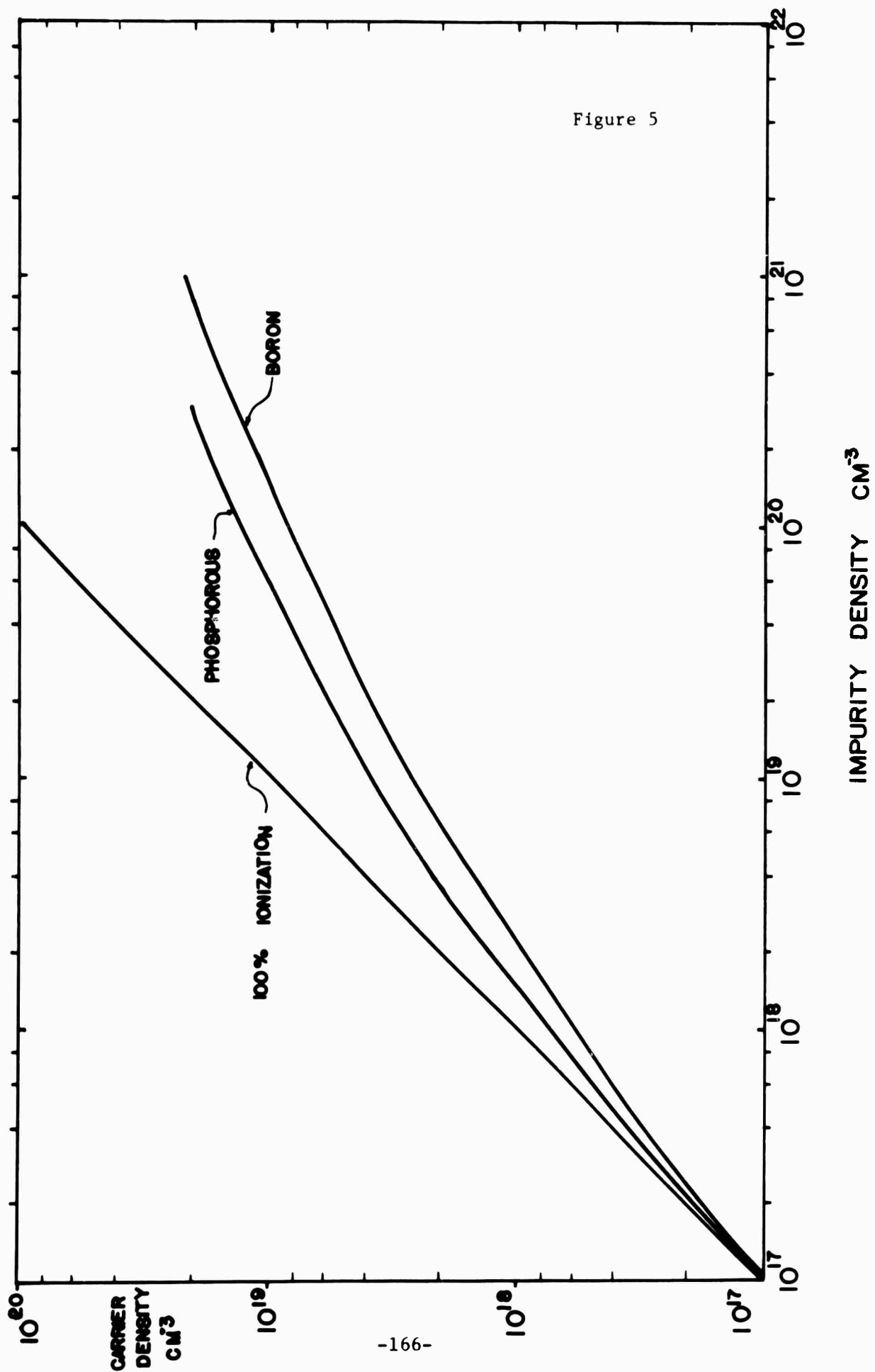
value. This assumption implies

$$E_F' = E_{Fc}'$$ (46)

and (45) may be re-expressed as

$$p_n = \frac{N_V \exp(E_V' - E_F') \exp(qV')}{1 + 0.27 \exp(E_V' - E_F') \exp(qV')}.$$ (47)

The assumption of constant quasi-Fermi levels was used as in Section II to relate the applied voltage to the difference between the quasi-Fermi levels.

The <u>total</u> density of minority holes at the space charge region edge is

$$p_n = p_{no} \frac{[1 + 0.27 \exp(E_V' - E_F')] [\exp(qV')]}{1 + 0.27 \exp(E_V' - E_F') \exp(qV')}$$ (48)

by rewriting (47); therefore the <u>excess</u> minority hole density is

$$p_1 = p_n - p_{no} = \frac{p_{no}[\exp(qV') - 1]}{1 + 0.27 \exp(E_V' - E_F')_n \exp(qV')}.$$ (49)

Equations (48) and (49) are based on the assumption of low injection. The result of the development to be made in Section 5 shows that the denominator of (49) may become different from unity for certain combinations of impurity concentration and applied voltage without violating the assumption of low injection. Thus, for these combinations, the excess minority carrier density will be less than the value predicted by the non-degenerate equation

$$p_1 = p_{no} [\exp(qV') - 1] .$$ (50)

Notice further that the value of p_{no} in (49) should be calculated by using (11) or (19) and not by using $p_{no} = n_i^2/n_{no} = n_i^2/N_D$ as would be done for non-degenerate cases.

The excess density of electrons at the edge of the space charge region in p-type material is

$$n_1 = n_p - n_{po} = \frac{n_{po} [\exp(qV') - 1]}{1 + 0.27 \exp(E_F' - E_C')_p \exp(qV')}$$ (51)

by analogy with (49).

-167-

5. A QUANTITATIVE DEFINITION OF LOW INJECTION

The qualitative definition of low injection given in Section IV can be made quantitative. Low injection was described as being the condition existing when the total density of minority carriers is small with respect to the density of majority carriers at the space charge region edge. Recall that the minority carrier density in the quasi-neutral region will have its greatest value at the space charge region edge. The definition can be written as

$$p_n \overset{<}{=} F \, n_{no},\tag{52}$$

at the edge of the space charge region on the n-type side, where F is some number less than unity. The voltage at which

$$p_n = F \, n_{no}\tag{53}$$

is now defined as the voltage limit for low injection and its value may be found by substituting (9) and (47) into (53),

$$\frac{N_V \exp(E'_V - E'_F)_n \exp(qV'_L)}{1 + 0.27 \exp(E'_V - E'_F)_n \exp(qV'_L)} = \frac{FN_C \exp(E'_F - E'_C)_n}{1 + 0.27 \exp(E'_F - E'_C)_n}.\tag{54}$$

The solution to (54) is

$$qV'_L = \ln F + \frac{3}{2} \ln\left(\frac{m^*_C}{m^*_V}\right) + (E'_F - E'_C)_n + E'_G - \ln \left\{ \exp[-(E'_F - E'_C)_n] + 0.27[1 - F\left(\frac{m^*_C}{m^*_V}\right)^{3/2}] \right\}\tag{55}$$

where the relationships $(E'_V - E'_F)_n \cdot - E'_G - (E'_F - E'_C)_n$ and (33) have been used. For a given material (which determines m^*_C/m^*_V) the maximum voltage for which low injection exists (as defined by F) can be calculated as a function of impurity concentration by using (55).

Figure 6 indicates the predictions of (55) as a graph of qV'_L versus $(E'_F - E'_C)_n$ with F as a parameter. For a given F, the voltage required to violate the definition of low injection, (52) increases as the impurity concentration increases. This is reasonable since a larger number of injected carriers will be required to

Figure 6

-169-
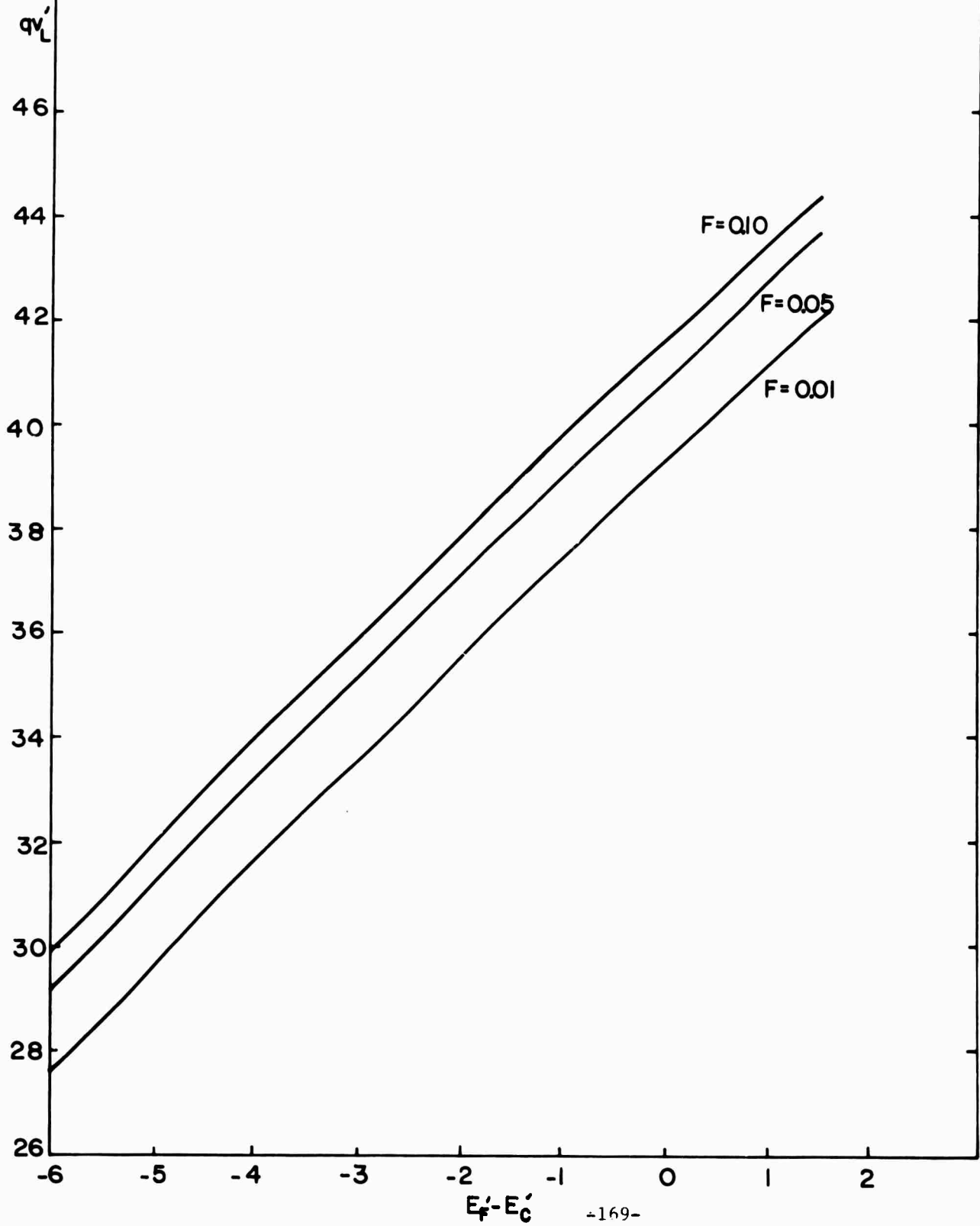
attain the given fraction of the increasing number of majority carriers. Also reasonable is the observation that, at a given impurity concentration, the maximum voltage allowed decreases as the fraction, F, decreases since less voltage is required to cause the injection of the smaller density of carriers. The abscissa is plotted as $(E_F' - E_C')$ to make the graph applicable to silicon in general. The graph may be made specific for phosphorous doped silicon by using Figure 2 to obtain $(E_F' - E_C')$ for a given impurity concentration.

The equation analogous to (55) for injection into p-type material is

$$qV_L' = \ln F + \frac{3}{2} \ln\left(\frac{m_V^*}{m_C^*}\right) + (E_V'-E_F')_p + E_G' - \ln \{\exp[-(E_V'-E_F')_p] + 0.27 [1-F\left(\frac{m_V^*}{m_C^*}\right)^{3/2}]\} .$$
(56)

The voltage limit for low injection can be compared to the contact potential by using (41) and (55). Figure 7 illustrates this comparison for the F = 0.1 by displaying the ratio qV_L'/qV_D' versus impurity concentration in phosphorous doped silicon. If the low injection limit voltage exceeds the contact potential, low injection cannot be violated since a voltage greater than the contact potential cannot be applied to the junction. The curves show that the low injection criteria can be violated on the more lightly doped side of the junction but cannot be violated on the more heavily doped side. The qualitative results are not unexpected but the quantitative results are interesting.

Equation (55) may be used to study the behavior of the denominator of (49), the equation for the excess minority carrier (hole) density at the edge of the space charge region. The questions to be answered are: (1) Does the denominator differ from unity before the low injection assumption is violated? and (2) Does the denominator differ from unity because of its dependency on impurity concen-
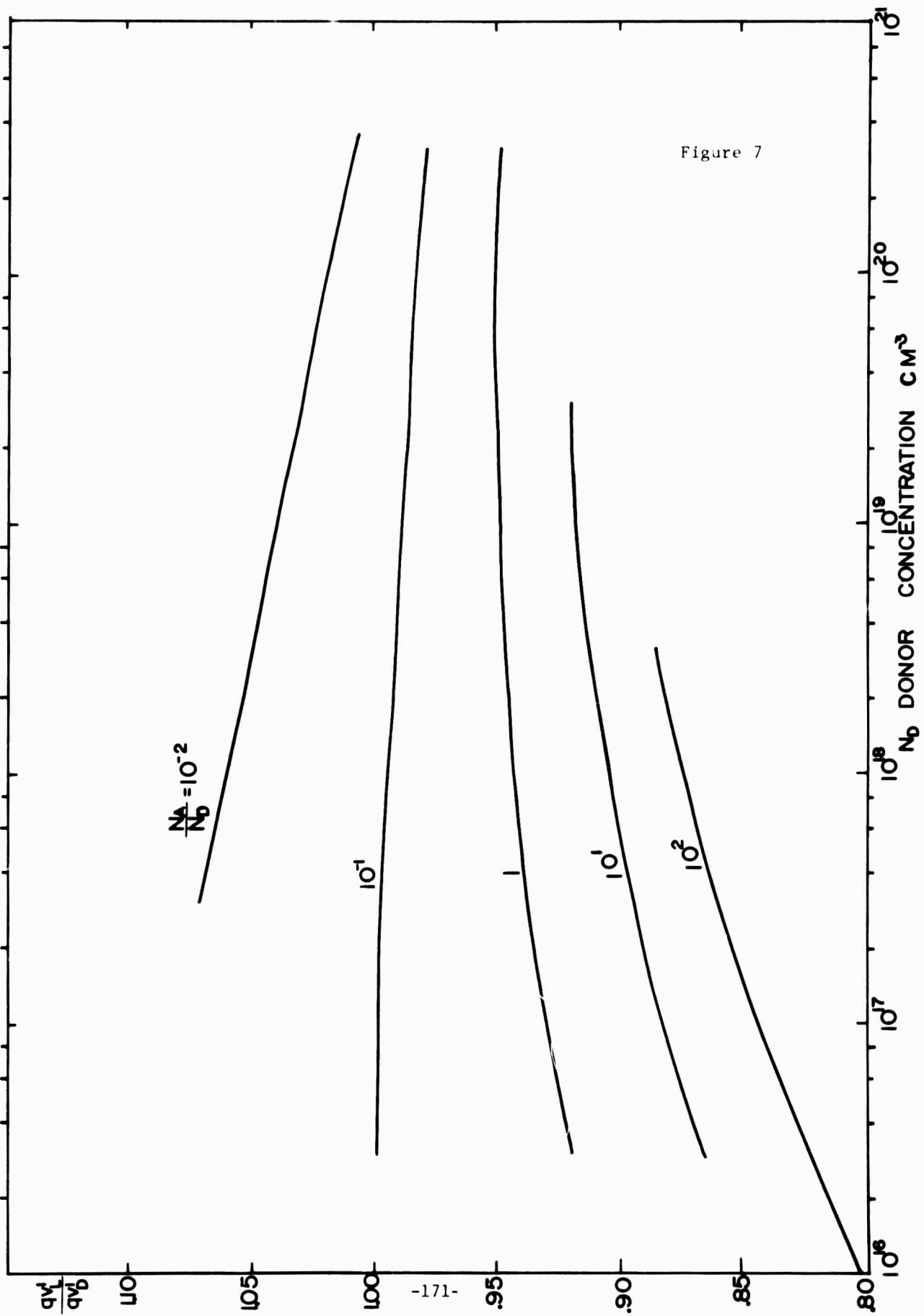
Figure 7

$\frac{N_A}{N_D}=10^{-2}$

10^{-1}

1

10^{1}

10^{2}

N_D DONOR CONCENTRATION CM^{-3}

10^{16} 10^{17} 10^{18} 10^{19} 10^{20} 10^{21}

$\frac{qV_d}{qV_b}$

1.10

1.05

1.00

.95

.90

.85

.80

-171-

tration?   The answers developed below, to these questions show that (49) does not reduce to the non-degenerate form (50) in general because the denominator does differ from unity under certain conditions.

If the applied voltage is cqV_L', where $c \leq 1$, the denominator of (49) becomes

$$\text{Denom.} = 1 + 0.27 \exp(E_V' - E_F')_n \cdot \left\{ \frac{F\left(\frac{m_C^*}{m_V^*}\right)^{3/2} \exp(E_F' - E_C')_n}{\exp(E_V' - E_F')_n + 0.27\left[1 - F\left(\frac{m_C^*}{m_V^*}\right)^{3/2}\right]\exp(-E_G')} \right\}^c \quad (57)$$

where $\exp(cqV_L') = [\exp(qV_L')]^c$ and (55) have been used.

Figure 8 presents the predictions of (57) for the behavior of the denominator at several values of c with F = 0.1 and for c = 1 with F = 0.05. When the number calculated from (57) is greater than unity, the excess density of minority carriers (holes) is less than the density predicted by the non-degenerate equation (50). This deviation does occur for higher concentrations at applied voltages near the low injection limit of voltage. Equation (49) does not reduce to (50) in all cases but does in the proper limits.

The discussion of the voltage dependence of the denominator of (15), which we postponed in Section 11, proceeds similar to the above discussion for (49). Our purpose is to show that the denominator does not depend on voltage for voltages below approximately 97% of the low injection limit and, therefore, that Figure 1 is valid for voltages (including zero) less than this. Figure 9 illustrates the departure of the denominator from its equilibrium value for voltages equal to 0.97 qV_L' and 1.0 qV_L'. The curves substantiate the remark in Section 11 that Figure 1 is valid for voltages less than approximately 97% of the low injection voltage limit. The calculations for Figure 9 were made with F = 0.1 which is probably the greatest amount one would define as low injection. Smaller values of F would lead to smaller departures from the curve of Figure 1 for any given voltage including qV_L'. At $N_D = 3 \times 10^{20}$ cm^{-3} for example, with F = 0.1

-172-

Figure 8

Figure 9

-174-
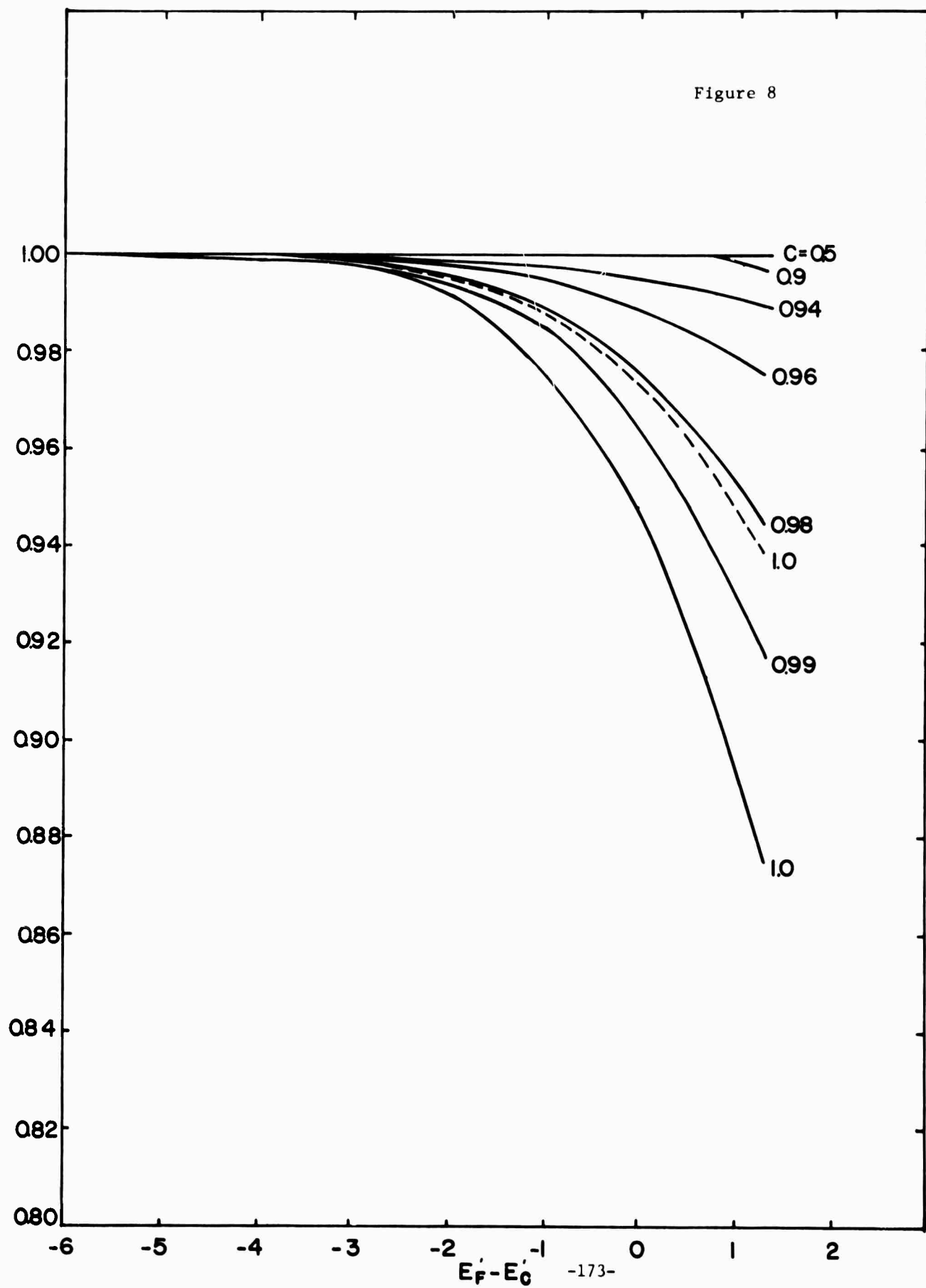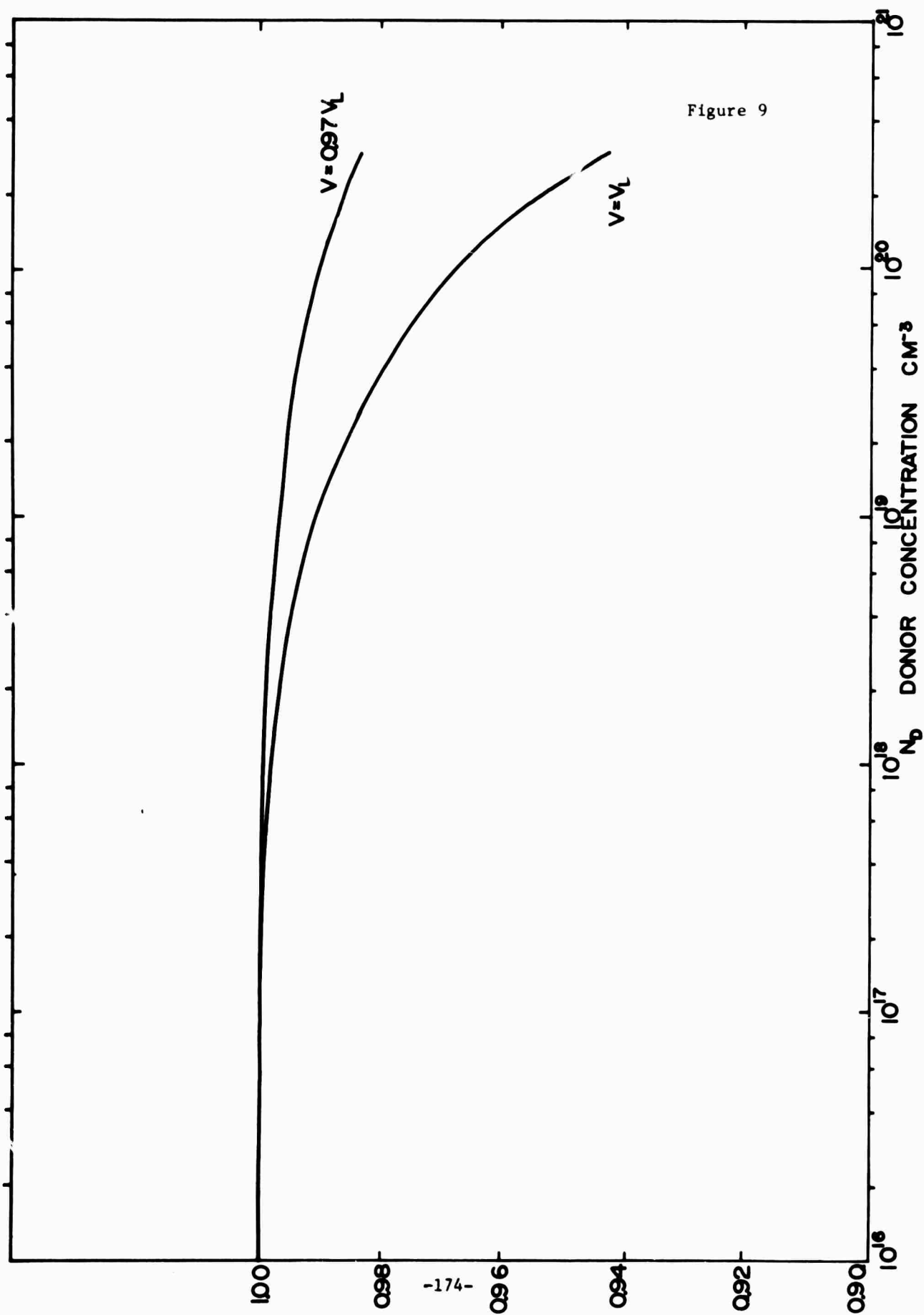
and $qV' = qV'_L$, Figure 9 shows that the ratio is 0.943 whereas a calculation would show that the ratio is 0.991 if $F = 0.01$ and $qV' = qV'_L$.

6. THE CURRENT DENSITY EQUATION

The electrical current density due to electrons is given by

$$J_n = q \mu_n n \mathcal{E}_x + q D_n \frac{dn}{dx} \tag{58}$$

in one dimension. The n and $\frac{dn}{dx}$ factors in (5) may be evaluated by using the non-equilibrium form of (6),

$$n = N_c \mathcal{F}_{\frac{1}{2}} (E'_{Fe} - E'_C) , \tag{59}$$

where the Fermi-Dirac integral is analogous to (8).

The derivative in (57) may be written

$$\frac{dn}{dx} \quad \left(\frac{\partial n}{\partial E'_C} \right)_{E'_{Fe}} \frac{dE'_C}{dx} + \left(\frac{\partial n}{\partial E'_{Fe}} \right)_{E'_C} \frac{dE'_{Fe}}{dx} \tag{60}$$

and it is noted that [4]

$$\frac{dE'_C}{dx} = \frac{q \mathcal{E}_x}{kT} \tag{61}$$

The two partial derivatives are evaluated using Liebnitz' rule [10] to obtain

$$\left(\frac{\partial n}{\partial E'_C} \right)_{E'_{Fe}} = - N_C - \frac{1}{2} (E'_{Fe} - E'_C) \tag{62}$$

and

$$\left(\frac{\partial n}{\partial E'_{Fe}} \right)_{E'_C} = - \frac{2}{\sqrt{\pi}} N_C \int_{E'_C}^{\alpha} (E' - E'_C)^{1/2} \frac{df(E')}{dE'} . \tag{63}$$

-175-

The current density equation becomes

$$J_n = q\mu_n n\epsilon_x + q\,D_n\left[-N_C\,\mathfrak{F}_{-1/2}(E'_{Fe}-E'_C)\frac{q_x}{kT} - \frac{dE'_{Fe}}{dx}\frac{2}{\sqrt{\pi}}\,N_C\int_{E'_C}^{\infty}(E'-E'_C)^{1/2}\frac{df(E')}{dE'}\,dE'\right] \tag{64}$$

or

$$J_n = q\mu_n n\epsilon_x - qD_n\left\{[N_C\,\mathfrak{F}_{1/2}(E'_{Fe}-E'_C)]\left[\frac{\mathfrak{F}_{-1/2}(E'_{Fe}-E'_C)}{\mathfrak{F}_{1/2}(E'_{Fe}-E'_C)}\frac{q}{kT}\right]\epsilon_x \;+\;\right.$$

$$\left.\frac{dE'_{Fe}}{dx}\frac{2}{\sqrt{\pi}}\,N_C\int_{E'_C}(E'-E'_C)^{1/2}\frac{df(E')}{dE'}\,dE'\right\}\cdot \tag{65}$$

If Li and Lindholm's generalized Einstein relationship [11]

$$\frac{\mathfrak{F}_{-1/2}(E'_F - E'_C)}{\mathfrak{F}_{1/2}(E'_F - E'_C)} = \frac{kT}{q}\frac{\mu_n}{D_n} \tag{66}$$

is assumed to be valid in non-equilibrium, equation (65) can be rewritten

$$J_n = -\frac{dE'_{Fe}}{dx}\frac{2q}{\sqrt{\pi}}\,N_C D_n\int_{E'_C}^{\infty}(E'-E'_C)^{1/2}\frac{df(E')}{dE'}\,dE', \tag{67}$$

where (59) has been used also. If (67) is integrated by parts and combined with (59) and (66), the result is

$$J_n = \mu_n n\,\frac{dE_{Fe}}{dx} \tag{68}$$

This equation is identical to that derived for the non-degenerate case [4] but it has been derived by considering Fermi-Dirac statistics and the variation of the Einstein relation with impurity concentration; therefore, (68) has been shown more generally to be valid at higher impurity concentrations than previously demonstrated with the conventional non-degenerate Einstein relation.

The corresponding equation for the current due to holes is given by

$$J_p = \mu_p p\,\frac{dE_{Fh}}{dx} \tag{69}$$

The thought may occur to the reader that one of the basic assumptions of this work has been the constancy of the quasi-Fermi level, but (68) includes the spatial derivative of the quasi-Fermi level. The rationale for this paradox lies in the meaning of the assumption. The assumption that was really made was that the change in the quasi-Fermi level across the junction was so small that it was negligible for the prupose of computing the voltage across the junction. However, the small change that is present is represented by an equally small slope which is sufficient, when multiplied, cf.(68), by the enormous number of carriers present, to account for current.

7. DISCUSSION AND CONCLUSIONS

We set out to develop, under certain assumptions, a set of equations for pn junction behavior which would be valid at impurity concentrations beyond the conventional non-degenerate range. The approach we took was to remove the assumption of non-degeneracy and to make an approximation (9) for the Fermi-Dirac statistics. This approximation is tractable for engineering calculations and is accurate to $\pm$ 3% if the Fermi level is not more than 1.3 kT into the allowed band. The resulting equations for step junctions reduce to, or are identical with, the conventional equations in the limit of low impurity concentration.

The major assumption which served as the basis for the work was that the semiconductor band edges and the impurity energy levels were unaffected by increasing impurity concentrations. Experimental and theoretical results show that this assumption is not valid [12,13,14]. The single energy level of the impurity atoms at low concentration widens to a band of energies due to the impurities when the concentration is great enough that the impurity atoms interact. The onset of the widening has been reported to be as low as at approximately 10^{17} donor impurities per cubic centimeter in silicon [12]. The

widening of the impurity level to a band changes the effective activation energy of the impurity and affects the carrier density accordingly. Furthermore, the density of states at the band edges deviates from the parabolic dependence on energy which we have assumed (4) and states become available in the previously forbidden energy gap. This deviation, often called "band tails", also increases with increasing impurity concentrations and further affects the activation energy of the impurities. In fact, the impurity band and the allowed band merge at high impurity concentrations and the activation energy becomes zero. Bonch-Bruyevich [1] reports that this occurs at donor impurity concentration of approximately $10^{18} cm^{-3}$ in silicon and approximately $3 \times 10^{17} cm^{-3}$ in germanium. The effect of impurity bands and band tails on the results derived in this interim report are being investigated.

In addition to the major assumption concerning the quantum density of states, we have tacitly made two other assumptions. The validity of these two merits discussion. First, the existence of the tunnelling phenomena is well-known and its occurrence in semiconductor device junctions is the basis of the Esaki diode. The development reported in this report has proceeded on the assumption that no tunnelling occurs across the junction. The fact is that the importance of tunnelling increases as the impurity concentration increases into the upper part of the range with which we purport to deal. The effects of tunnelling on the present results are not significant for diffused silicon junctions [15], but should be considered for germanium junctions.

Second, the assumption that the quasi-Fermi levels are constant in the junction region allowed us to relate the splitting of the quasi-Fermi levels to the applied voltage. Sah's development [8] dealt with the special cases of a symmetric step junction and a linearly graded junction. The results for

forward biased junctions of either profile are equivalent in that the quasi-Fermi levels are predicted to be approximately constant in the space charge region. Sah's development, however, depends on the assumption of non-degeneracy, although he has suggested that the results are valid in general [15].

Despite the limitations imposed by the underlying assumptions concerning the density of states, the new equations developed in the interim report provide, in some practical instances of pn junction design, information superior to that supplied by conventional expressions. The usefulness of the new equations can be appreciated through the following reasoning.

Both the conventional and the new equations depend on these assumptions: negligible tunneling, negligible impurity concentration effects on the densities of states, and negligible variation of the quasi-Fermi levels in junction regions. The new equations, reviewed below, do not depend on the assumption of non-degeneracy whereas the convernional equations do. But the conventional equations are often used to make calculations in which the non-degeneracy assumption is violated. Hence the new equations are clearly more valid in these situations.

Equation (15), with (17) or (18), permits the calculation of the product of the number densities of charge carriers at any point in a semiconductor in equilibrium or with applied voltage. The evaluation is particularly easy at the edges of the space charge region of a pn junction. Also, if the depletion approximation is used to find the spatial variation of the edges of the allowed bands throughout the space charge region, Equation (15) allows the calculation of the np product in this region for use in recombination calculations. Figure 1 illustrates that the np product differs significantly from the conventional prediction at high impurity concentrations for voltages between zero and approximately 97% of the low injection voltage limit.

The position of the Fermi-level relative to the band edges may be calculated from (27) or (30) in n-type material and (28) or (31) in p-type material. Equations (27) and (28) indicate the dependence of the Fermi levels on the impurity concentration, the semiconductor material properties, and the impurity activation

energy. Equations (30) and (31) provide an auxiliary means of calculation. Figure 2 illustrates the predictions of (27) and (28) for boron or phosphorous doped silicon. The Fermi-level approaches the band edge with increasing impurity concentration as expected.

The contact potential of a pn junction is given by (41) or (44). Equation (41) shows that correction terms must be added to the conventional equation for use at high impurity concentrations. Equation (44) requires that the same energy differences be known as are needed in (41) but (44) provides for ease of calculation. Figure 3 shows the behavior predicted for junctions between boron and phosphorous doped silicon. Figure 4 illustrates the correction terms in (41) and thereby the errors inherent in using conventional equations , (42) or (43).

Equations (49) and (51) express low injection minority carrier densities at the edge of the space charge region. Figure 6 indicates that the predictions from (49) [and(51)] differ from those of the non-degenerate equation (50) at high impurity concentrations and at voltages near the low injection limit.

A quantitative definition of the voltage limit for low injection is given by (55) for injection into n-type material and by (56) for injection into p-type material. Figure 6 indicates the predictions of (55) by presenting qV_L' versus $(E_F' - E_C')_n$ with various values of F as a parameter. F is the parameter that defines the limit of low injection. The figure illustrates the expected result that the more injection one is willing to allow the more voltage can be applied.

Finally, the equations for current density due to electrons and holes are presented in (68) and (69). These equations have the same form as the non-degenerate equations but they have been derived by accounting for the dependence of the Einstein relation on impurity concentration.

8. COMMENT

It should be noted that, while the discussion has been cast in terms of

adjusting the relative Fermi-level position by varying the impurity concen-
trations, the results are valid for instances in which the Fermi-level is
caused to change due to a change in temperature. Specifically, the results
are applicable to semiconductor devices with high impurity concentrations at
low temperatures.

REFERENCES

[1] V. L. Bonch-Bruyevich, The Electronic Theory of Heavily Doped Semi-conductors, New York: American Elsevier Publishing Co., Inc., 1966.

[2] I. I. Ivanchik, "Toward the Theory of Degenerate p-n Junction," Soviet Physics - Solid State, Vol. 3, No. 1, July, 1961.

[3] R. D. Middlebrook, An Introduction to Junction Transistor Theory, New York: Wiley, 1957.

[4] A. K. Jonscher, Principles of Semiconductor Device Operation, New York: Wiley, 1960.

[5] Alvin B. Phillips, Transistor Engineering and Introduction to Integrated Semiconductor Circuits, New York: McGraw-Hill, 1962.

[6] J. S. Blakemore, Semiconductor Statistics, New York: MacMillan, 1962.

[7] W. Shockley, Electrons and Holes in Semiconductors, New York: John Wiley, 1951.

[8] C. T. Sah, "The Spatial Variation of the Quasi-Fermi Potentials in pn Junctions," IEEE Trans on Electron Devices, Vol. ED-13, pp. 839-846, December 1966.

[9] J. P. McKelvey, Solid-State and Semiconductor Physics, New York: Harper & Row, 1966.

[10] F. B. Hildebrand, Advanced Calculus for Applications, Englewood Cliffs, New Jersey: Prentice-Hall, 1962.

[11] S. S. Li and F. A. Lindholm, Proc. IEEE, in press.

[12] E. M. Conwell, "Impurity Band Conduction in Germanium and Silicon," Phys. Rev., 103, 1, 51 (1956).

[13] T. P. Brody, "Nature of the Valley Current in Tunnel Diodes," J. Appl Phys., 33, 1, 100-111 (Jan. 1962).

[14] T. N. Morgan, "Broadening of Impurity Bands in Heavily Doped Semiconductors," Phys. Rev., 139, 1A, A343-A348 (July 5, 1965).

[15] C. T. Sah, Private Communication

APPENDIX A

Figure 10 provides a reference diagram of the energy bands of a semi-conductor in the region near a pn junction. The list of symbols defines those used in the paper and the number in parenthesis indicates the equation in which the symbol is first found. Throughout the paper a superscript "prime" on energies indicates that the energies have been normalized by kT, i.e., $E' = \frac{E}{kT}$. Subscripts n or p denote quantities dealing with electrons or holes. The same subscripts, n and p, are used to denote quantities to be calculated on the n- or p-side of the junction. For example, $(E'_F - E'_C)_n$ means that the energy difference between the Fermi-level and the conduction band edge is to be calculated on the n-type side of the junction.

SYMBOLS

A^* defined in (B-1)

c   a fraction applied to the low injection voltage limit (57)

D   carrier diffusivity (58)

E   general energy (1)

E_A the energy of the acceptor level in the forbidden gap (28)

E_C the energy of the conduction band edge (3)

E_D the energy of the donor level in the forbidden gap (22)

E_F the Fermi-level (1)

E_{Fe} the quasi-Fermi level for electrons (12)

E_{Fh} the quasi-Fermi level for holes (13)

E_G the forbidden gap width $= E_C - E_V$ (14)

E_V the energy of the valence band edge (5)

ε_x the x-component of electric field (58)

F   defined in (52)

f(E)   the distribution function for electrons, the probability of an electron occupying a state at the energy E (1)

$\mathcal{F}_{1/2}$ the Fermi-Dirac integral of order 1/2 (6)

$\mathcal{F}_{-1/2}$ the Fermi-Dirac integral of order -1/2 (62)

g(E)   the quantum density of states at the energy E (4)

h   Planck's constant (3)

J   electrical current density (58)

K   defined in (15)

k   Boltzmann's constant (1)

m_C^* the density-of-states effective mass of electrons in the conduction band (3)

m_V^* the density-of-states effective mass of holes (5)

n   the number density of electrons in the conduction band (12)

n_1 the excess number density of electrons at the edge of the space charge region in p-type material $= n_p - n_{po}$ (51)

n_i the intrinsic number density of electrons (15)

N_A the number density of acceptor atoms (28)

N_C the effective density of states in the conduction band (6)

N_D the number density of donor atoms (22)

N_D^+ the number density of ionized donor atoms (21)

N_V the effective density of states in the valence band (11)

p the number density of holes (13)

p_1 the excess number density of holes at the edge of the space charge region in n-type material $= p_n - p_{no}$ (49)

q the magnitude of the electronic charge (14)

T the temperature in °K (1)

V general voltage (14)

V_D the contact potential of a pn junction (41)

V_L the low injection voltage limit (54)

α defined in (24)

β_C defined in (24)

β_D defined in (24)

μ carrier drift mobility (58)

APPENDIX B

CONSTANTS USED IN SAMPLE CALCULATIONS
(See Appendix A for Definition of Symbols)

$T = 300°K$

$q/kT = 38.685 \text{ ev}^{-1}$

$m_C^* = 1.08 \, m_o$ [6]

$m_V^* = 0.59 \, m_o$ [6]

$N_C = 2.816 \times 10^{13} \text{cm}^{-3}$

$N_V = 1.137 \times 10^{19} \text{cm}^{-3}$

$E_G' = 43.3 \text{ kT units } (1.12 \text{ ev})$ [6,9]

$E_C' - E_D' = 1.7408 \text{ kT units P in Si}$ [3]

$E_A' - E_V' = 1.7408 \text{ kT units B in Si}$ [3]

FIGURE CAPTIONS

Figure 1 The behavior of the np product at the edge of the space charge region of a step junction in silicon at 300°K as a function of the relative Fermi-level (impurity concentration) depicted as the ratio of equation (15) to the conventional expression, $np = n_i^2 \exp(qV')$. The development in Section V shows that this curve is applicable to cases where the applied voltage is less than approximately 97% of the voltage limit of low injection.

Figure 2 The behavior of the relative Fermi-level as a function of impurity concentration in phosphorous and boron doped silicon at 300°K.

Figure 3. The contact potential of a step junction (phosphorous-boron) in silicon at 300°K.

Figure 4. The magnitude of the correction terms for the contact potential of a step junction as a function of phosphorous and boron impurity concentration in silicon at 300°K. The "100% ionization" curve gives the amount by which the non-degenerate equation, $qV_D' = \ln[N_D N_A / n_i^2]$ overestimates the contact potential of a symmetric step junction. The remaining curves give the amount by which the non-degenerate equation $qV_D' = \ln[n_{no} p_{po} / n_i^2]$ underestimates the contact potential.

Figure 5. The carrier density versus impurity concentration for phosphorous and boron doped silicon at 300°K. The actual carrier densities are contrasted with the prediction based on the assumption of 100% ionization.

Figure 6. The voltage limit for low injection (holes into n-type silicon at 300°K) across a step junction versus the relative Fermi-level. The parameter F defines the low injection limit by $p_n = F n_{no}$.

Figure 7. The ratio of the voltage limit for low injection (of holes into n-type silicon) to the junction contact potential versus impurity concentration at 300°K.

Figure 8. The behavior of the minority carrier density (holes) at the edge of the space charge region of a step junction in silicon at 300°K as a function of the relative Fermi-level (impurity concentration) depicted as the ratio of equation (49) to the conventional equation $p_1 = p_{no} [\exp(qV') - 1]$. The parameter c is defined by $qV' = c q V_L'$. The solid curves are for F = 0.1 whereas the dotted curve is for F = 0.05.

Figure 9. The ratio of the np product at certain applied voltages to the equilibrium np product versus donor concentration. These curves show that the np product at the n-type edge of the space charge region in silicon does not depend significantly on the applied voltages up to approximately 0.97 V_L.

C. GENERATION AND RECOMBINATION NOISE IN SOLIDS (J. Salz)

1. INTRODUCTION

The noise behavior of solids has been extensively studied theoretically as well as experimentally. An excellent treatise of this subject and an extensive bibliograph can be found in reference (1). As may be expected the theoretical approach to this problem must be statistical since noise by definition is a stochastic process. In this report we treat generation-recombination noise from a fresh mathematical point of view. Here we restrict the analysis to homogeneous materials and consequently our descriptive statistical parameters will be independent of spatial coordinates. We focus attention on the most important parameters of the noise such as the mean value, mean-square, covariance and spectral density.

As discussed in reference (1) the characteristics of the noise in homogeneous solids can be completely determined by the statistical behavior of a vector stochastic process $\overline{V}(t) = (v_1(t), v_2(t) \ldots v_N(t)$ whose components represent the number of carriers at time t in energy level E_j, j = 1, 2 . . . N respectively subject to the constraint that Σv_j is fixed.

In previous treatments of this problem it was assumed that the vector stochastic process $\overline{V}(t)$ is Markovian. This assumption opens up a whole body of mathematical works devoted to the study of Markov processes. In particular the theory of Fokker and Planck (2), (3) is most applicable and the derivations of the noise statistics under these assumptions reduce to the calculation of various conditional moments.

Our approach is more direct. We attack the problem by evaluating partial derivatives of the characteristic function for the vector stochastic process from which we extract systems of differential equations in the desired statistical parameters. Our results then, are solutions to linear state-equations. It appears that our approach has greater applicability and

is not restricted to only Markov processes. It has however been observed (4) that even the Fokker-Planck-Kolmogorov equations appear to be of wider applicability than just to Markov processes.

In Section I we define the problem and describe the mathematical model. In Section II we derive the covariance and the spectral density matrices while in Section III we apply the general results to a specific situation.

2. THE MATHEMATICAL MODEL

Our basic objective in this report is to derive formulas for the pertinent statistics of generation-recombination noise arising in homogeneous solids. Our aim then, is first to formulate a phenomenological model based on fundamental physical concepts and then to analyze this model. A most useful statistical function that can be empirically determined is the spectral density of the noise. This function describes the distribution of the average power as a function of frequency. The area under this curve gives the total average noise power -- a most fundamental parameter of devices. Another important statistical function associated with noise is the correlation function which, as will be seen, is related to the spectral density by Fourier transformation. We shall be principally interested in deriving formulas for these functions in terms of fundamental properties of solids.

Our working physical model is the following: A dc voltage is applied to a sample of homogeneous-solid. As a result a current $I_o(t)$ can be observed. We presume this current to be modeled as a stochastic process. The random aspects arise from carrier fluctuations. The current flowing in this circuit is assumed to be given by a linear combination of more elementary counting processes as:

$$I_o(t) = \sum_{n=1}^{N} a_n v_n(t) \tag{1}$$

where the a_n's are constants determined by fundamental parameters of the material such as mobilities, carrier charges and applied potential. The set of functions $v_n(t)$, $n = 1, 2 \ldots N$ represent the number of carriers at time t associated with corresponding energy levels E_n, $n = 1, 2 \ldots N$. These functions are counting stochastic processes whose differentials Δv_n, $n = 1, 2 \ldots N$ can take on only ± 1 or 0. The statistics associated with these increments completely determine the behavior of $I_o(t)$. For instance, the average value of $I_o(t)$ is

$$\langle I_o(t) \rangle = \sum_n a_n \langle v_n(t) \rangle \tag{2}$$

where $\langle \, . \, \rangle$ denotes the ensemble average. The fluctuating portion of $I_o(t)$ is

$$I(t) = I_o(t) - \langle I(t) \rangle \tag{3}$$

and the total average noise power is

$$\sigma^2 = \langle I^2(t) \rangle \tag{4}$$

In the next section we shall evaluate these averages more explicitly

The spectral density of $I(t)$, or the spectrum is defined (5) as

$$F(\omega) = \lim_{T \to \infty} \frac{1}{2T} \langle |W_T(\omega)|^2 \rangle \tag{5}$$

where $W_T(\omega) = \displaystyle\int_{-T}^{T} I(t) \, e^{-i\omega t} \, dt$. In terms of the original process (2)

$$\langle |W_T(\omega)|^2 \rangle = \sum_{n,m} a_n a_m \langle \Lambda_n(\omega, t) \Lambda_m^*(\omega, t) \rangle$$

where $\Lambda_n(\omega, t) = \displaystyle\int_{-T}^{T} U_n(t) \, e^{-i\omega t} \, dt$ with $U_n(t) = v_n(t) - \langle v_n(t) \rangle$

and * denotes the complex conjugate. Thus we see that the spectrum of $I(t)$ is given by a quadratic form.

$$\mathbf{F}(\omega) = \overline{A} \; \tilde{G}(\omega) \; \overline{A}^T \tag{6}$$

where the vector $\overline{A} = (a_1 - - - a_n)$, $\overline{A}^T$ denotes the transpose of $\overline{A}$, and $\tilde{G}(\omega)$ is an NxN matrix with elements $G_{nm}(\omega)$ given by

$$G_{nm}(\omega) = \lim_{T \to \infty} \frac{1}{2T} \, \langle \Lambda_n(\omega, T) \, \Lambda^*_m(\omega, T) \rangle \tag{7}$$

Eqn. (7) can also be obtained by the Fourier transform of the correlation coefficients[+]

$$R_{nm}(\tau) = \langle U_n(t) \, U_m(t+\tau) \rangle \tag{8}$$

To see how this is done write Eqn. (7) as

$$G_{nm}(\omega) = \lim_{T \to \infty} \frac{1}{2T} \int_{-T}^{T} \int_{-T}^{T} e^{i\omega(t'-t)} \langle U_n(t) \, U_m(t') \rangle dt \, dt'$$

$$= \lim_{T \to \infty} \frac{1}{2T} \int_{-T}^{T} \int_{-T}^{T} R_{nm}(t-t') \, e^{i\omega(t'-t)} \, dt' \, dt$$

$$= \lim_{T \to \infty} \frac{1}{2T} \left[\int_{0}^{2T} (T-x) \, R_{nm}(x) \, e^{i\omega x} \, dx - \int_{0}^{2T} (x-T) \, R_{nm}(-x) \, e^{i\omega x} dx \right]$$

+ We assume that the stochastic processes $U_n(t)$, $n = 1 \ldots N$ are ergodic

$$= \int_0^\infty [R_{nm}(x) \ e^{i\omega x} + R_{nm}(-x) \ e^{i\omega x}] \ dx \qquad (9)$$

Using matrix notation we can express (9) in a compact form.

$$\tilde{G}(\omega) = \text{Re}\left\{\int_0^\infty [\tilde{R}(x) \ e^{i\omega x} + \tilde{R}^T(x) \ e^{-i\omega x}] \ dx\right\} \qquad (10)$$

where $\tilde{R}(x)$ is the covariance matrix with elements $R_{nm}(x)$. In (10) we used the fact that $\tilde{R}(-x) = \tilde{R}^T(x)$. This can be established by noting that for stationary processes

$$R_{nm}(x) = \langle U_n(o) \ U_m(x) \rangle$$

$$= \langle U_n(-x) \ U_m(o) \rangle$$

$$= \langle U_m(o) \ U_n(-x) \rangle = R_{mn}(-x) \qquad (11)$$

The "real" part in (10) must be taken since both $\tilde{G}(\omega)$ and $\tilde{R}(x)$ are real matrices.

In the next section we shall derive in detail the form of the covariance and the spectral density matrices.

3. THE COVARIANCE AND THE SPECTRAL DENSITY MATRICES

The covariance matrix of a zero-mean vector stochastic process is defined as

$$\tilde{R}(t_1, t_2) = \langle \overline{U}^T(t_1) \, \overline{U}(t_2) \rangle \qquad (12)$$

When the process is stationary (12) becomes

$$\tilde{R}(t) = \langle \overline{U}^T(o) \, \overline{U}(t) \rangle \qquad (13)$$

where $t = t_2 - t_1$. Making use of the sub-conditioning[+] property of expectations we can write (13) as

$$\tilde{R}(t) = \langle \overline{U}^T(o) \, E\{\overline{U}(t) \mid \overline{U}(o)\} \rangle \qquad (14)$$

where $E\{\cdot \mid \}$ denotes conditional expectation.

We shall now derive a differential equation for the conditional mean-vector $E\{\overline{U}(t) \mid \overline{U}(o)\}$ through its characteristic function. In what follows we shall work with the original vector process $\overline{V}(t) = (v_1(t), v_2(t) \ldots v_N(t)$ defined in Eqn. (1). Recall that $\overline{U}(t) = \overline{V}(t) - \langle \overline{V}(t) \rangle$.

For the $\overline{V}$ process the conditional characteristic function is defined as

$$C(\omega, t) = E\{\exp \overline{i\omega}\overline{V}(t) \mid V_o\} \qquad (15)$$

where $\overline{\omega} = (\omega_1 \ldots \omega_N)$ and $\overline{V}_o = \overline{V}(o)$. The partial derivative of C with respect to t is interpreted in the following manner

---

+ The sub-conditioning property of expectations is simply a statement of the fact that averages can be carried out by first computing a conditional average and then averaging with respect to the conditioned variables.

$$\frac{\partial C}{\partial t} = \lim_{\delta \to o} \frac{1}{\delta} E \left\{ e^{i\bar{\omega}\bar{V}^T(t+\delta)} - e^{i\bar{\omega}\bar{V}^T(t)} \mid \bar{V}_o \right\}$$

$$= \lim_{\delta \to o} \frac{1}{\delta} E \left\{ e^{i\bar{\omega}V^T(t)} [e^{i\bar{\omega}\Delta\bar{V}^T(t)} - 1] \mid \bar{V}_o \right\} \qquad (15)$$

where $\Delta\bar{V}(t) = \bar{V}(t+\delta) - \bar{V}(t)$ and, we assume that the above limit exists. By again invoking the sub-conditioning property of expectations, we can put (15) into the form

$$\frac{\partial C}{\partial t} = \lim_{\delta \to o} \frac{1}{\delta} E \left\{ e^{i\bar{\omega}\bar{V}^T(t)} E \left\{ e^{i\bar{\omega}\Delta\bar{V}^T(t)} - 1 \mid \bar{V}_o, \bar{V}(t) \right\} \mid V_o \right\} \qquad (16)$$

We now focus attention on the inner-conditional expectation.

$$E \left\{ e^{i\bar{\omega}\Delta\bar{V}^T(t)} - 1 \mid \bar{V}_o, \bar{V}(t) \right\}$$

$$= \int \cdots \int [e^{i\bar{\omega}\Delta\bar{V}^T(t)} - 1] P(\Delta\bar{V} \mid \bar{V}_o, \bar{V}(t)) \, d(\Delta\bar{V}) \qquad (17)$$

where $P(\cdot \mid)$ is the conditional probability density of $\Delta\bar{V}$.

Since the components of the process $\bar{V}(t)$ can change only by one unit at any t, the incremental components $\Delta v_j(t)$, $j = 1, 2 \ldots N$ can assume only the three possible values 1, -1, or 0. It is reasonable to assume that the vector increment $\Delta\bar{V}(t)$ conditioned on $\bar{V}(t)$ and $\bar{V}(o)$ does not depend on both the process at time t and an earlier time t = o. This essentially presumes that the process $\bar{V}(t)$ is Markovian. As a consequence, therefore,

$$P(\Delta\bar{V}(t) \mid \bar{V}_o, \bar{V}(t)) = P(\Delta\bar{V}(t) \mid \bar{V}(t)) \qquad (18)$$

We now define the following probabilities

$$P_r \left[\Delta \overline{V}(t') = \overline{A}_k \mid \overline{V}(t'), \ t' \epsilon [t, \ t+\delta] \right] = g_k(\overline{V}(t)) \delta \qquad (19)$$

where $\overline{A}_k = (a_{kj} \cdots a_{kN})$ and $a_{k\ell}$ is either 1, -1 or o, k, j = 1, ... N. A typical $\overline{A}_k$ vector might look like (1, 1, - 1, 0, 0, 1, . . . 1). There can be at most $K = 3^n$ such vectors but because of physical constrains the permissible number of vectors may be less. The scalar functions $g_k(\overline{V})$ are the probabilities per unit time that the increment $\Delta \overline{V}$ given $\overline{V}$ takes on the vector $\overline{A}_k$. Upon substituting (19) into (17) we obtain

$$E \left\{ e^{i\overline{\omega} \, \Delta \overline{V}} - 1 \mid \overline{V}(t) \right\} = \sum_k g_k(\overline{V}) \left[e^{i\overline{\omega} \, \overline{A}_k^T} - 1 \right] \delta \qquad (20)$$

and the basic equation (16) becomes

$$\frac{\partial C}{\partial t} = \sum_k \left[e^{i\overline{\omega} \, \overline{A}_k^T} - 1 \right] E \left\{ e^{i\overline{\omega} \, \overline{V}^T(t)} g_k(\overline{V}) \mid \overline{V}_o \right\} \qquad (21)$$

We now derive the conditional mean of $\overline{V}$ needed in the evaluation of the co-variance matrix.

Towards this and let

$$m_\ell(t) = E \left\{ v_\ell(t) \mid \overline{V}_o \right\} = -i \frac{\partial C}{\partial \omega_\ell} \Big|_{\overline{\omega} = o} \ , \ \ell = 1, 2 \ldots . N$$

From Eqn. (11) we obtain

$$\frac{\partial m_\ell(t)}{\partial t} = \sum_k a_{k\ell} E \left\{ g_k(\overline{V}) \mid \overline{V}_o \right\}$$

$$= E \left\{ \sum_k a_{k\ell} \, g_k(\overline{V}) \mid \overline{V}_o \right\}$$

$$= E \left\{ f_\ell(\overline{V}) \mid \overline{V}_o \right\} , \ \ell = 1, 2 \ldots . N$$

where

$$f_\ell(\overline{V}) = \sum_k a_{k\ell} g_k(\overline{V})$$

In order to make further progress we approximate $f_\ell(\overline{V})$ by the linear form

$$f_\ell(\overline{V}) \sim f_\ell(\overline{N}_o) + \sum_{n=1}^{N} \frac{\partial f_\ell(\overline{N}_o)}{\partial v_m} (v_m - N_{om}) \qquad (24)$$

where

$$\overline{N}_o = <\overline{V}(t)> = (N_{o1}, N_{o2} \cdots N_{oN})$$

is the steady-state mean vector. The mean vector components $N_{o\ell}$ can also be obtained from

$$N_{o\ell} = \lim_{t \to \infty} m_\ell(t), \quad \ell = 1, 2 \cdots N. \qquad (25)$$

When we substitute (24) into (23) we obtain

$$\frac{\partial m_\ell}{\partial t} = f_\ell(\overline{N}_o) + \sum_{m=1}^{N} \frac{\partial f_\ell(\overline{N}_o)}{\partial v_m} E\{ v_m - N_{om} \mid \overline{V}_o \} \qquad (26)$$

By taking the limit as $t \to \infty$ on both sides of (26) we conclude that

$$f_\ell(\overline{N}_o) = 0, \quad \ell = 1, 2 \cdots N \qquad (27)$$

since

$$\lim_{t \to \infty} E\{ v_m - N_{om} \mid \overline{V}_o \} = 0$$

Because N_{on}, $n = 1, 2 \cdots N$ does not depend on time we can write (26) in the form

$$\frac{\partial U_\ell}{\partial t} = \sum_{m=1}^{N} b_{\ell m} U_m, \quad \ell = 1, 2 \cdots N \qquad (28)$$

where

$$U_\ell = F \{ v_\ell - N_{o\ell} \mid V_o \}$$

and

$$b_{\ell m} = - \frac{\partial f_\ell (\overline{V})}{\partial v_m} \bigg|_{\overline{V} = \overline{N}_o}$$

A more compact representation of (28) is possible by making the following observations. Define the conditional mean vector by

$$\overline{M}(t) = E \{ \overline{U}(t) \mid \overline{U}(o) \} \qquad (29)$$

whose elements are $U_n(t)$, $n = 1, 2 \ldots N$. Furthermore define the matrix $\tilde{F}$ whose elements are $b_{\ell m}$, then we can write (28) as

$$\frac{d\overline{M}(t)}{dt} = - \overline{M}(t) \tilde{F} \qquad (30)$$

Post multiplying (14) by $\tilde{F}$ we obtain

$$\tilde{R}(t)\tilde{F} = \langle \overline{V}^T(o) \overline{M}(t) \tilde{F} \rangle$$

$$\qquad (31)$$

$$= - \langle \overline{V}^T(o) \frac{d\overline{M}(t)}{dt} \rangle$$

$$= - \frac{d}{dt} \langle \overline{V}^T(o) \overline{M}(t) \rangle$$

By undoing the sub-conditions in (31) we obtain the desired state-differential equation in $\tilde{R}(t)$ as

$$\frac{d\tilde{R}(t)}{dt} = - \tilde{R}(t) \tilde{F} \qquad (32)$$

with the well known solution

$$\tilde{R}(t) = \tilde{R}(o) e^{-\tilde{F}t} \qquad (33)$$

For a complete specification of the covariance matrix we need $\tilde{R}(o)$ – the steady-state variance matrix. This matrix can be obtained by evaluating second derivatives of the characteristic function as follows. Observe that

$$\frac{\partial^2 C}{\partial \omega_\ell \omega_s}\bigg|_{\overline{\omega}\,=\,o} = E\{v_\ell(t)\,v_s(t)\,|\overline{V}_o\} = \lambda_{\ell s}, \quad \ell,\,s = 1,\,2\,\ldots\,N \quad (34)$$

By twice differentiating Eqn. (21) and evaluating the result at $\overline{\omega} = o$, we obtain

$$\frac{\partial \lambda_{\ell s}}{\partial t} = \sum_k \{a_{ks}\,E\{v_\ell g_k(\overline{v})\,|\,\overline{V}_o\}$$

$$+ a_{k\ell}\,E\{v_s\,g_k(\overline{v})\,|\,\overline{V}_o\}$$

$$+ a_{k\ell}\,a_{ks}\,E\{g_k(\overline{v})|\overline{V}_o\} \quad (35)$$

$$= E\{v_\ell f_s(\overline{v})\,|\overline{V}_o\} + E\{v_s\,f_\ell(\overline{v})|\,\overline{V}_o\}$$

$$+ \sum_k a_{k\ell}\,a_{ks}\,E\{g_k(\overline{v})\,|\,\overline{V}_o\}, \quad \ell,\,s = 1,\,2\,\ldots\,N$$

Making use of (24) we find that

$$E\{v_\ell f_s(\overline{v})\,|\overline{V}_o\} \quad (36)$$

$$= -E\{v_\ell \sum_m b_{sm}(v_m - N_{om})\,|\,\overline{V}_o\}$$

and

$$E\{v_s\,f_\ell(\overline{v})\,|\overline{V}_o\} \quad (37)$$

$$= -E\{v_s\,\sum_m b_{\ell m}\,(v_m - N_{om})\,|\,\overline{V}_o\}$$

Since we are only interested in the steady-state situation, the left-hand side of Eqn. (35) can be set to zero. ($\lambda_{\ell s}$ cannot depend on time because of stationerity.) Also, the conditional averages on the right side become ordinary expectations which do not depend on $\overline{V}_o$. Thus we obtain from (35) with the use of (36) and (37) the relationship

$$\sum_m b_{sm} <U_m U_\ell> + \sum_m b_{\ell m} <U_m U_s>$$

$$= \sum_m a_{m\ell} a_{ms} <g_m(\overline{V})>, \quad \ell, s = 1, 2 \ldots N \tag{38}$$

Upon approximating $g_m(\overline{V})$ by

$$g_m(\overline{V}) = g_m(\overline{N}_o) + \sum_{q=1}^{N} \frac{\partial g_m(\overline{N}_o)}{\partial v_q} (v_q - N_{oq}) \tag{39}$$

we obtain from (38) the matrix equation

$$\tilde{C} = \tilde{F}\tilde{R}(o) + \tilde{R}(o)\tilde{F}^T \tag{40}$$

where $\tilde{C}$ is an NxN matrix with elements

$$c_{\ell s} = \sum_m a_{m\ell} a_{ms} g_m(\overline{N}_o) \tag{41}$$

and the elements[+] of $\tilde{R}(o)$ are clearly $<U_m U_\ell>$. To obtain $\tilde{R}(o)$ explicitly we must solve Eqn. (40). As it turns out the spectral density matrix involves the matrix $\tilde{C}$ only and therefore we shall not attempt to solve (40).

The calculation of the spectral density matrix is now straightforward.

+ The transpose of $\tilde{R}(o)$ is equal to itself.

from Eqn. (10)

$$\tilde{G}(\omega) = \int_0^\infty [\tilde{R}(t) + \tilde{R}^T(t)] \cos \omega t \, dt$$

Using (33) in (42) we obtain

$$\tilde{G}(\omega) = \mathrm{Re} \left\{ \int_0^\infty \tilde{R}(o) \, e^{-\tilde{F}t + i\omega t} \, dt \right.$$

$$\left. + \int_0^\infty e^{-\tilde{F}^T t - i\omega t} \tilde{R}(o) \, dt \right\} \tag{43}$$

$$= \mathrm{Re} \left\{ \tilde{R}(o) \, [\tilde{F} - i\omega I]^{-1} + [\tilde{F}^T + i\omega I]^{-1} \tilde{R}(o) \right\}$$

where $[\cdot]^{-1}$ denotes the inverse and I denotes the identity matrix. Since $\tilde{G}(\omega)$ is symmetric we can put (43) in the simple form

$$\tilde{G}(\omega) = \mathrm{Re} \left\{ [\tilde{F}^T + i\omega I]^{-1} [(\tilde{F}^T + i\omega I) \tilde{R}(o) + \tilde{R}(o) (\tilde{F} - i\omega I)] [\tilde{F} - i\omega I]^{-1} \right\}$$

$$= \mathrm{Re} \left\{ (\tilde{F}^T + i\omega I)^{-1} [\tilde{F}^T \tilde{R}(o) + \tilde{R}(o) \tilde{F}] (\tilde{F} - i\omega I)^{-1} \right. \tag{44}$$

$$= \mathrm{Re} \left\{ (\tilde{F}^T + i\omega I)^{-1} \tilde{C} (\tilde{F} - i\omega I)^{-1} \right.$$

where $\tilde{C} = \tilde{F}^T \tilde{R}(o) + \tilde{R}(o) \tilde{F}$ is a symmetric matrix given in Eqn. (40).

We now wish to represent $\tilde{G}(\omega)$ in normal-modes, i.e., in terms of the various corner-frequencies. This can best be accomplished by diagonalizing $\tilde{F}$. Now, we suppose that $\tilde{F}$ has real[+] eigenvalues $\lambda_\ell, \ell = 1, 2 \ldots N$ and let

$$\tilde{F} = \tilde{Q}^{-1} D \tilde{Q} \tag{45}$$

+ As will be apparent later these conditions must be satisfied in order for the mathematics to make physical sense.

-200-

where D is a diagonal matrix with elements λ_ℓ, $\ell = 1, 2 \ldots N$. Using this representation for $\tilde{F}$ puts 44 in the form

$$\tilde{G}(\omega) = \text{Re } \{\tilde{Q}^{-1} (D + i\omega I)^{-1} \tilde{W} (D - i\omega I)^{-1}\}\tilde{Q}^{-T}$$

(46)

$$= \frac{1}{2} \tilde{Q}^{-1} \{L(\omega) \tilde{W} L(-\omega) + L(-\omega) \tilde{W} L(\omega) \} \tilde{Q}^{-T}$$

where

$$\tilde{W} = \tilde{Q} \tilde{C} Q^T, \quad L(\omega) = (D + i\omega I)^{-1}$$

and $\tilde{Q}^{-T}$ is the inverse-transpose matrix. Since $\tilde{W}$ is a symmetric matrix we find that the elements of the matrix

$$\tilde{H} = \frac{1}{2} L(\omega) \tilde{W} L(-\omega) + \frac{1}{2} L(-\omega) \tilde{W} {}_{L}(\omega)$$

(47)

can be represented by

$$h_{ij} = \frac{W_{ij}(\lambda_i\lambda_j + {}^2)}{(\lambda_i^2 + \omega^2) (\lambda_j^2 + \omega^2)}$$

(48)

$$\approx \frac{W_{ij}}{\lambda_i + \lambda_s} \left[\frac{\lambda_i}{\lambda_i^2 + \omega^2} + \frac{\lambda_i}{\lambda_j^2 + \omega^2} \right]$$

and W_{ij}'s are the elements of $\tilde{W}$. Now if we let the elements of $\tilde{Q}^{-T}$ be q_{ij}^{-T}, the elements, α_{ij} of the matrix $\tilde{H} Q^{-T}$ are

$$\alpha_{ij} = \sum_{k} h_{ik} q_{kj}^{-T}$$

(49)

and therefore the elements of the spectral density matrix in normal modes become

$$G_{nm}(\omega) = \sum_{s} q_{ns}^{-} q_{sr}^{-}$$

$$= \sum_{s} \sum_{k} h_{nk} q_{sk}^{-} q_{sm}^{-}$$

(50)

$$= \sum_{k} h_{nk} r_{km}$$

-201-

where q^-_{ij} are the elements of the matrix $\bar{Q}^{-1}$ and

$$r_{km} = \sum_s q^-_{sk} \, q^-_{sm} \tag{51}$$

when we substitute (48) into (50) we obtain finally the canonical represen-

tation of the matrix elements $G_{nm}(\omega)$ as

where

$$G_{nm}(\omega) = \sum_{s=1}^{N} (q^-_{ns} \, \beta_{sm} + q^-_{ms} \, \beta_{sn}) \, \frac{\lambda_s}{\lambda_s^2 + \omega^2}$$

$$\beta_{sn} = \sum_k \frac{W_{ks}}{\lambda_k + \lambda_s} \, q^-_{nk} \tag{52}$$

In the forthcoming section we shall apply these results to a special

case.

4. NOISE STATISTICS IN A TWO-LEVEL SEMICONDUCTOR

Noise in a semiconductor may be regarded as arising from carrier tran-

sitions that occur between two energy levels, e.g., the conduction band and

a set of impurity levels. Because the number of charge carriers is conserved

we need only consider a single counting stochastic process $v(t)$.

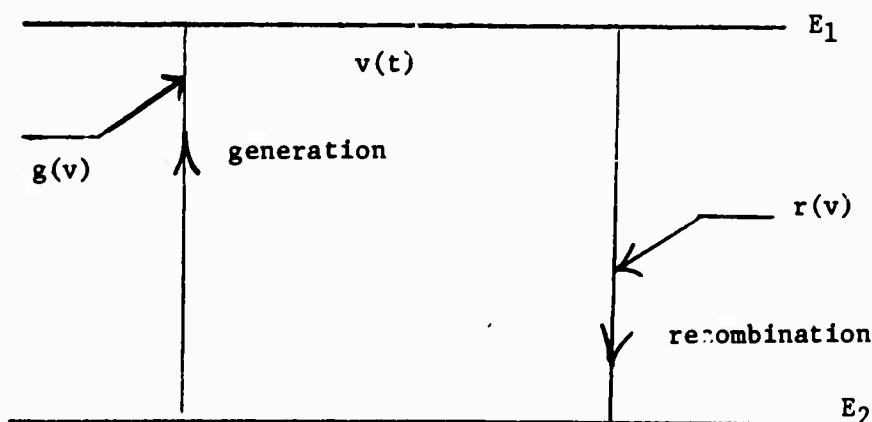Fig. 1 shows a schematic representation of the given situation.

Fig. 1 Two-level system

In this application the vectors $\overline{A}_k$ in (19) are one-dimensional, taking on the values 1, -1 and 0. Their respective probabilities are

$$P_r[\Delta v(t') = 1 \mid v(t'); \ t' \epsilon \ [t, \ t + \delta] \ ] \ = \ r(v) \ \delta$$

$$P_r[\Delta v(t') = 1 \mid v(t'); \ t' \ [t, \ t + \delta] \ ] = g(v) \ \delta \qquad (53)$$

$$P_r[\Delta v(t') = o \mid v(t'); \ t' \epsilon \ [t, \ t + \delta] \ ] = (1 - r(v) - g(v))\delta$$

From Eqn. (23) and (24) with $\ell = 1$, $N = 1$ we obtain

$$
\begin{aligned}
f_1(v) \quad &= r(v) - g(r) \\
&\sim r(N_o) - g(N_o) + \left(\frac{dr(v)}{\partial v} - \frac{dg(v)}{dv} \right) \Bigg|_{v=N_o} (v-N_o)
\end{aligned}
\qquad (54)
$$

where $N_o = \ <v(t)> \ .$

An important result from (27) is that

$$r(N_o) \ = \ g(N_o) \qquad (55)$$

from which N_o may be determined.

Observe that in this application, $\tilde{F}$ has only one element and is therefore a scalar equal to

$$
\begin{aligned}
b &= \ \frac{\partial f_1(v)}{\partial v} \ \Bigg| \ v = N_o \qquad (56) \\
&= \ g'(N_o) - r'(N_o)
\end{aligned}
$$

where the prime denotes differentiation. The covariance function now is simply

$$
\begin{aligned}
R(t) \ &= \ <v(o) \ v(t)> \\
&= \ R(o) \ e^{-b|t|}
\end{aligned}
\qquad (57)
$$

Solving Eqn. (40) for R(o) now yields

$$R(o) = \frac{gN_o}{r'(N_o) - g'(N_o)} \tag{58}$$

The Fourier transfer of (57), which is the spectral density, is simply

$$G(\omega) = \frac{2 \, g(N_o)}{b^2 + \omega^2} \tag{59}$$

REFERENCES

1. K. M. Van Vliet and J. R. Fassett, "Fluctuations Due to Electronic Transitions and Transport in Solids," Chapter 7 in <u>Fluctuation Phenomenon in Solids</u>, Edited by R. E. Burgess, Academic Press, N. Y., 1965.

2. R. L. Stratonovich, <u>Topics in the Theory of Random Noise</u>, Vol. 1, N. Y. Gordon and Bresch, 1963.

3. Nelson Wax Ed. "Selected Papers on Noise and Stochastic Processes," Dover Publications, Inc., N. Y.

4. Terrence Fine, "Partial Differential Equations for Densities of Random Processes," Tech. Report No. 445, May 1964, Cruft Laboratories, Harvard University.

5. S. O. Rice, "Mathematical Analysis of Random Noise," <u>Bell System Tech. J.</u> 42, 1944.

D. LOW FREQUENCY NOISE IN INTEGRATED CIRCUIT TRANSISTORS (E. R. Chenette, A. J. Brodersen, R. C. Jaeger)

The low frequency noise performance of all semiconductor devices is dominated by sources of excess noise with a spectral density which varies approximately as 1/f. Although much work has been done in the study of this 1/f noise it remains an unsolved problem[1]. It is impossible, at the present time, to predict the 1/f noise performance of a bipolar transistor (or that of any other semiconductor device) on the basis of a knowledge of device and circuit parameters. At higher frequencies where the sources of 1/f noise are negligible, it is possible to predict noise performance with precision for a wide range of operating conditions.

Recently progress has been made in relating the 1/f noise observed in MOS field-effect transistors to the surface charge density[2]. Earlier experimental studies have shown that a major source of 1/f noise in otherwise well-behaved low-noise bipolar transistors is related to fluctuations in the surface recombination velocity near the emitter base transition region[3,4,5,6]. It has been shown that controlling the surface potential near the emitter-base transition region of a planar transistor can effect the surface recombination rate and hence the d.c. current gain. It is reasonable to expect that this control of the surface potential must also effect the 1/f noise since this excess noise in these otherwise well-behaved transistors is proportional to the recombination current (base current).

The brief discussion which follows gives a summary of some of the preliminary work being done to better understand this problem. The results of some preliminary measurements of noise in integrated circuit transistors will be presented. Equivalent circuits describing the noise performance of transistors in the 1/f noise region are compared.

1. MEASUREMENT OF LOW FREQUENCY NOISE IN INTEGRATED CIRCUIT TRANSISTORS

Preliminary measurements have been made of the equivalent noise resistance of several types of planar transistors. The measurements are made as a function of frequency with operating point, source resistance and environment as parameter. The CA 3018 has been a convenient source of typical integrated circuit planar transistors for these early measurements. For comparison, measurements were also made on low noise 2N930 planar transistors. Special transistors pairs with carefully matched geometries and including field plates for control of surface potential are being fabricated in our laboratory for additional study.

Figures 1 and 2 show the results of some of these measurements. As discussed below, these results are in agreement with the expected behavior. At this point they serve mainly to build confidence in our measurement technique and the operation of the spectrum analyzers.

The most significant feature noticed to this point is considered to be the small spread in the magnitude of the noise in this 1/f noise region. This is in contrast to results reported earlier of large variations in noise from transistor to transistor even of the same type. It is hoped that this uniformity is an indication that a well-defined cause for the apparent modulation of the surface recombination rate may soon be identified.

2. COMPANION OF LOW-FREQUENCY NOISE EQUIVALENT CIRCUITS

Figure 3 shows three different noise equivalent circuits which have been used to describe the noise performance of bipolar transistors when flicker noise or 1/f noise predominates. Figures 3A and 3B are basically common-base T-equivalent circuits. 3A shows two flicker noise current generators; i_{f1},

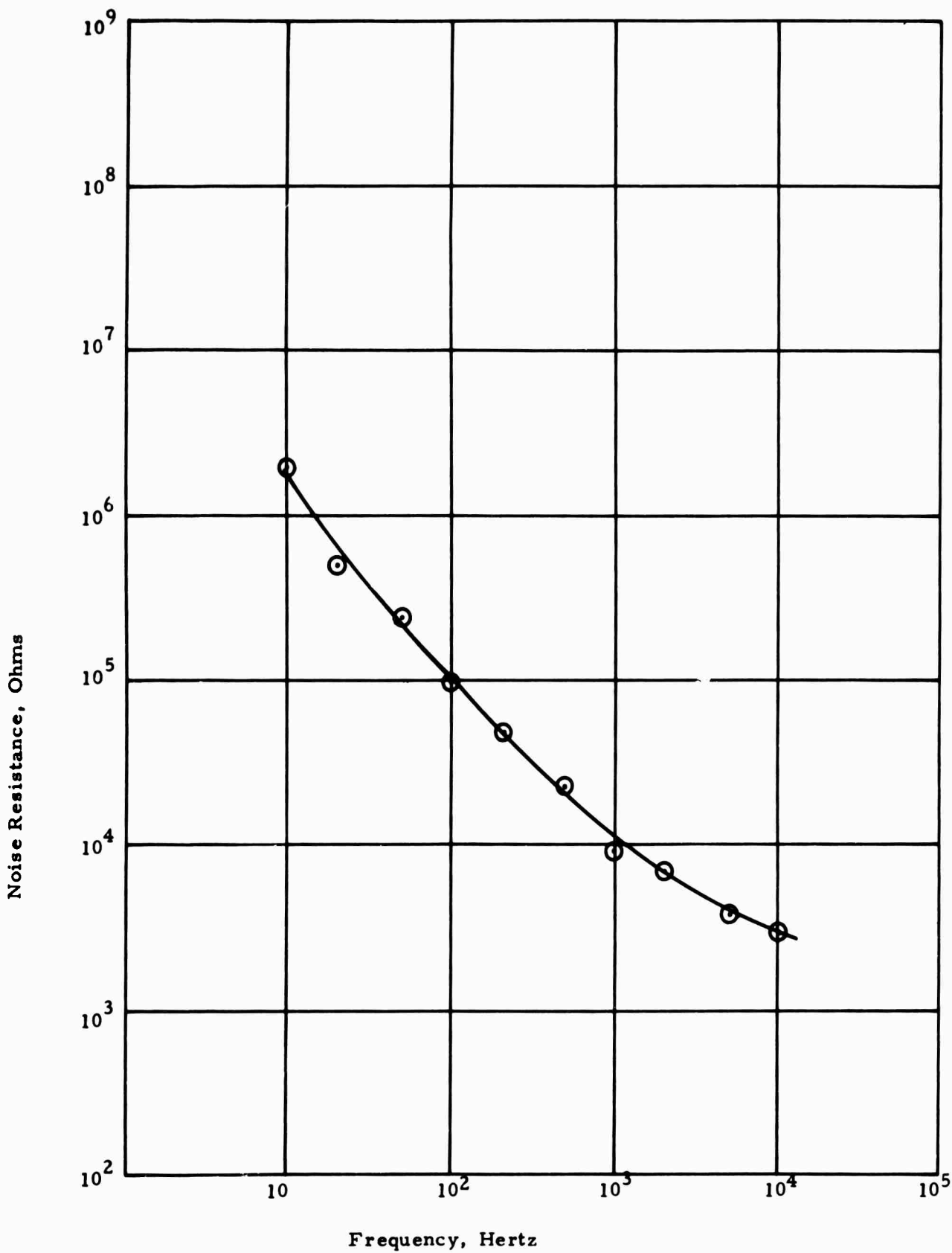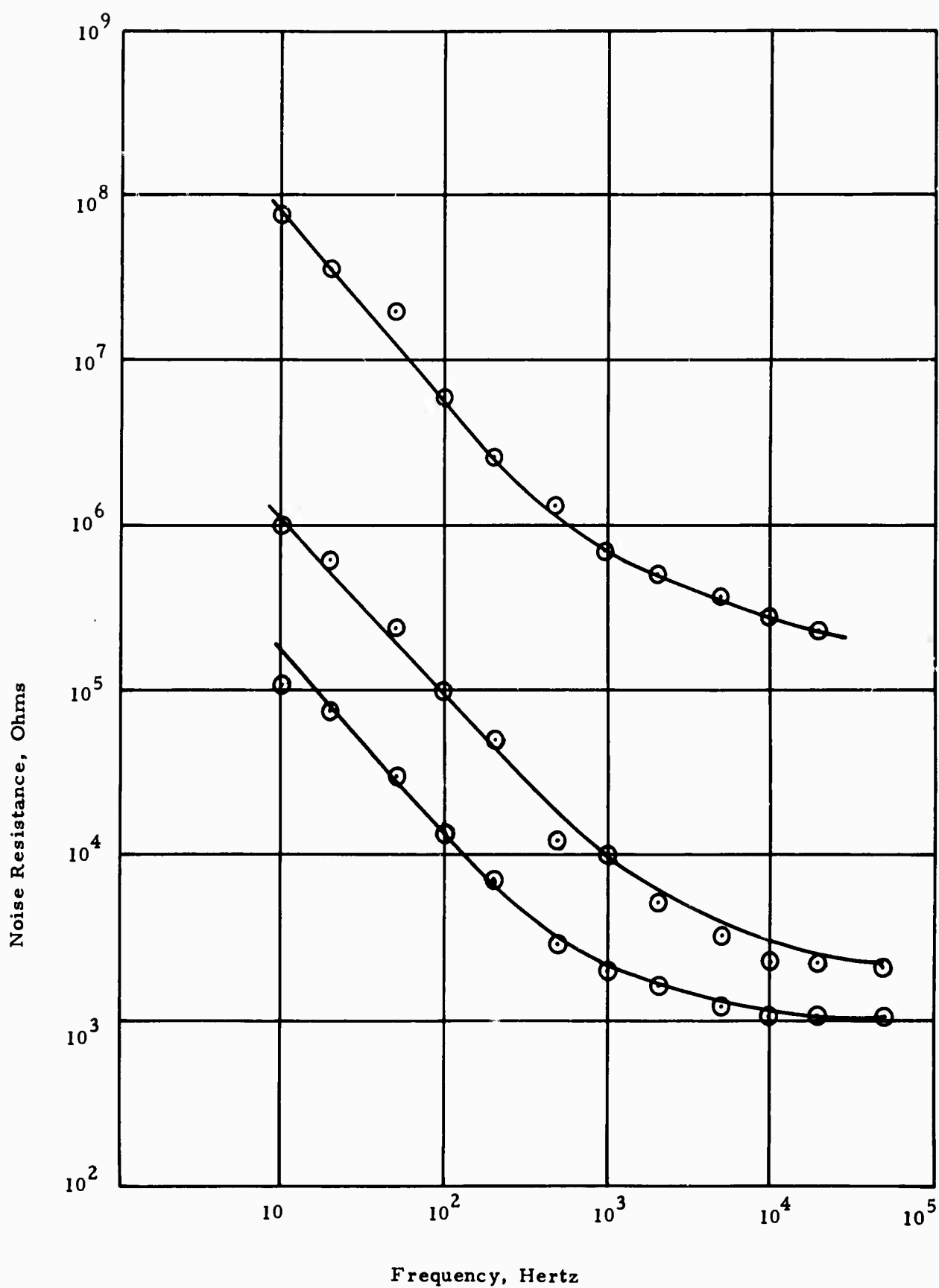FIGURE 1: Noise Resistance of Typical Integrated Circuit
Bipolar Transistors

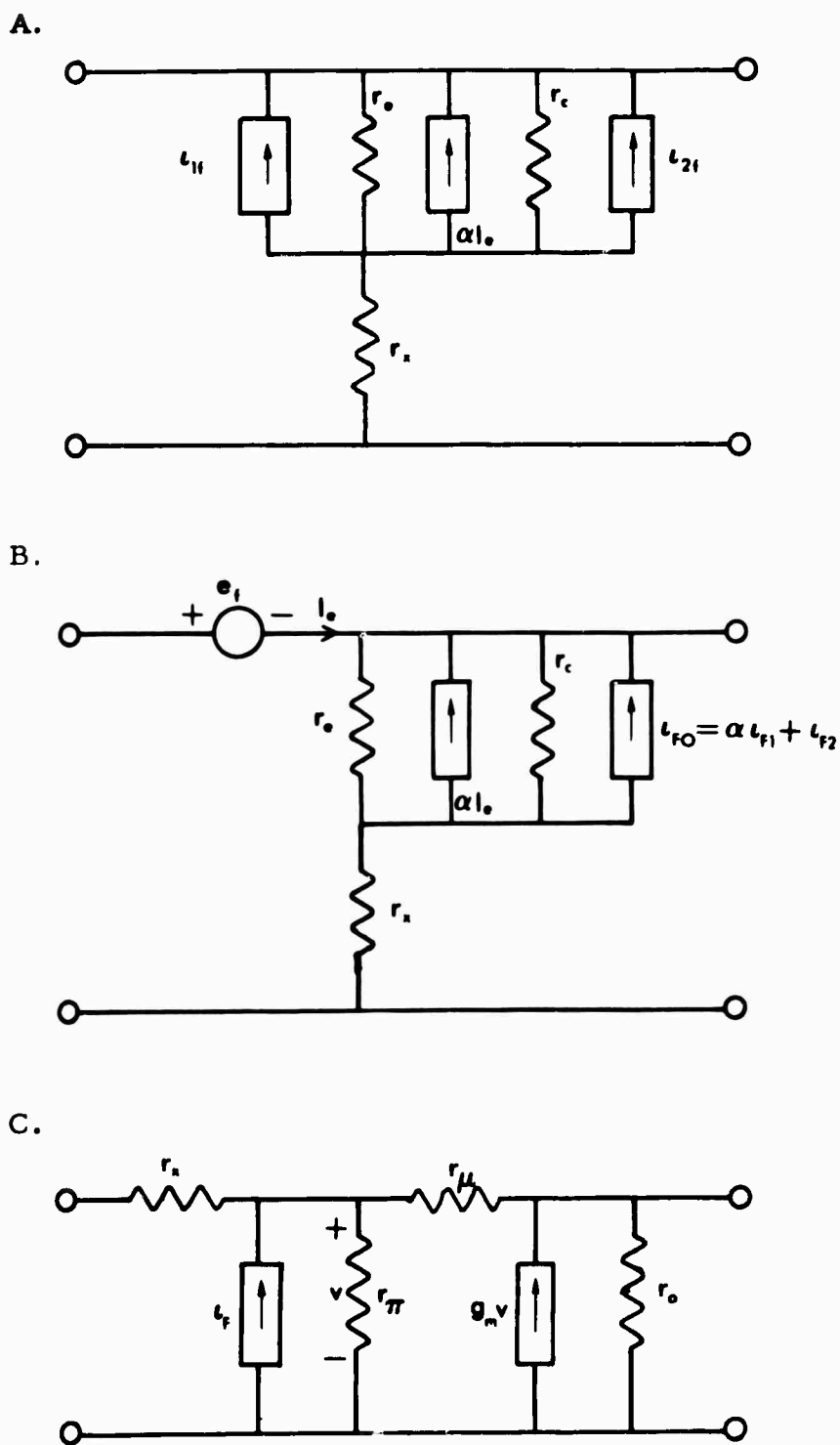FIGURE 2: Noise Resistance of Low Noise 2N930 Silicon Planar Transistors

Frequency, Hertz

FIGURE 3   Equivalent Circuit for Flicker Noise
in Bipolar Transistors

in parallel with r_e and i_{f2} in parallel with r_c and αI_e. 3B shows a flicker

noise emf, e_f series with r_e and a current generator i_{fo} in parallel with r_c.

These two circuits are identical if:

$$i_{fo} = i_{f2} + \alpha i_{f1}$$

and

$$e_f = i_{f1} \cdot r_e$$

Work by Chenette and Plumb[4,6] has shown that, for a large class of bi-

polar transistors -- with negligible flicker noise generated by collector

leakage current -- the flicker generators of Figure 3A or 3B are almost com-

pletely correlated. Since this is the case the simplified representation of

Figure 3C is often adequate. Here a single flicker noise generator is placed

in parallel with the emitter-base resistance in a hybrid-pi equivalent circuit.

This circuit can be used to predict an equivalent noise resistance or an ex-

pression for noise figure. The results are:

$$R_n = R_s + g_f (R_s + r_x)^2$$

or

$$F = 1 + \frac{g_f}{R_s} (R_s + r_x)^2$$

Here g_f is the equivalent noise conductance of i_f, i.e.

$$i_f^2 = 4\ kT g_f\ df$$

Empirically we know that $$g_f = \frac{K I_B r}{f^\alpha}$$

where the exponents α and r are often near unity -- yielding the common 1/f

dependence and a direct dependence on I_B. The results of the preliminary

measurements shown on Figure 1 and 2 are in essential agreement with this model. Some evidence of an anomaly at high resistances has been observed but more careful investigation is required.

Work now in progress includes a more detailed study of the effect of source resistance and an investigation of the possible effect of thermal environment on the 1/f noise source as well as the study of the matched pairs with field plates described earlier. The results of that work will be presented in a later report.

REFERENCES

1. E. R. Chenette, "Noise in Semiconductor Devices," _Advances in Electronics_, Vol. 23, L. Martin, Ed., Academic Press, 1967.

2. C. T. Sah, S. Y. Wu, and F. H. Hielscher, "The Effects of Fixed Bulk Charge on the Thermal Noise in Metal-Oxide-Semiconductor Transistors," _IEEE Trans. on Electron Devices_, ED-13, p. 410, April 1966.

3. W. H. Fonger, "A Determination of 1/f Noise Sources in Semiconductor Diodes and Triodes," in Transistors I(Princeton, N. J.: RCA Laboratories, 1965), p. 239.

4. E. R. Chenette, "Measurement of the Correlation Between Flicker Noise Sources in Transistors," _Proc. IRE_, 46, p. 1204, 1950.

5. J. F. Gibbons, "Low-Frequency Noise Figure and Its Application to the Measurement of Certain Transistor Parameters," _IEEE Trans. Electron Devices_, ED-9, p. 308, May, 1962.

6. J. L. Plumb and E. R. Chenette, "Flicker Noise in Transistors," _IEEE Trans. Electron Devices_, ED-10, p. 304, Sept. 1963.

7. V. G. K. Reddi, "Influence of Surface Conditions on Silicon Planar Transistor Current Gain," _Solid State Electronics_, 10, p. 305, April, 1967.

E. ADDITION TO LABORATORY FACILITIES: MEASUREMENT OF ELECTRONIC AND
   QUANTUM PARAMETERS (S. S. Li)

This section outlines the progress made toward the measurement of the

electronic and quantum parameters of materials.

The development and set-up of facilities for electrical and quantum parameters
study:

During this period, a system for measuring of Hall-effect, conductivity,

magneto-resistance, thermoelectric, thermomagnetic and PEM effect at tempera-

tures between 4.2°K and room temperature has been designed and built. The

basic equipment in this set-up consists of a 6" Varian electromagnet, Air

Products Helium Cryotip refrigeration system, high sensitivity nano-volt

potentiometer, sampling oscilloscope, nanosecond light source and chart re-

corder. This set-up has been successfully tested using gold diffused silicon

specimens. Several measurements on silicon specimens are being undertaken

using these facilities. A liquid nitrogen cryostat has also been built for

minority carrier lifetime experiments using the photoconductivity decay method.

Preparation of Samples:

Another important aspect of progress is the preparation of samples. A

diffusion furnace has been adapted for the diffusion of gold in a neutral or

reducing atmosphere; this equipment has been successfully tested by diffusing

gold at 1200°C into phosphorous-doped silicon. Personnel have been trained in

the preparation of the surfaces of the samples; this preparation includes

mechanical polishing, lapping and chemical etching of the specimens. Experi-

mentation has yielded a reliable technique for making ohmic contacts; the

technique makes use of electroless nickel plating and soldering.

All these preliminary tasks have been completed and samples are now

ready for measurements.

V. Discussion

The research of this second semi-annual period has enlarged our competence in solid-state materials and devices. It has yielded results of technical significance, and it has laid the foundations for future study and growth.

From the research concerning glasses has come a fundamental understanding of the role that structural disorder plays in determining electronic properties. This knowledge will undergird much of the research to come -- certainly in glasses, perhaps in more ordered materials as well.

From the research concerning measurement techniques has emerged capabilities that will prove invaluable in many of our envisaged materials studies. The x-ray research has yielded a method for determining particle size distributions; one future effort, for example, will be the adaptation of this method to semiconductors, enabling the measurement of impurity-atom clustering in degenerate silicon and germanium. Analysis concerning the electron microprobe has opened the way to the employment of this tool in determining the structure of thin films; this work has begun, utilizing samples of permalloy films made during this period in our magnetic-film laboratory. Finally, the analysis of thickness error in quantitative transmission microscopy has provided another technique for the examination of the structure of ceramics.

From the research concerning semiconductors and semiconductor devices has come progress collateral to that reported with respect to structural analysis. This period has seen the acquisition and installation of our facilities for Hall-effect, lifetime, and conductivity measurements at cryogenic and elevated temperatures. Samples have been prepared and the first measurements have been made. The data forthcoming from these facilities will be correlated

with that yielded from structural analysis and from measurements of noise spectra. Device-oriented research will continue, building upon the preliminary knowledge reported here dealing with noise performance and with the influence of degenerate concentrations of impurity atoms.

Radiation studies have continued and have yielded knowledge that will be described in the report for the next semi-annual period.

The plan of research will remain the same. In the materials research, correlation will be sought between electronic and structural parameters, which will be further correlated with radiation effects. The materials research will both suggest collateral device studies and will be guided by them.

The progress described in this report is in accord with this plan.

DOCUMENT CONTROL DATA - R&D

(Security classification of title, body of abstract and indexing annotation must be entered when the overall report is classified)

1. ORIGINATING ACTIVITY *(Corporate author)*	2a. REPORT SECURITY CLASSIFICATION
University of Florida Engineering and Industrial Experiment Station Gainesville, Florida 32601	Unclassified
	2b. GROUP

3. REPORT TITLE

A CENTER OF COMPETENCE IN SOLID STATE MATERIAL AND DEVICES

4. DESCRIPTIVE NOTES *(Type of report and inclusive dates)*

Scientific. Interim.

5. AUTHOR(S) *(First name, middle initial, last name)*

Fred A. Lindholm	Robert W. Gould	Sheng S. Li
Arthur J. Brodersen	Larry L. Hench	Jack Salz
Eugene R. Chenette	John J. Hren	James K. Watson

6. REPORT DATE	7a. TOTAL NO. OF PAGES	7b. NO. OF REFS
10 October 1968	223	118

8a. CONTRACT OR GRANT NO.	9a. ORIGINATOR'S REPORT NUMBER(S)
F 19628-68-C-0058-ARPA Order 1060	Scientific Report No. 2
b. PROJECT, TASK, WORK UNIT NOS. 8687 n/a n/a	
c. DOD ELEMENT 615450ID	9b. OTHER REPORT NO(S) *(Any other numbers that may be assigned this report)*
d. DOD SUBELEMENT n/a	AFCRL-68-0493

10. DISTRIBUTION STATEMENT

1 - Distribution of this document is unlimited. It may be released to the Clearinghouse, Department of Commerce, for sale to the general public.

11. SUPPLEMENTARY NOTES	12. SPONSORING MILITARY ACTIVITY
This research was supported by the Advanced Research Projects Agency.	Air Force Cambridge Research Laboratories (CRW) L. G. Hanscom Field Bedford, Massachusetts 01730

13. ABSTRACT The content of this report, for the second semi-annual period of contract support, comprises three main topics. The first treats of the relationships borne in glasses between microstructure and electrical properties. One study examines a theoretical model that relates the aperiodicity in glass lattices to electron transport. Another explores the structural mechanisms involved in the nucleation of crystal phases in glasses.

The second main topic deals with the measurement of parameters of material structure, demonstrating the measurement techniques by applying them to various materials: glass ceramics, nickel alloys, magnetic films, and degenerate semiconductors. Discussion centers on analysis by small-angle x-ray scattering, by electron microprobe, and by transmission electron microscopy. The errors inherent in the measurements and the theoretical basis for the analysis of data receive special attention.

The third main topic concerns semiconductors and semiconductor devices. One study reports, for degenerate n-type germanium and silicon, the theoretical variation of the density of quantum states as a function of impurity concentration. In another, the conventional theory of pn junctions is extended by removing the assumption of non-degeneracy. Finally, for both devices and bulk material, the sources of noise are subjected to theoretical and experimental study.

DD FORM 1473
1 NOV 65

14. KEY WORDS	LINK A		LINK B		LINK C	
	ROLE	WT	ROLE	WT	ROLE	WT
Transition Metal Glasses						
Electron Transport in Glasses						
Crystallization of Glass						
Particle-Size Distribution						
Small Angle X-ray Scattering						
Optical Diffraction Modeling						
Degenerate Semiconductors						
Nickel Alloys						
Electron Microprobe						
Permalloy Films						
Transmission Microscopy						
Density of States in Semiconductors						
PN Junctions						
Generation and Recombination Noise						
Low Frequency Noise in Transistors						
Integrated Circuits						